AD-A195 633 DEVELOPMENT AND EVALUATION OF CHEMICAL DIAGNOSTIC METHODS(U) GEO-CENTERS INC NEWTON CENTRE MA L ISSACSON MAY 88 GC-TR-88-1429 N00014-84-C-2011 1/2

UNCLASSIFIED F/G 7/2 NL

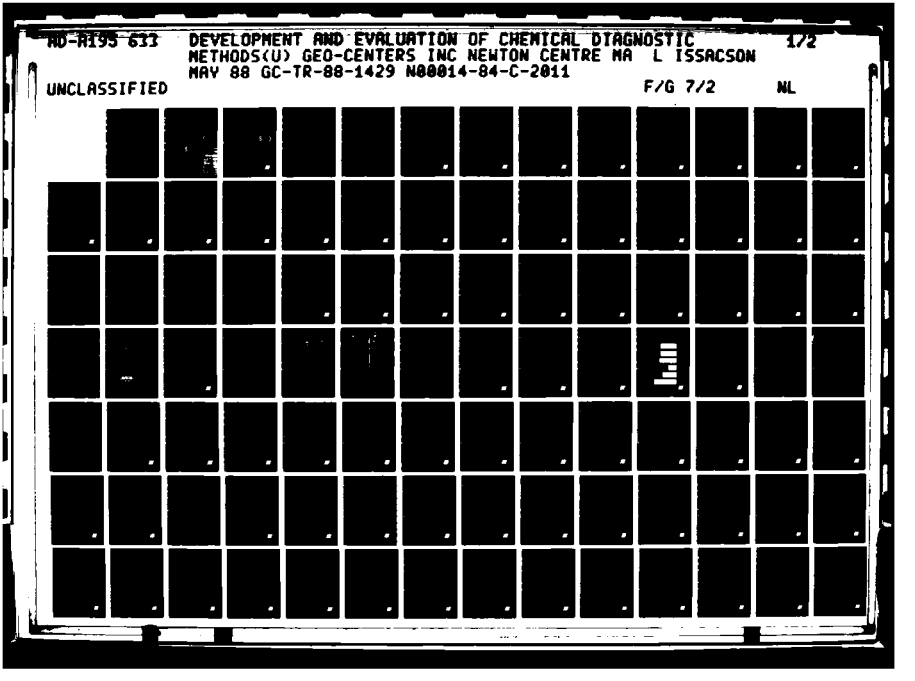

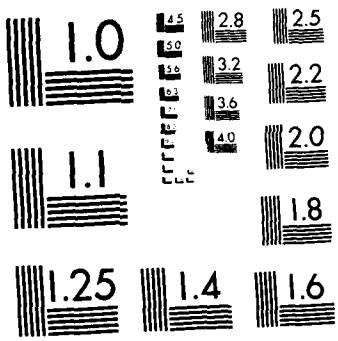
1.0
1.1
1.25
1.4
1.6
1.8
2.0
2.2
2.5
2.8
3.2
3.6
4.0
4.5
5.0
5.6
6.3

(4)

GC-TR-88-1429

DEVELOPMENT AND EVALUATION OF CHEMICAL DIAGNOSTIC METHODS

GEO-CENTERS, INC.

(4)

GC-TR-88-1429

DEVELOPMENT AND EVALUATION

OF

CHEMICAL DIAGNOSTIC METHODS

FINAL REPORT

PREPARED FOR
NAVAL RESEARCH LABORATORY
4555 OVERLOOK DRIVE, S.W.
WASHINGTON, D.C. 20375-5000
UNDER CONTRACT NUMBER N00014-84-C-2011

PREPARED BY
GEO-CENTERS, INC.
7 WELLS AVENUE
NEWTON CENTRE, MA 02159

MAY 1988

GEO-CENTERS, INC.

UN
SECURITY CLASSIFICATION OF THIS PAGE

REPORT DOCUMENTATION PAGE

ADA195633

1a. REPORT SECURITY CLASSIFICATION UNCLASSIFIED	1b. RESTRICTIVE MARKINGS
2a. SECURITY CLASSIFICATION AUTHORITY	3. DISTRIBUTION/AVAILABILITY OF REPORT Approved for public release; distribution unlimited.
2b. DECLASSIFICATION/DOWNGRADING SCHEDULE	
4. PERFORMING ORGANIZATION REPORT NUMBER(S) GC-TR-88-1429	5. MONITORING ORGANIZATION REPORT NUMBER(S)
6a. NAME OF PERFORMING ORGANIZATION GEO-CENTERS, INC. 6b. OFFICE SYMBOL (If applicable)	7a. NAME OF MONITORING ORGANIZATION
6c. ADDRESS (City, State, and ZIP Code) 7 Wells Avenue Newton Centre, MA 02159	7b. ADDRESS (City, State, and ZIP Code)
8a. NAME OF FUNDING/SPONSORING ORGANIZATION Naval Research Laboratory 8b. OFFICE SYMBOL (If applicable)	9. PROCUREMENT INSTRUMENT IDENTIFICATION NUMBER Contract Number N00014-84-C-2011
8c. ADDRESS (City, State, and ZIP Code) 4555 Overlook Avenue, S.W. Washington, DC 20375-5000	10. SOURCE OF FUNDING NUMBERS PROGRAM ELEMENT NO. / PROJECT NO. / TASK NO. / WORK UNIT ACCESSION NO.

11. TITLE (Include Security Classification)
DEVELOPMENT AND EVALUATION OF CHEMICAL DIAGNOSTIC METHODS (U)

12. PERSONAL AUTHOR(S)
Isaacson, L.

13a. TYPE OF REPORT	13b. TIME COVERED	14. DATE OF REPORT (Year, Month, Day)	15. PAGE COUNT
Final	FROM 10/83 TO 3/88	May 1988	160

16. SUPPLEMENTARY NOTATION

17. COSATI CODES		
FIELD	GROUP	SUB-GROUP

18. SUBJECT TERMS (Continue on reverse if necessary and identify by block number)
Hydrazine dosimetry, passive detection, electrochemical detection, optoacoustic sensors, surface acoustic wave sensors, deuterated lubricants,

19. ABSTRACT (Continue on reverse if necessary and identify by block number)
A variety of novel chemical diagnostics methods have been investigated and applied to practical problems of interest to the DOD. Novel sensing methods and devices have been utilized in the investigation of hydrazine vapors with both passive and active sensing devices; optoacoustic detection schemes for explosive vapors; the detection of water vapor using surface acoustic wave (SAW) sensors, and the determination of the oxidative stability of novel deuterated lubricants by detection of evolved gaseous by-products.

20. DISTRIBUTION/AVAILABILITY OF ABSTRACT ☒ UNCLASSIFIED/UNLIMITED ☐ SAME AS RPT. ☐ DTIC USERS	21. ABSTRACT SECURITY CLASSIFICATION UNCLASSIFIED
22a. NAME OF RESPONSIBLE INDIVIDUAL J.R. McDonald	22b. TELEPHONE (Include Area Code) (202) 767-3340 22c. OFFICE SYMBOL Code 6110

DD FORM 1473, 84 MAR 83 APR edition may be used until exhausted. All other editions are obsolete.

SECURITY CLASSIFICATION OF THIS PAGE
UNCLASSIFIED

18. oxidative stability.

TABLE OF CONTENTS

TABLE OF CONTENTS (Cont'd.)

TABLE OF CONTENTS (Cont'd.)

TABLE OF CONTENTS (Cont'd.)

LIST OF FIGURES

LIST OF FIGURES, CONT'D.

LIST OF FIGURES, CONT'D.

LIST OF FIGURES, CONT'D.

LIST OF FIGURES, CONT'D.

LIST OF TABLES

LIST OF TABLES, CONT'D.

1.0 INTRODUCTION

The Chemical Diagnostics Branch (Code 6110) of the U.S. Naval Research Laboratory requires technical assistance in its mission to develop materials and systems for fleet applications and to devise diagnostic methods appropriate for their test and evaluation. Of particular interest is the continuation of on-going research into the development of advanced fuels and lubricants (e.g., deuterated lubricants) and the design and testing of novel diagnostic methods for characterizing and monitoring their performance.

To assist Code 6110 in accomplishing its goal, GEO-CENTERS initiated a multi-disciplinary research effort to develop and demonstrate novel diagnostic methods employing optical, optoacoustic, surface acoustic wave (SAW) and electrochemical schemes for application to energetic materials such as explosives and rocket propellants. Related research efforts examined the emission properties of pyrotechnic decoy materials and the monitoring of lubricant performance with emphasis on deuterated lubricants.

This final report describes results obtained by GEO-CENTERS in support of tasks in:

(1) The detection of hydrazine vapor in air using passive dosimetry;

(2) The detection of hydrazine vapor in air using electrochemical methods;

(3) The detection of explosives; vapors using optoacoustic methods;

(4) The detection of water vapor in air using a surface acoustic wave sensor;

(5) The emission characteristics of infrared decoy materials;

(6) The monitoring of deuterated lubricant performance.

The sections entitled, "The Detection of Hydrazine Vapor in Air Using Electrochemical Methods" and the "The Detection of Water Vapor in Air Using a Surface Acoustic Wave Sensor" represent work performed by Transducers Research Inc., Naperville, Illinois, and Microsensors, Inc., Fairfax, Virginia, under sub-contract to GEO-CENTERS, INC.

2.0 DETECTION OF HYDRAZINE VAPOR IN AIR USING PASSIVE DOSIMETRY

2.1 Introduction

The use of hydrazine (Hz) and monomethylhydrazine (MMH) as high energy propellants has increased dramatically in recent years. The Space Shuttle program consumes large quantities of hydrazines and substantial quantities are used in satellites, Titan missiles, and aircraft auxiliary power units. With this increased usage has come an increased concern over the toxicological properties of hydrazines.

Exposure to hydrazines is known to cause a broad spectrum of maladies, among them kidney, liver and lung damage, blood abnormalities, mutagenicity, teratogenicity, and marked emotional and behavioral changes. At low exposure levels, the hydrazines are highly suspected carcinogens. Therefore, the maximum tolerated toxic level has been set at five parts-per-million (ppm), and to safeguard against overexposure, the American Conference of Government Industrial Hygienists (ACGIH) has recommended the threshold limit values (TLV's) of Hz and MMH to be 100 and 200 parts-per-billion (ppb) respectively (2.1). A recent study suggests that exposure may be more harmful than previously believed, and recommends not only that TLV's be lowered, but also that maximum lifetime dose levels be established (2.2).

To protect NASA and Department of Defense personnel, the air is routinely monitored in areas where hydrazines are stored and/or handled to ensure that exposure does not exceed recommended TLV levels. In order to supplement the present

monitoring program, there is need for an inexpensive, lightweight, personal dosimeter that could be distributed to a large number of personnel, work for at least a week, and be easily analyzed.

The development of a dosimeter badge is complicated by the reactivity of the hydrazines. Hydrazines have a strong tendency to adsorb and decompose on surfaces, particularly metals, making them difficult to sample and measure. No commercial dosimeters or laboratory techniques are available. A passive electrochemical monitor was tested and found to be unreliable (2.3). Liquid sorbent badges were investigated, but lacked the precision necessary. Strong acids on solid supports have been used for field sampling of hydrazine, but MMH is not stable in the medium. Because antioxidants have improved the stability of MMH solutions, we decided to investigate a solid support coated with an organic acid having antioxidant properties, citric acid.

2.2 Experimental

The passive dosimeter developed for this work is shown in Fig. 2.1. A plastic sample holder, 1/2" deep and 1 3/4" in diameter, supports the collector which is a disc of polyester matted drafting film dipped in a 20%-30% citric acid in methanol solution and allowed to dry. A 1/16" spacer provides an air gap between the substrate and the top of the badge. Passive diffusion is controlled by a one inch diameter pattern of 140 1mm holes in the top (diffuser). The dosimeters are tested by exposing them in a test chamber through which flows air containing a known level of the contaminant hydrazine. MMH or hydrazine in air mixtures are made up using a test system

previously described (2.3). The test chamber shown in Fig. 2.2 is constructed of glass with a removable end and contains a pair of Teflon baffles to promote laminar flow. Three such chambers of different diameters allow changing face velocity without changing gas stream conditions. At least two hours are allowed for equilibration in the test chamber between changes in experimental conditions. The concentration is verified by collecting impinger samples from the test chamber.

The badges are disassembled and analyzed to determine the amount of the contaminant hydrazine collected. The badges and impinger samples are analyzed for MMH using two accepted wet chemical methods: (a) A NIOSH approved method (#S149) using phosphomolybdic acid, and (b) a coulometric titration with bromide and amperometric endpoint detection. The coulometric method is a NRL/White Sands modification of reference 2.4, in which we miniaturized the system to improve sensitivity.

2.3 Results

2.3.1 Monomethyl Hydrazine Testing

Initial testing was done using MMH and dosimeters machined from solid Teflon. MMH was chosen as it is less stable than hydrazine and was expected to be more difficult to maintain in a collection medium. Dosimeters machined from Teflon were tested by exposing four badges to a dry gas stream contaminated with 242 ppb MMH and measuring the amount of MMH detected versus the exposure time. Exposure times between 3 and 65 hours were examined over several weeks; the results are shown in Fig. 2.3. A correlation coefficient of 0.996 was obtained for 107 data points. The badge sample rate as calculated from this data was 31 ml/min.

The stability was verified in two tests. In each test, four badges were exposed to MMH, two of the badge substrates were analyzed immediately and the other two substrates were stored in the dark at room temperature in a sealed container. No degradation was observed for any of the storage periods (3-7 days) as shown in Table 2.1. Badge D_1 always reads higher than average while D_4 is lower than the average.

The linearity was investigated by exposing the badges to MMH between 70 and 240 ppb in dry air for 16 hours, see Fig. 2.4. Deviation from ideal performance was observed below 100 ppb. This deviation became considerably more pronounced with the addition of humidity, although at higher relative humidities performance was about the same as when sampling dry air. The poorest performance was observed at about 25% relative humidity. This phenomenon was strongly suspected to be due to surface adsorption. This was demonstrated by "preconditioning" several badges in a humid MMH contaminated gas stream, quickly substituting fresh citric acid discs for the exposed discs, then exposing these "preconditioned" badges along with several unconditioned badges for a short time. The "preconditioned" badges approached ideal behavior, while the unconditioned badges exhibited the same deviations from the ideal which we had been experiencing in other low dose tests. It seemed evident that this was a materials problem and not the fault of the citric acid film. Later testing with "nude" citric acid films further substantiated this belief. Microscopic examination of the badge material revealed that they had been machined from Teflon stock formed of compressed particles. This "sintered" Teflon stock is full of microscopic cavities and pores which, with the addition of tool marks left by machining, create an enormous surface area.

A second set of badges was machined from polypropylene. Even through polypropylene does not have the same porous character of the compressed Teflon badge, the results were not substantially improved. We began to consider that the tool marks left by machining might be a more important factor than previously believed. Commercially available molded fluoroware sample cassettes were obtained and converted into badges by drilling hole patterns in the faces and adding polyethylene spacers. These badges performed better at low concentrations and/or low exposure times than the previous badges, and were used exclusively for all subsequent testing. The data comparing the machined Teflon, machined polypropylene, and molded fluoroware badges, is presented in Fig. 2.5.

The relative humidity effects were tested using MMH at the TLV, and relative humidities between 10-75% RH. The molded badges were exposed to the gas stream from 15 minutes to 16 hours at a face velocity of 5 ft/min. At sampling times less than one hour the apparent sampling rate has significant dependence upon relative humidity: the worst case is at 25% RH, see Fig. 2.6. The reason for this peculiar effect is unknown.

The face velocity effects on the sample rate were also tested for 2, 5 and 20 ft/min. Two tests were used to compare the face velocities and the results are shown in Table 2.2. One was conducted for high exposure time and low humidity while the other test was conducted for short exposure and high humidity. The sample rates were within 10% of each other.

Interferences by isopropyl alcohol, ammonia, NO_2, and freons were examined by mixing approximate TLV levels with the

TLV level of MMH. These results are in Table 2.3. The amount of MMH collected by the badges was compared to samples collected with impingers. Little variation was observed in the MMH concentration in the badge compared to analyzed impinger samples from the same gas stream. Ammonia caused a reduction in MMH collected of about 13%. Recent tests indicate that the reduction caused by ammonia may be as great as 25%. More study is needed in this area.

2.3.2 Hydrazine Testing

Preliminary hydrazine testing consisted of a comparison of the molded fluoroware badge, machined Teflon badge, and several other similar badges with nonporous plastic diffusers. Badges were exposed to hydrazine (61-95 ppb) in dry air for periods of 2-16 hours, and a face velocity of 2.5 ft/min. The molded Fluoroware dosimeters exhibited the highest apparent flow rate at all exposures and displayed the least scatter. Therefore, the molded fluoroware badge was the best candidate for testing with hydrazine.

The precision data in Table 2.4 was collected in dry air with 70 ppb Hz and 2.5 ft/min face velocity. The apparent sampling rate remains essentially constant between 2 and 6 hours with little scatter in data points.

The addition of humidity to the Hz contaminated gas stream caused the citric acid film to crystallize producing a depression of the apparent sample rate and increased scatter. The crystallization only occurred when high relative humidities were present. Crystallization stopped by (a) increasing the citric acid/methanol concentration from 20% to 30%, (b) drying or

curing the films at room temperature rather than elevated temperatures, and (c) reducing the handling of the polyester film or citric acid coated discs. Since implementation of these measures, no crystallization problems have occurred despite efforts to promote crystallization by running tests at high relative humidities. Further investigations are underway to understand the cause of the crystallization.

The linearity data in Fig. 2.7 was obtained in 128 ppb Hz and 55-60% relative humidity at a face velocity of 5 ft/min. Exposure times were 15 minutes to 90 hours. Deviation from ideal performance at low concentration/low exposure time is similar to that observed when sampling humidified MMH gas streams. At 15 minutes exposure time, the apparent sample rate is about 75% of the calculated mean sample rate.

2.3.3 "Nude" Disc Testing

The citric acid substrate was used without the diffusion barrier to investigate the collection characteristics at different face velocities using 100 ppb hydrazine in air. We observed an increase of hydrazine collected with increasing face velocities as shown in Fig. 2.8 for both dry and 60% RH. The effect of RH on collection of hydrazine was minimal as shown in Fig. 2.9. All the samples were within 10% of the dry measurement except one point collected at 40% RH. We also investigated the citric acid substrate at 20 ppb, but too much scatter was observed to use the data. The two major sources of error are: the hydrazine concentration in the chamber is probably perturbed when we put the badges in the chamber, and the analysis methods are at their limit of accuracy.

2.3.4 Theoretical Model

A theoretical model to characterize the passive collection of hydrazines by the dosimeter has been developed. The model permits optimization of the badge design, such as the number and size of the holes, prior to badge construction. Parameters such as diffusion coefficients and viscosities were obtained or computed from standard references when available (2.6, 2.7, 2.8). The actual computations describing the badge were modeled after those used in reference 2.5 with a modification to account for the passage of air through the diffusion barrier and the air gap between the diffuser and substrate.

The theoretical model predicted a sampling rate for MMH 40% greater than actual. The diameter of the diffuser holes was taken to be the diameter of the drill size (1 mm) used to make the holes in the diffuser. After inspecting the diffuser holes, the diameter was reduced 20% to 0.8 mm for the computation. This is reasonable considering imperfections in the holes. The corrected model predicted within 18% the actual quantity of MMH collected for three different face velocities. Figure 2.10 shows the two theoretical curves and actual data. The model predicts less than a 5% change in the collection rate for face velocities between 17-100 ft/min. and a decrease of 25% at 2 ft/min. which correlates with experimental results. Because typical workplace face velocities are between 50-75 ft/min (2.5), the badge should exhibit little or no velocity effects.

2.4 Conclusions

Citric acid/methanol applied to polyester film makes an excellent substrate for sampling both monomethylhydrazine and

hydrazine. The exposed substrate is easily analyzed by accepted methods. There are virtually no humidity effects associated with the citric acid film itself, and humidity effects associated with the citric acid substrate in conjunction with the current badge design remain within 25%. Badges have been exposed for periods of time up to 91 hours. Results have been highly repeatable and have remained linear over this range of exposure times, except as concentrations/exposure times approach zero. Badges have been stored for up to 8 days after exposure with no loss of collected hydrazines. Ammonia, freons, and isopropyl alcohol interfere minimally with sampling, but more study is needed in this area. The current badge design has little face velocity effects between 2 and 20 ft/min.

Badge material is a continuing concern for sampling at levels less than 100 ppb. It appears that the surface condition of the badge is at least as important as material selection. It is doubtful that optimum surface conditions can be achieved through machining processes. It is conceivable, however, that using a molded badge with molded holes in the diffuser, optimized with respect to hole diameter and pattern, badge size, and internal dead volume, the limit of reliable detection could be lowered from the present 15 minutes at TLV for Hz and MMH to the goal of 5 minutes at TLV.

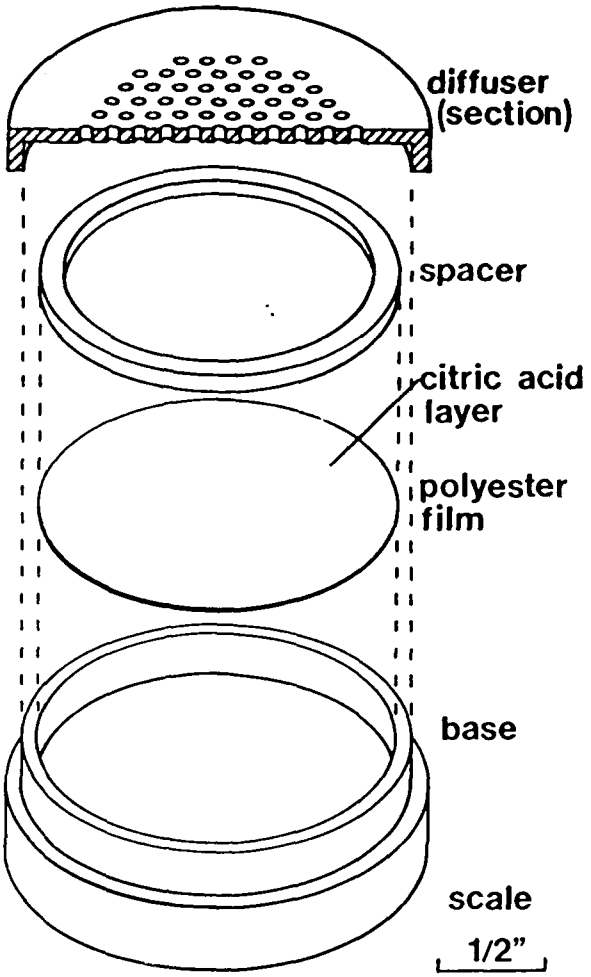

Figure 2.1 Dosimeter

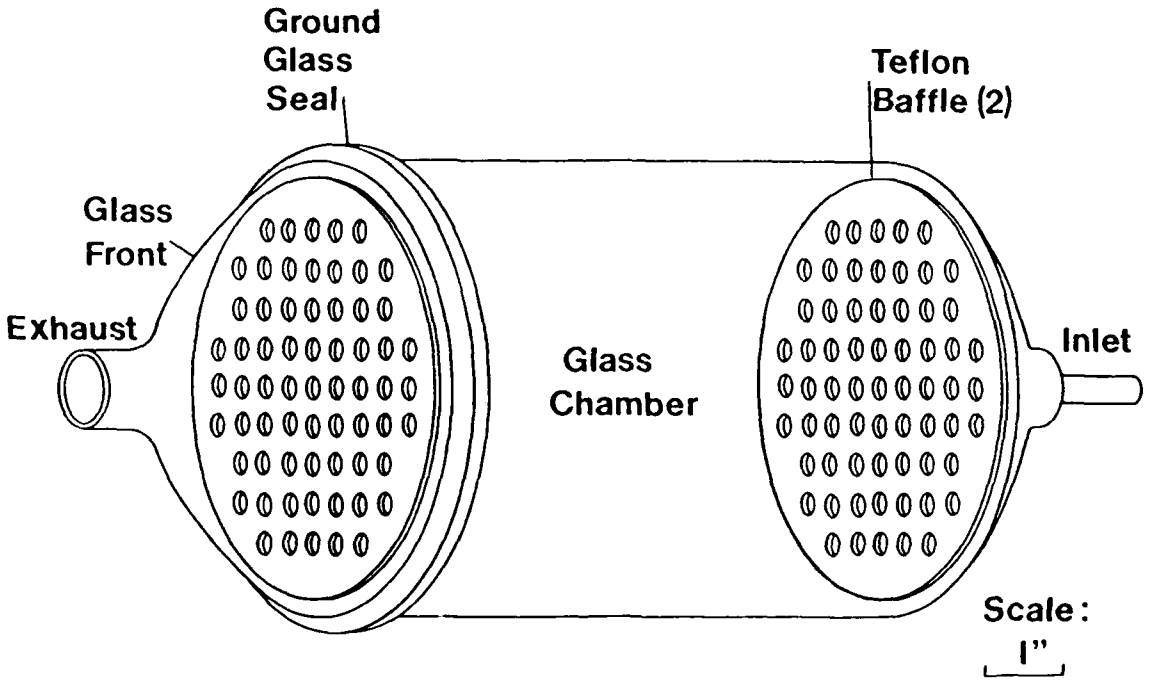

Figure 2.2 Dosimeter Test Chamber

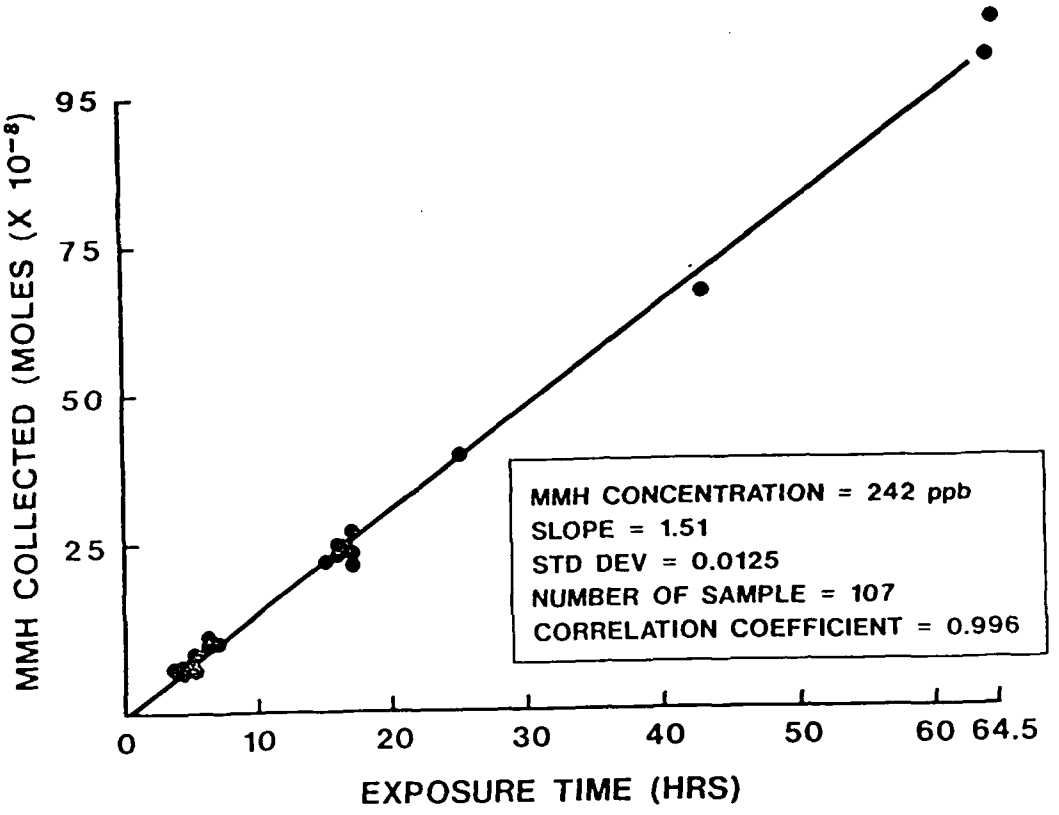

Figure 2.3 Precision test using machined Teflon badges.

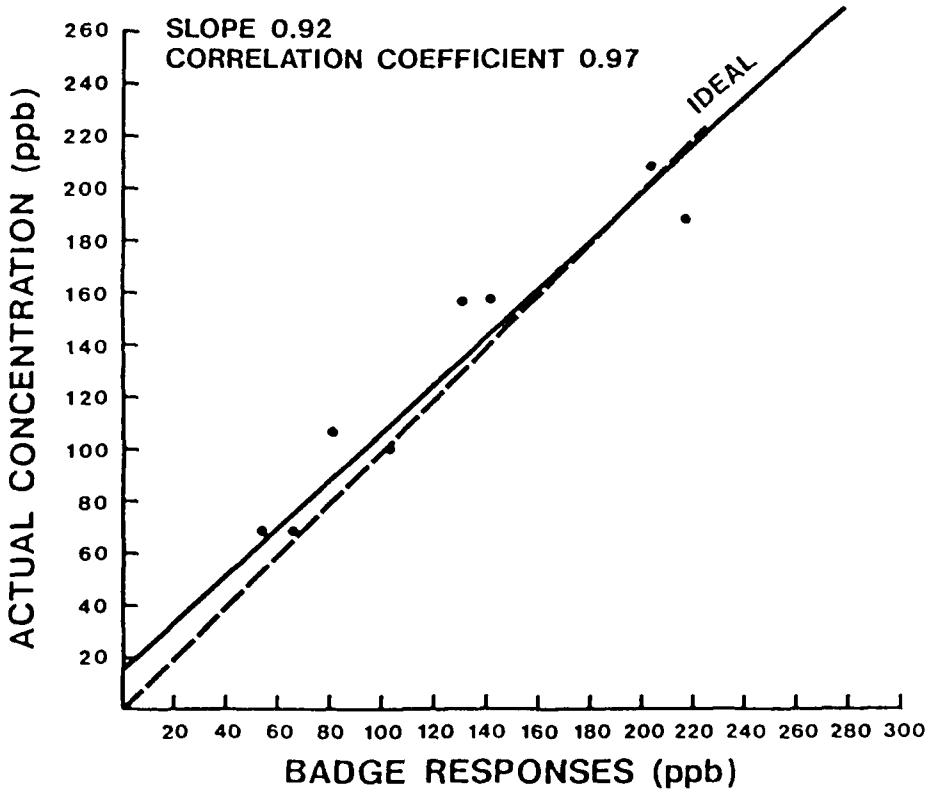

Figure 2.4 Linearity test using machined Teflon badges.

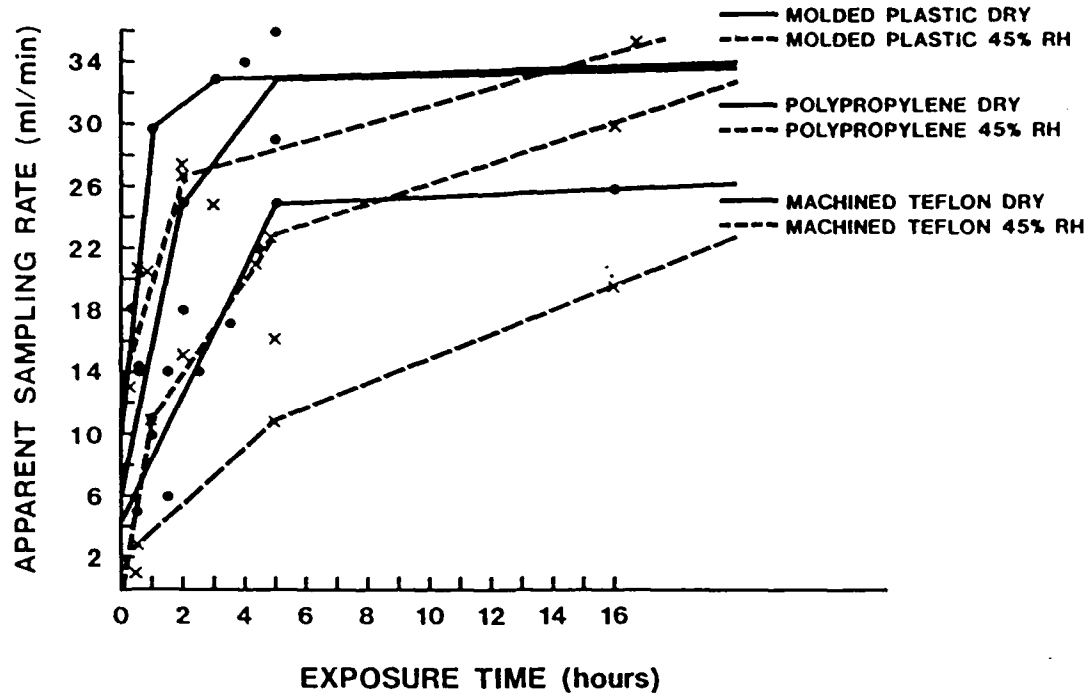

Figure 2.5 Adsorption test on three different badge materials.

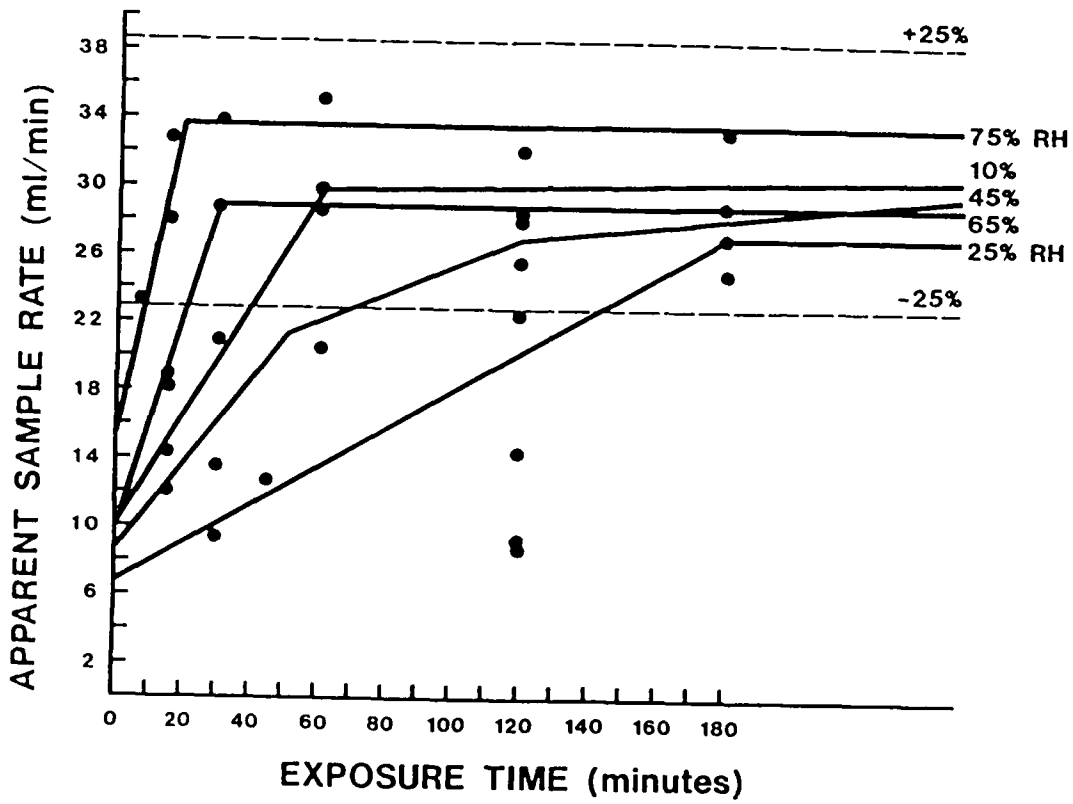

Figure 2.6 Relative humidity test using molded Fluoroware badges.

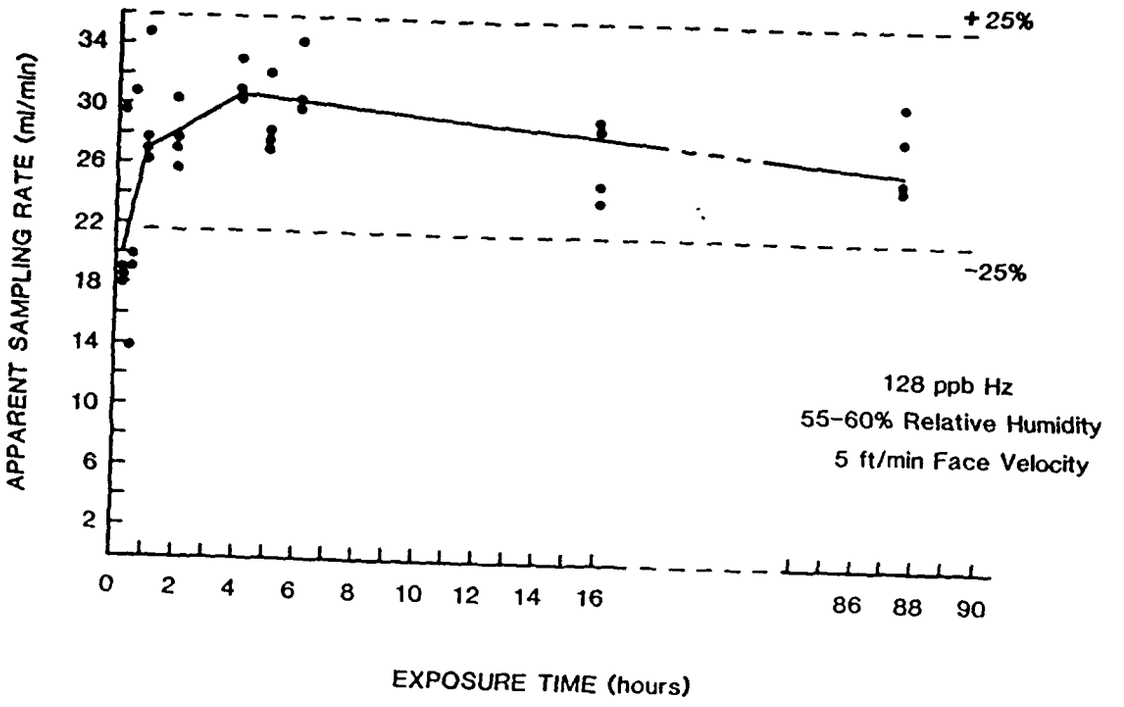

Figure 2.7 Linearity test of hydrazine on molded Fluoroware badges.

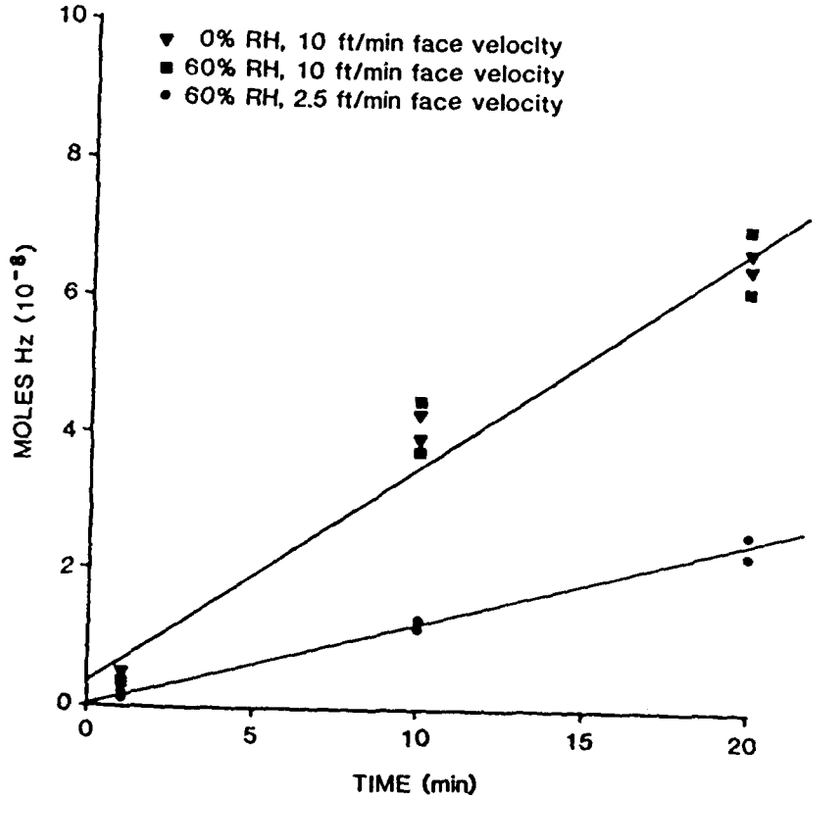

Figure 2.8 Face velocity effects on "nude" citric acid films.

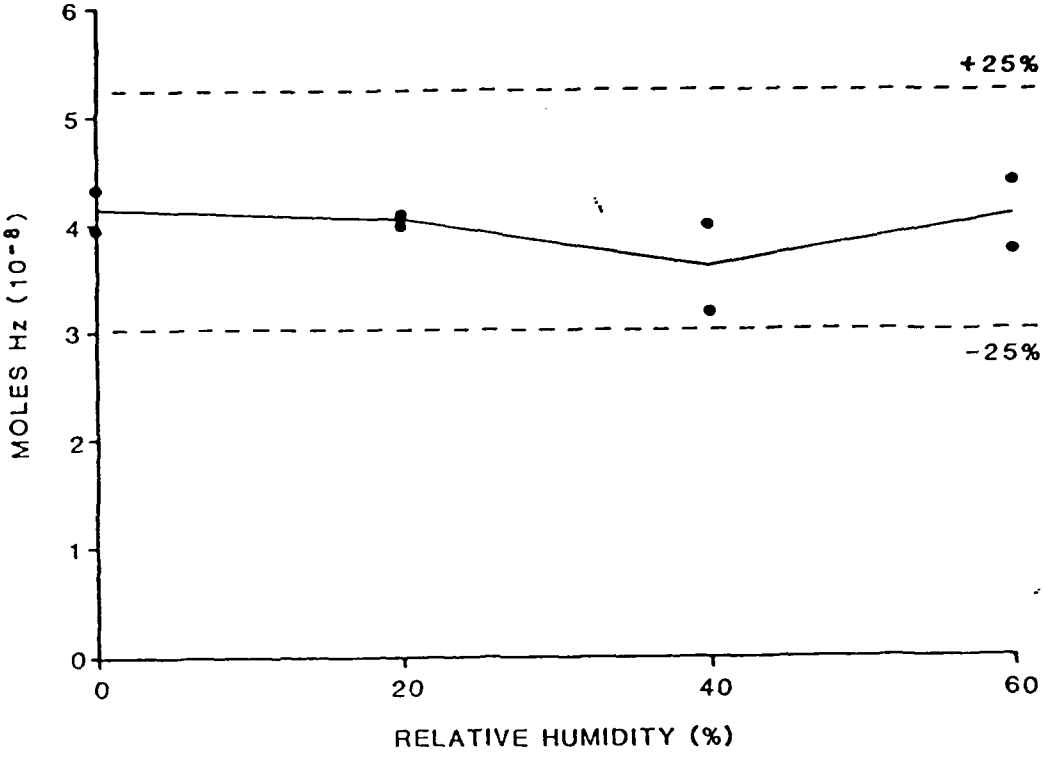

Figure 2.9 Relative humidity effects on "nude" citric acid films.

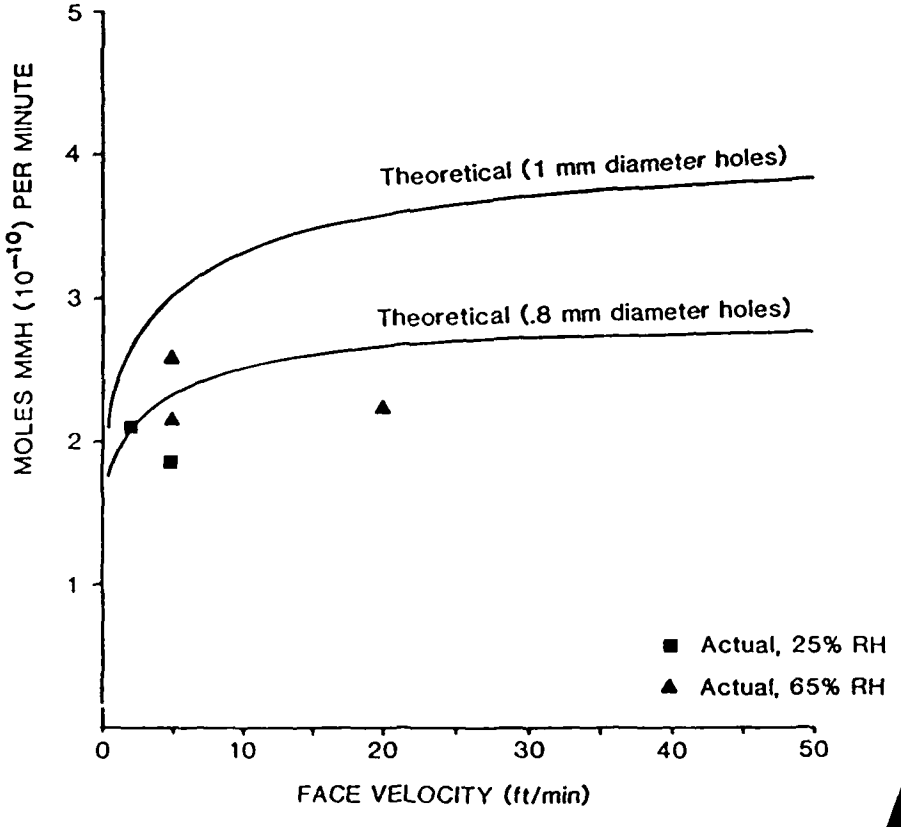

Figure 2.10 Plot of theoretical sampling rate.

GEO-CENTERS, INC.

Table 2.1 Stability Test Results

Test 1
Exposure time = 18 hours
MMH Concentration = 242 ppb

Badge	Number of Days Stored	Concentration (moles)
D_1	0	28.3×10^{-8}
D_2	0	26.0×10^{-8}
D_3	3	27.9×10^{-8}
D_4	3	25.5×10^{-8}

Test 2
Exposure time = 5 hours
MMH Concentration = 268 ppb

Badge	Number of Days Stored	Concentration (moles)
D_2	0	7.75×10^{-8}
D_4	0	7.25×10^{-8}
D_1	5	9.38×10^{-8} (25%)
D_3	7	8.0×10^{-8} (7%)

Table 2.2 Face Velocity Tests

Exposure Time (Hrs)	Relative Humidity (%)	Face Velocity (ft/min)	MMH (ppb) concentration	Sample Rate (ml/min)
3	65	5	190	29.1
3	65	20	179	30.4
64	25	2	199	27.4
64	25	5	173	26.1

Table 2.3 Interference Tests

2 hour exposure time, 65% relative humidity, 5 ft/min face velocity

MMH CONCENTRATION (ppb)	INTERFERENCE COMPOUND	INTERFERENCE CONCENTRATION (ppm)	SAMPLE RATE (ml/min)
174	isopropyl alcohol	500	30.1(9%)
188	ammonia	50	24.9(13%)
176	freons	15	28.7(0%)
**	nitrogen dioxide	1	**

() percent change caused by interference compound
** MMH and nitrogen dioxide are highly reactive and our tests indicate that they do not coexist at significant concentrations.

Table 2.4 Precision Tests

Face Velocity = 2.5 ft/min
Hydrazine Conc. = 70 ppb

Sample time (hrs)	Apparent Sampling Rate (ml/min)
6	30
3	34
2	35
6	33
6	31
2	30
Average	32.2 ± 2.1

GEO-CENTERS, INC.

2.5 References

2.1 J.A.E. Hannum, Recent Developments in the Toxicology of Propellant Hydrazines, Chemical Propulsion Information Agency, CPIR 82-15, June 1982.

2.2 Committee on Toxicology, "Emergency and Continuous Exposure Guidance Levels for Selected Airborne Contaminants", Vol. 5, Board on Toxicology and Environmental Health Hazards, Commission on Life Sciences, National Research Council, National Academy Press, Washington, D.C. 1985.

2.3 S.L. Rose and J.R. Holtzclaw, A Critical Comparison of Commercially Available Hydrazine Detectors, Naval Research Laboratory, Washington, D.C., NRL Report 8848, March 19, 1985.

2.4 Edward C. Olson, The Coulometric Determination of Hydrazine and Substituted Hydrazines, Analytical Chemistry, Vol. 32, No. 12, November 1960, pgs. 1545-1547.

2.5 Rosemary Ellersick, Research on Personal Dosimeters to Measure Hydrazine fuels in Air, Walden Division of Abcor, Inc., Report SAM-IR-79-22, Wilmington, Mass., Oct. 1979.

2.6 W.J. Lyman, W.F. Reehl, and D.H. Rasenblatt, "Handbook of Chemical Properties Estimation Method," (McGraw Hill: New York, 1982).

2.7 R.H. Perry, "Chemical Engineers Handbook," 5th Edition. (McGraw Hill: 1973).

2.8 F.C. Tompkins and R.L. Goldsmith, A New Personal Dosimeter for the Monitoring of Industrial Pollutants. Walden Division of Abcor, Inc., Wilmington, Mass., 1976.

3.0 DETECTION OF HYDRAZINE VAPOR IN AIR USING ELECTROCHEMICAL METHODS

3.1 Introduction

The major objectives of this task are the design, assembly and production of a reliable sensor that can function as a replacement part for the 7000 series hydrazine sensor presently in use at the Kennedy Space Center (KSC). It is desired that the replacement sensor be compatible with currently used instrumentation. To accomplish these objectives, the following program elements were defined:

(1) Examine and evaluate the present cell in detail;

(2) Design and engineer a sensor that retrofits into the basic, presently employed detection unit; and

(3) Assemble and evaluate the new sensor designs and deliver prototypes.

3.2 Current Sensor Examination and Evaluation

The current sensors exhibit the following specific problems:

(1) Long stabilization times

(2) Weepage or leakage

(3) Rapid loss in sensitivity in continuous use (two months to failure)

(4) Potential negative backgrounds

An examination of several cells produced the following results:

(1) A new cell (ESI 1058) was filled with electrolyte (23% KOH) and challenged with 49 ppm NO_2. The cell stabilized overnight and gave 300-380 mv signals on the instrument's low range (x1).

(2) An old ESI cell was examined and found to be leaking. The cell was cleaned and refilled with fresh KOH. No signal was observed. The counter/reference endplate was found to be corroded and was replaced. The cell was cleaned with dilute acid, allowed to stand overnight in distilled water and refilled with distilled water. The sensor never gave a signal when challenged with NO_2.

(3) A second old ESI cell (ESI 0746) was found to be weeping, and gave no signal when challenged with NO_2 vapor. The cell was cleaned and dried for 24 hours and refilled with fresh KOH. The sensor gave a 90 mv signal when challenged with 49 ppm NO_2. The cell was disassembled, cleaned with dilute acid, rinsed and refilled with KOH. The signal level increased to 290 mv when challenged with 49 ppm NO_2.

Physical inspection of the cells indicates that weeping/leaking of the electrolyte (KOH) through the pores and lack of seal integrity probably constitute the major source for cell failure.

Table 3.1 and Figure 3.1 indicate how three current ESI sensors respond to a 49 ppm NO_2 challenge as a function of time (i.e., between 11/21/86 and 12/7/87). Note that the current output from the cell initially changes when new potentiostats are installed, but appear to return near former levels with time.

3.3 Retrofit Sensor Design and Evaluation

The emphasis on retrofit sensor design initially focused on developing more rugged cells designed to minimize and/or stop the leakage of the electrolyte. This was approached in two ways; namely, (1) the development of different electrolyte systems and (2) the identification and use of different membrane/seal materials and their fit with cell components. Figure 3.2 is a sketch of two cells designed to overcome identified problems.

Table 3.2 and Figure 3.3 compare test results, as a function of bias voltage, for ESI cells and variously constructed TRI hydrazine cells to a 115 ppm monomethyl hydrazine (MMH) challenge. Table 3.2 also contains data on the concentration of NO_2 needed to produce a 1 ppm MMH signal level as a function of bias voltage on the cell.

Figures 3.4 to 3.7 illustrate the response of various TRI cells to 100-115 ppm MMH challenges. Figure 3.4 shows how Nafion cells respond to 100 ppm MMH as the bias voltage changes. Figures 3.5 and 3.6 compare the response changes of an ESI cell, KOH filled TRI cell and a non-aqueous filled TRI cell at bias voltages between -100 and +300 mv. Figure 3.7 shows the behavior of several TRI cells and an ESI cell as a function of air flow rate (i.e., 100-1000 ml/min) through the chamber. The air flow rate appears to induce more change in the output signal from the ESI cell.

A test was developed to determine the weeping pressure of the membranes and the electrolytes used in the sensors. For this

test, the membrance is placed in a housing with the electrolyte on one side and a vacuum pump on the other. The vacuum is gradually increased at a rate of 2 cm Hg/10 sec and the point at which visible electrolyte weeping occurs is recorded. Figure 3.8 compares the weeping pressures determined for a variety of electrolytes on G110 (Zitex) membranes proposed for use in the retrofit system. Some data on 662-123, the membrane used in the ESI cell, is also given. Figure 3.9 compares the weeping pressure measured for propylene carbonate, a non-aqueous electrolyte, through a series of different membranes. All of the membranes tested appear better than the Zitex membrane. Figure 3.10 compares the signals measured for a 0.7 microamp/ppm MMH sensor containing a second backing membrane defined in the figure. Note that the teflon membrane does not pass the signal while CG-4 and the Gortex membranes appear better than the Zitex G110 membrane.

Table 3.3 compares the response time measured for a series of propylene carbonate electrolyte filled sensors. Except for PC-002, all sensors tested had 90% rise or decay times less than 15 seconds.

A series of sensors were assembled and tested for ruggedness by shipping them in two states of assembly/readiness. Six cells were shipped in the following manner:

(1) Three cells were to be filled with KOH, one was filled and the other two were shipped dry,

(2) Three cells were to be filled with 2M $LiClO_4$, one was filled and the other two were shipped dry.

Both sensors shipped filled were received with the electrolyte either spilled or leaked from the reservoir. The source/cause for this leakage was not apparent.

A series of life tests were initiated on KOH and $LiClO_4$/propylene carbonate electrolyte based cells with Zitex membranes. Figure 3.11 compares response data to 100 ppm MMH from the two cells. The KOH based cell worked erratically, and began losing sensitivity approximately 12 days after start-up. At 18 days after start-up, the reservoir was examined and found to be practically empty. It has not been determined whether membrane weeping or an actual tear, leak or bad seal was responsible for electrolyte loss. This observed behavior in signal loss is typical for KOH type sensors. The $LiClO_4$/propylene carbonate cell performed well, exhibiting a stable signal output and small drift in background and response time.

Based on the weeping pressure results given in Figures 3.9 and 3.10, the 1.0 micron Gortex and Celgard 4510 (CG-4) were selected as alternative membrane materials to be tested. The Celgard proved difficult to heat seal to the cell body. Celgard materials with different backings should be explored for easier construction and assembly. The Gortex membrane modified cells yield responses to 8 and 100 ppm MMH challenges that are similar to the Zitex based cells. There is no evidence of electrolyte weeping, even at 500 mm Hg, for the cells with Gortex membranes. The preliminary waveform response and reproducibility for a Gortex membrane based sensor to 100 ppm MMH is given in Figure 3.12. The linearity of the sensor's response to MMH was tested

using sensors with propylene carbonate and membranes of Zitex or Gortex (Figure 3.13). The Zitex based cells appear to exhibit extreme non-linear responses to MMH while the Gortex cell appears to be much less non-linear. The change in linearity appears to occur for MMH concentrations above 20 ppm. This observed behavior needs to be validated.

It is evident that drastic redesign and reconfiguration of the electrochemical based hydrazine detector is needed. Membrane materials fabricated from Gortex appear to be superior to the present materials used and the teflon based Zitex membranes initially considered for retrofit. Additionally, the problems associated with cell seal materials need to be addressed. The design of the cell, as well as the type of material, needs to be integrated as a package to minimize this source of leakage.

RESPONSE TO 50 ppm NO2

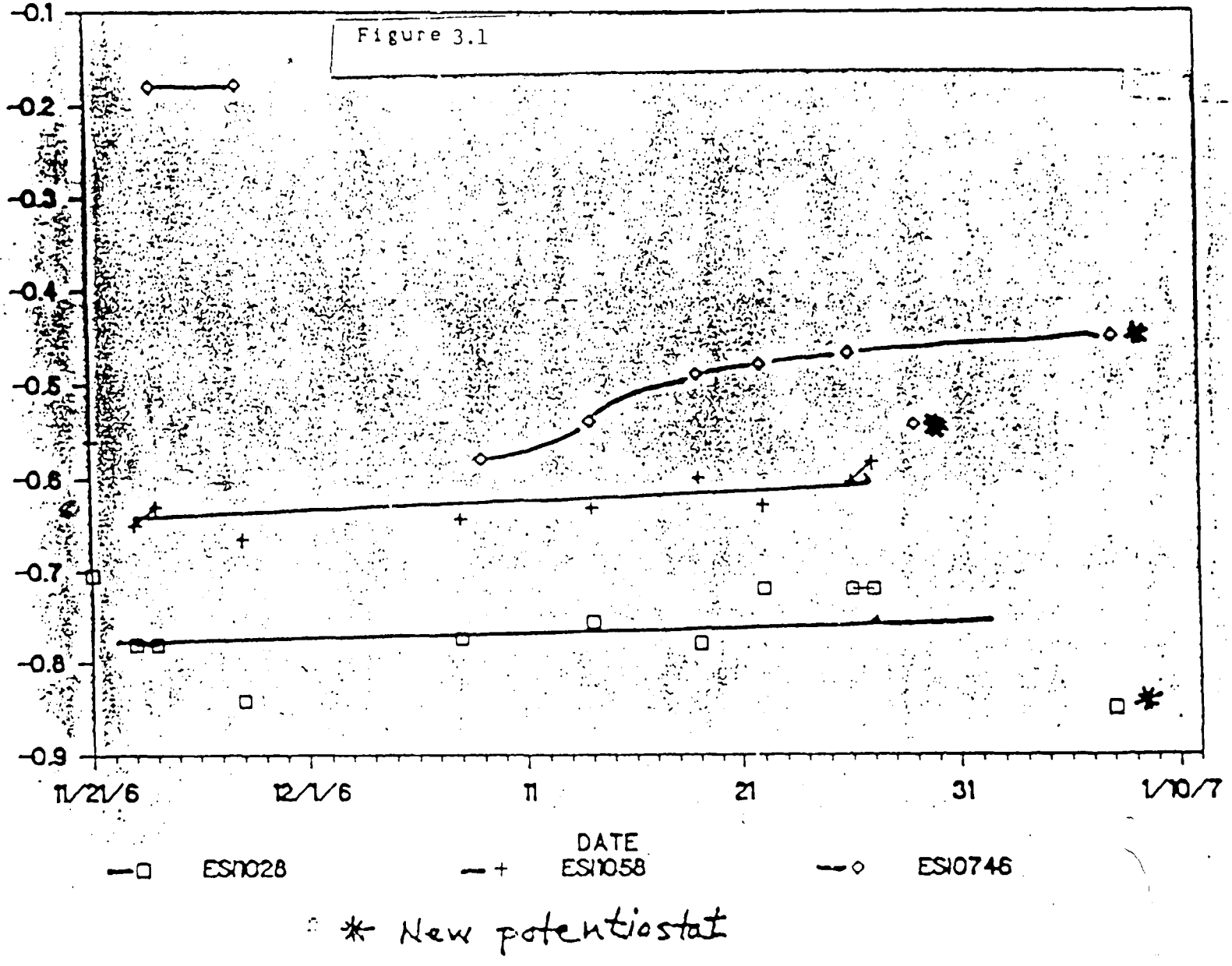

GEO-CENTERS, INC.

Table 3.1 Performance test results (signals) for ESI sensors. The sensors were on bias continuously but with periodic air flow through the sensors. Sensor ESI0746 was reconditioned by soaking in dilute acid and drying 12/1/1986.

TRI NASA-MMH PROJECT: ESI SENSOR TESTS

RESPONSE TO 50 ppm NO_2

DATE	ESI 1028 mV	ESI 1028 uA	ESI1058 mV	ESI1058 uA	ESI0746 mV	ESI0746 uA
11/21/6	-352	-0.704	-280	-0.56		
22						
23	-390	-0.78	-325	-0.65		
24	-390	-0.78	-315	-0.63	-90	-0.18
25						
26						
27						
28	-421	-0.842	-333	-0.666	-89	-0.178
29						
30						
12/1/6						
2						
3						
4						
5						
6						
7						
8	-387	-0.774	-322	-0.644		
9					-290	-0.58
10						
11						
12						
13						
14	-378	-0.756	-316	-0.632	-270	-0.54
15						
16						
17						
18						
19	-390	-0.78	-300	-0.6	-245	-0.49
20						
21						
22	-360	-0.72	-315	-0.63	-240	-0.48
23						
24						
25						
26	-360	-0.72	-302	-0.604	-234	-0.468
27	-360	-0.72	-292	-0.584		
28						
29					-272	-0.544*
30						
31						
JAN 1 '87						
2						
3						
4						
5						
6						
7		-0.85*				-0.45*

*New potentiostats

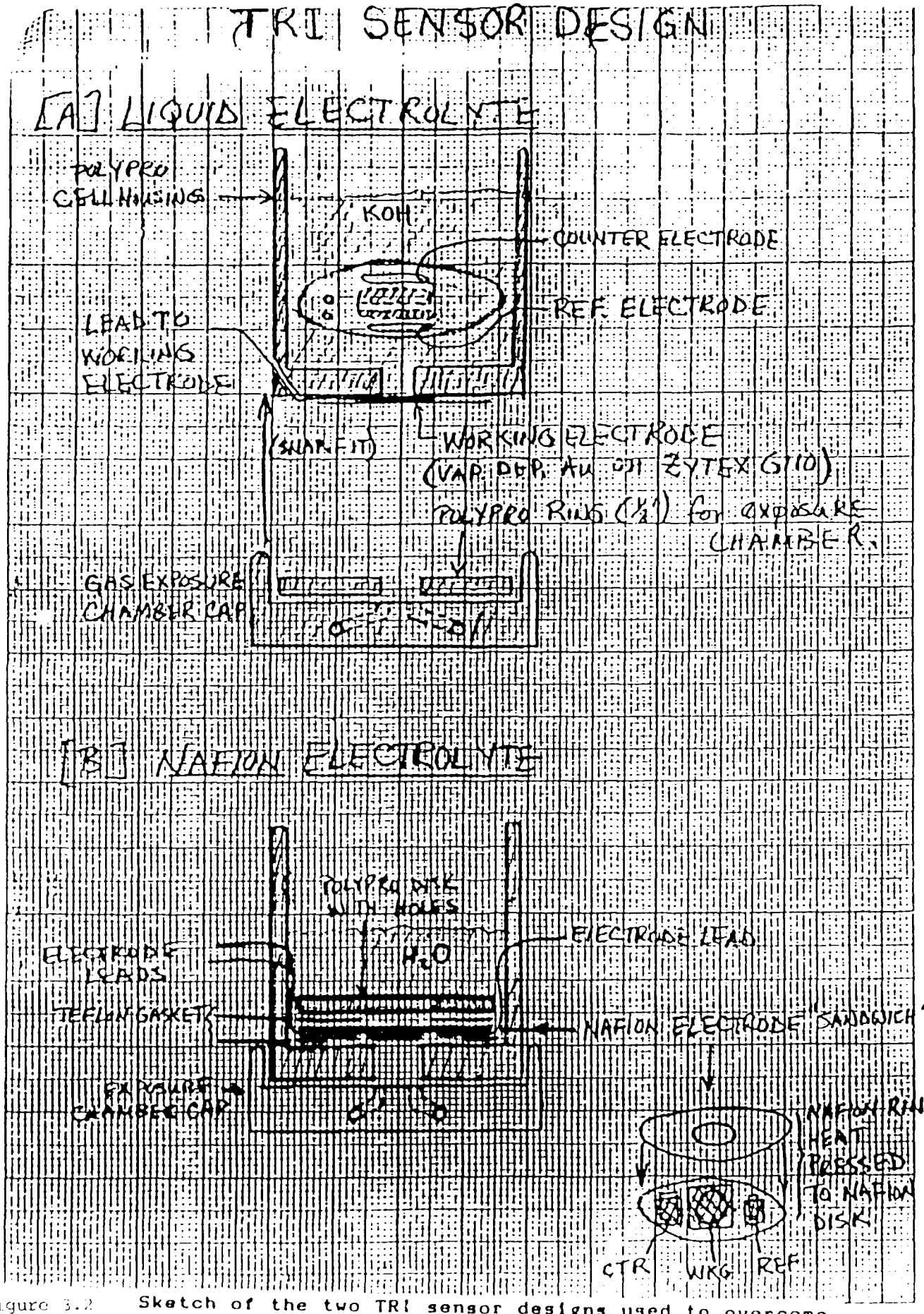

Figure 3.2 Sketch of the two TRI sensor designs used to overcome the identified chemical/mechanical problems.

Table 3.2 Test results for an ESI cell, two liquid electroclyte TRI cells, and three SPE TRI cells at four different potentials (data for interference to NO_2 shown).

SIGNAL VS. WE BIAS : 115 PPM MMH

CELL --->> BIAS (mV)	ESI1028 uA	LEAU001 uA	LEAU002 uA	NAFAU002 uA	NAFAU003 uA	NAFIR003 uA
300	42	555	107	22	2.7	175
200	40	500	91	18	4.4	135
100	42	415	93	17	0.4	89
-100	50	230	95	16	1	62

** LEAU001 - VAPOR DEP. AU WORKING;KOH ELECTROLYTE
** LEAU002 - VAPOR DEP. AU WORKING; PROPCO3 ELECTROLYTE

INTERFERENCE TESTING OF MMH SENSORS

CONCENTRATION OF INTERFERENT TO PRODUCE 1 PPM MMH SIGNAL

SENSOR	NO2 +200 mV	NO2 +100 mV	NO2 -100 mV
ESI1028	(-)30 ppm		
ES10746		(-)55	
LEAU001	(-)175	>(-)200	
LEAU002	>(-)1000		
NAFAU002	10		
NAFAU005	15		
NAFIR001	~1		

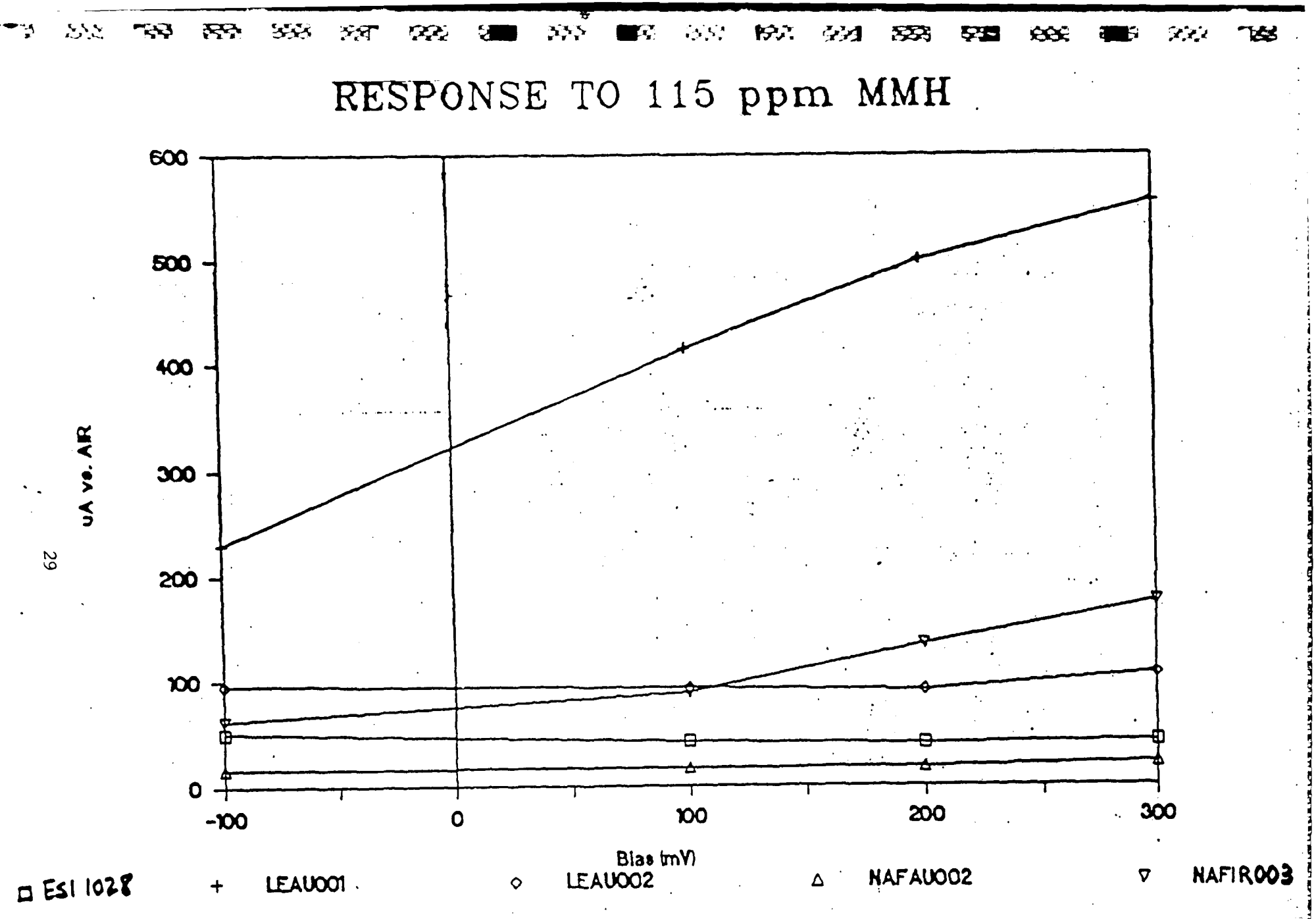
RESPONSE TO 115 ppm MMH
600
500
400
300
200
100
0
uA vs. AIR
-100
0
100
200
300
Bias (mV)
ESI 1028
LEAU001
LEAU002
NAFAU002
NAFIR003

Figure 3.3

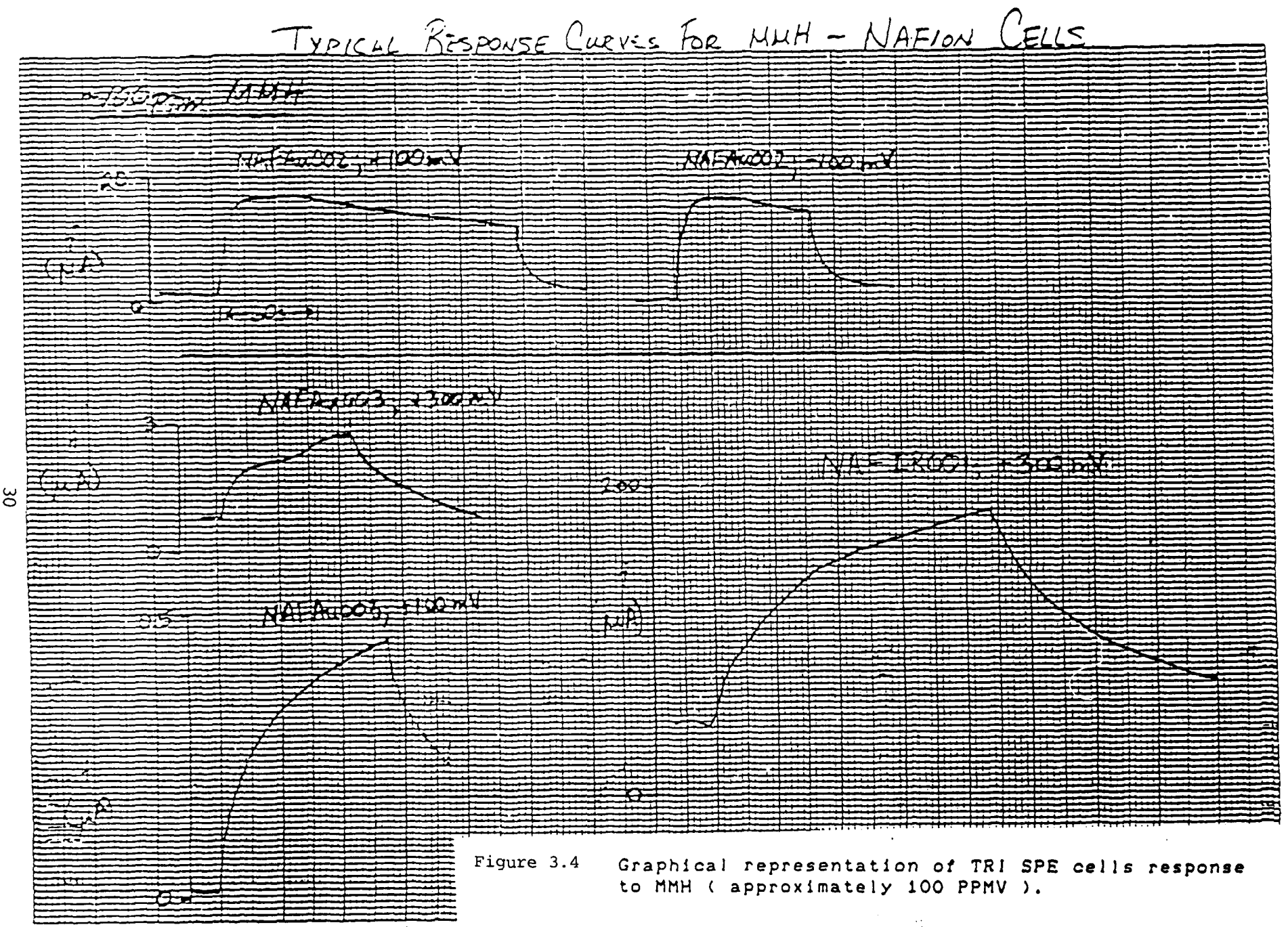

Figure 3.4 Graphical representation of TRI SPE cells response to MMH (approximately 100 PPMV).

Response Curves For 115ppm MMH

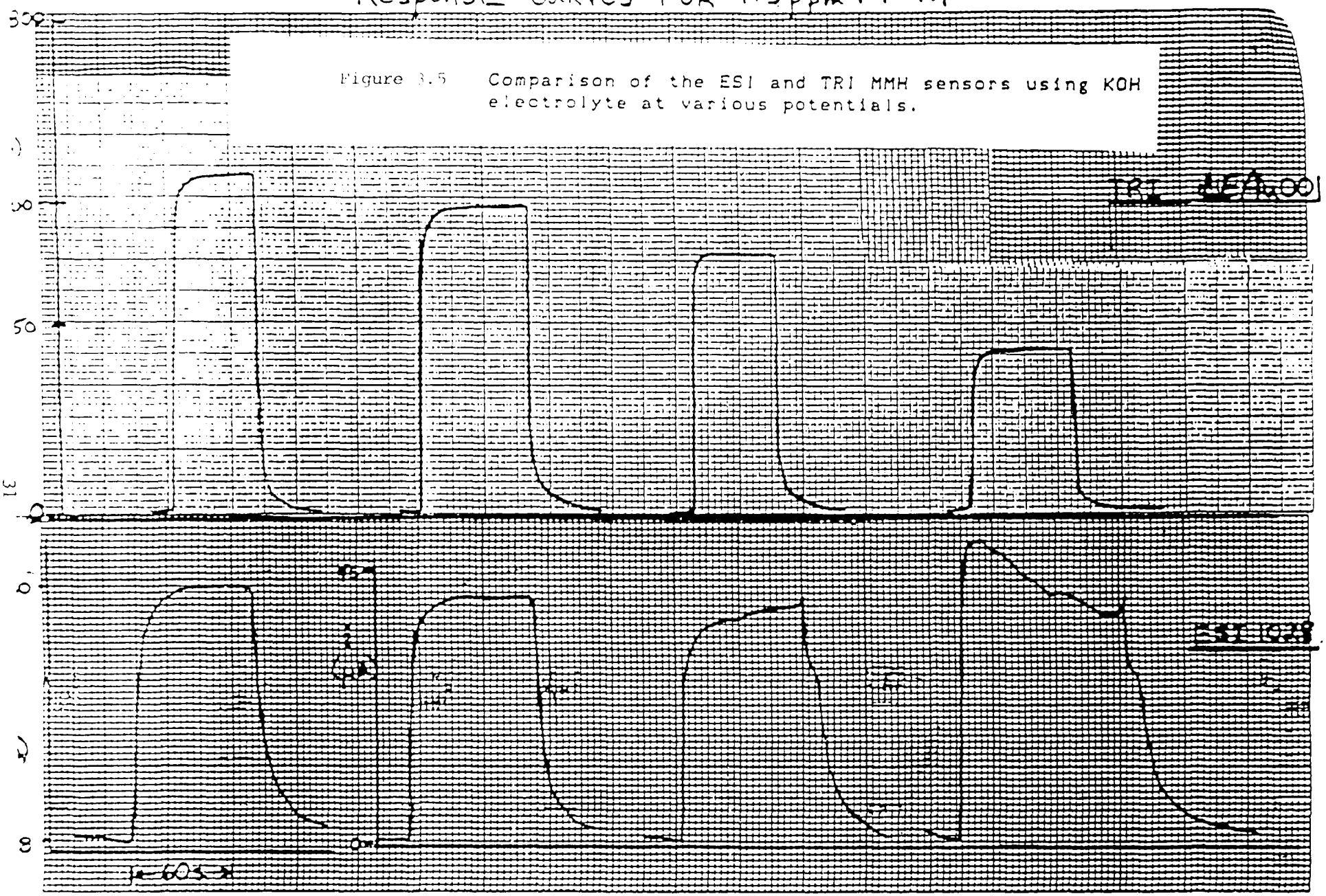

Figure 3.5 Comparison of the ESI and TRI MMH sensors using KOH electrolyte at various potentials.

RESPONSE CURVES FOR 115 ppm MMH

Response of the TRL platinum sensor to MMH.

TRL LEAK 002

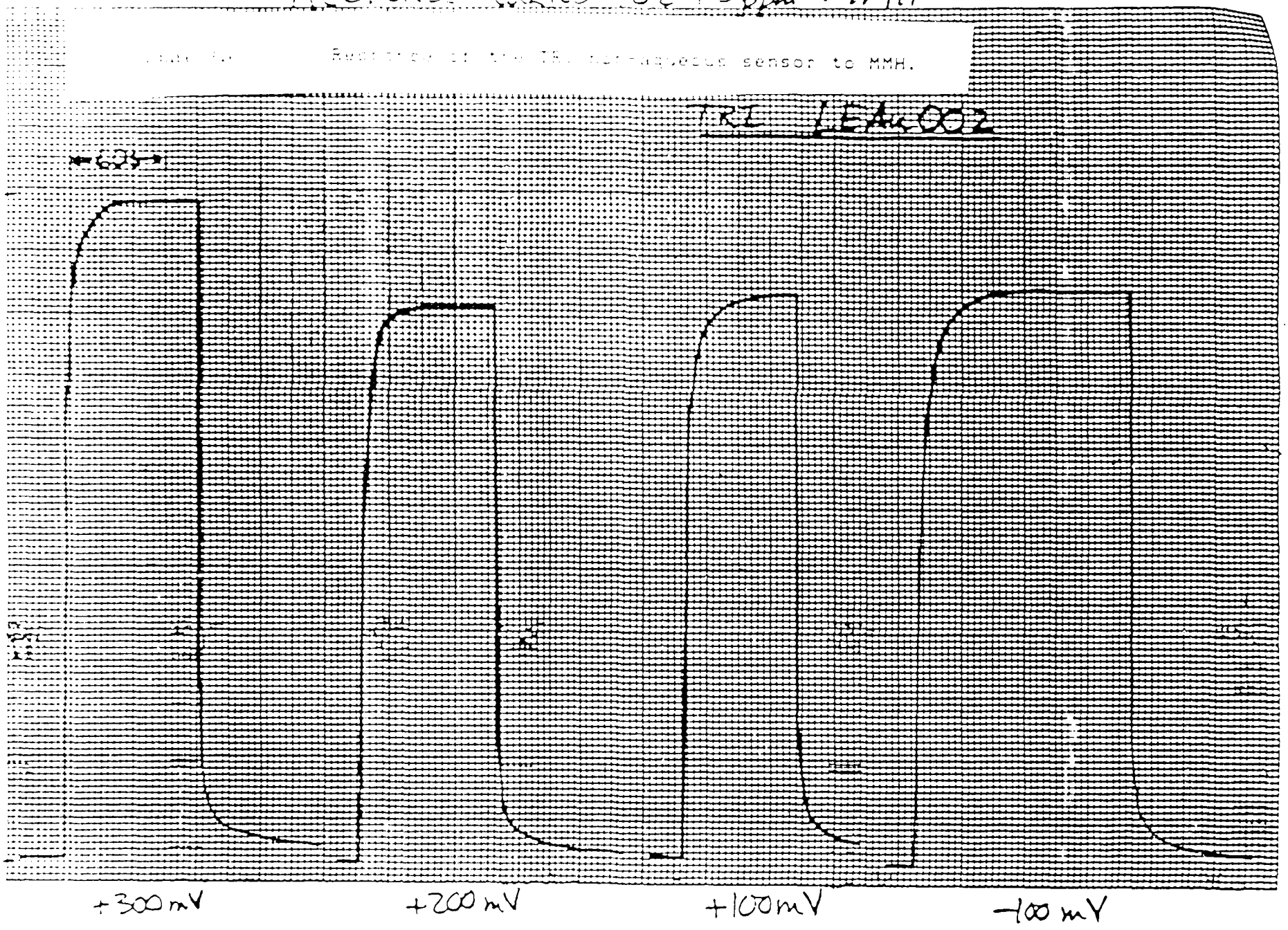

Figure 3.7

CELL RESPONSE VS. FLOW RATE

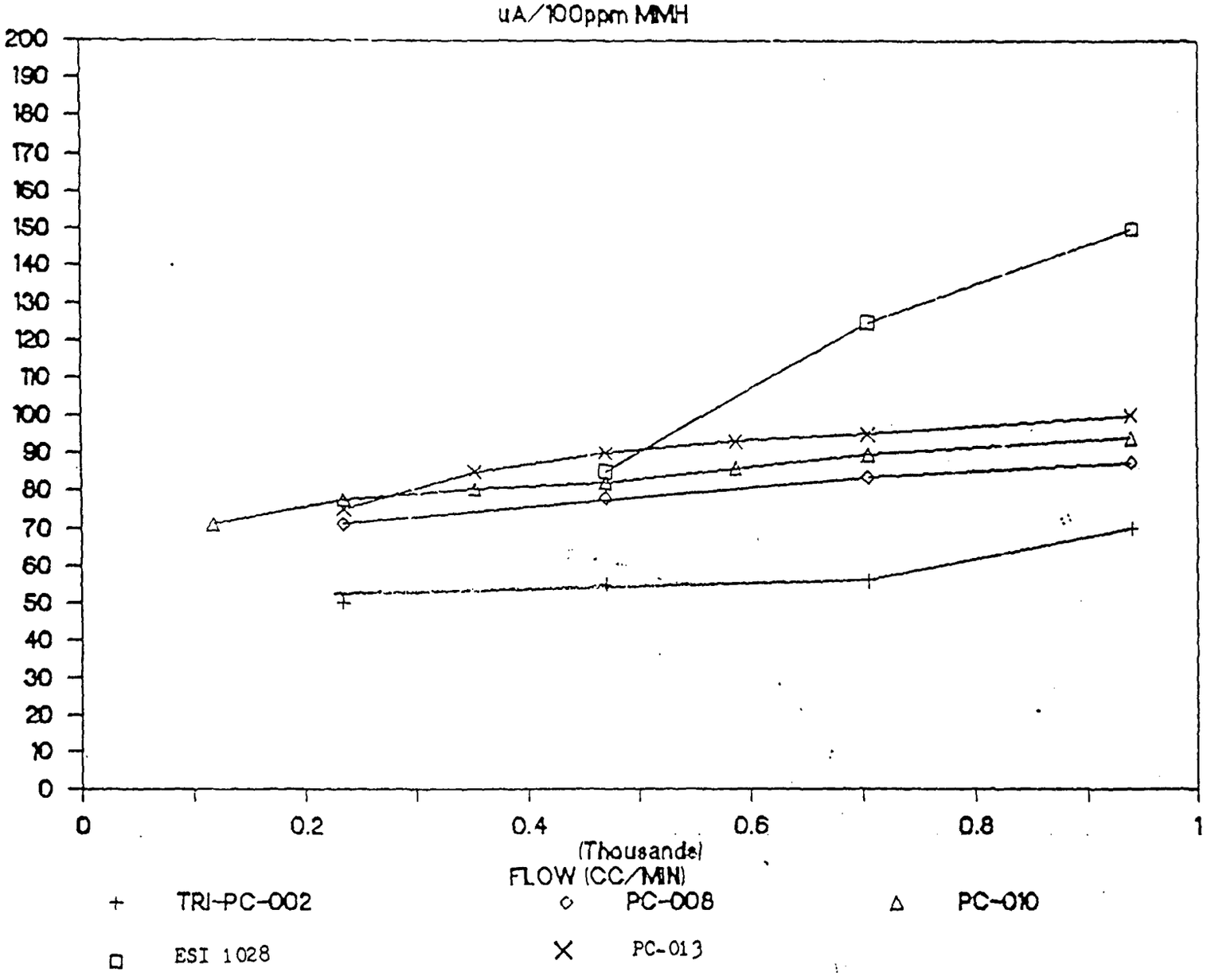

uA/100ppm MMH

GEO-CENTERS, INC.

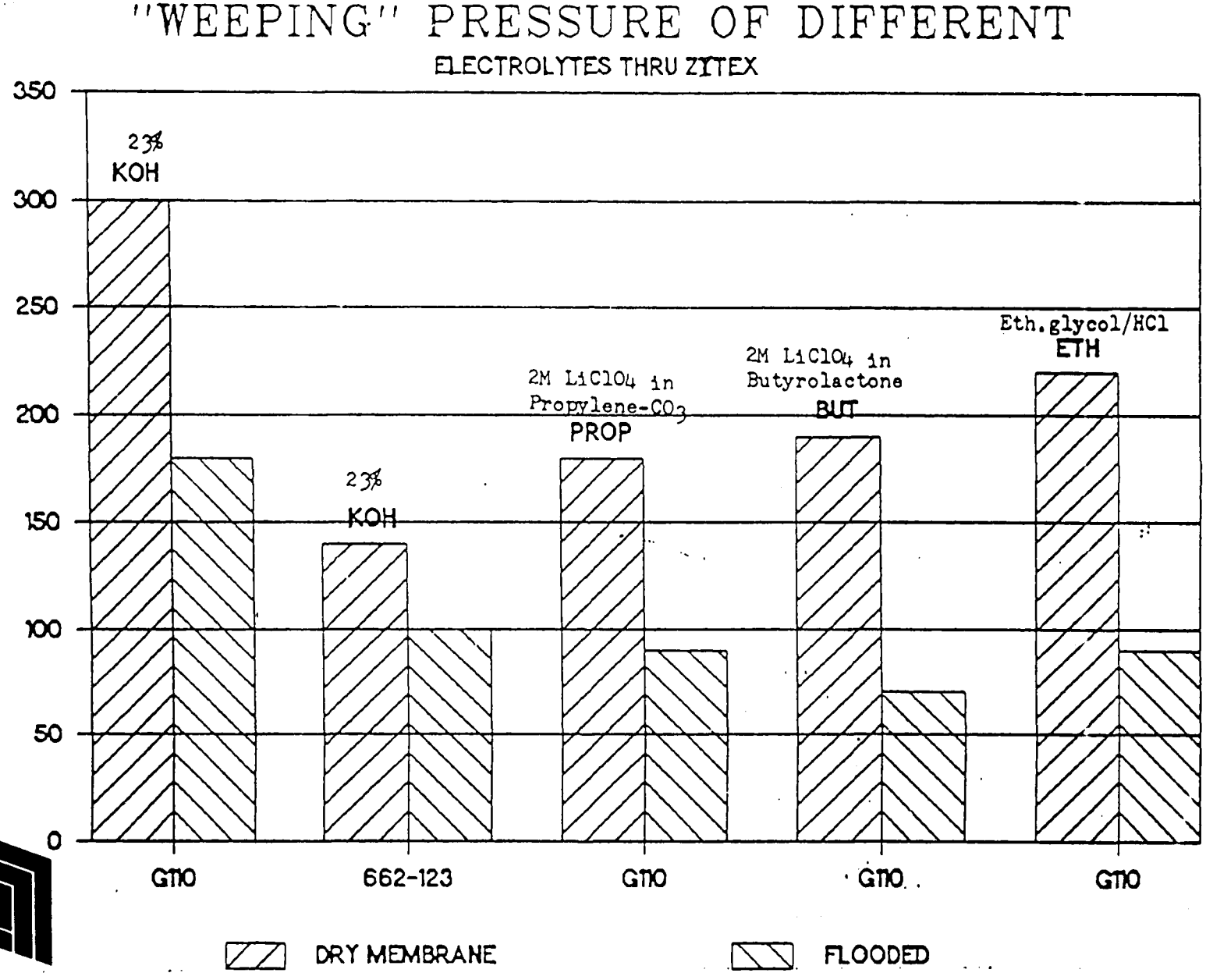

Figure 3.8

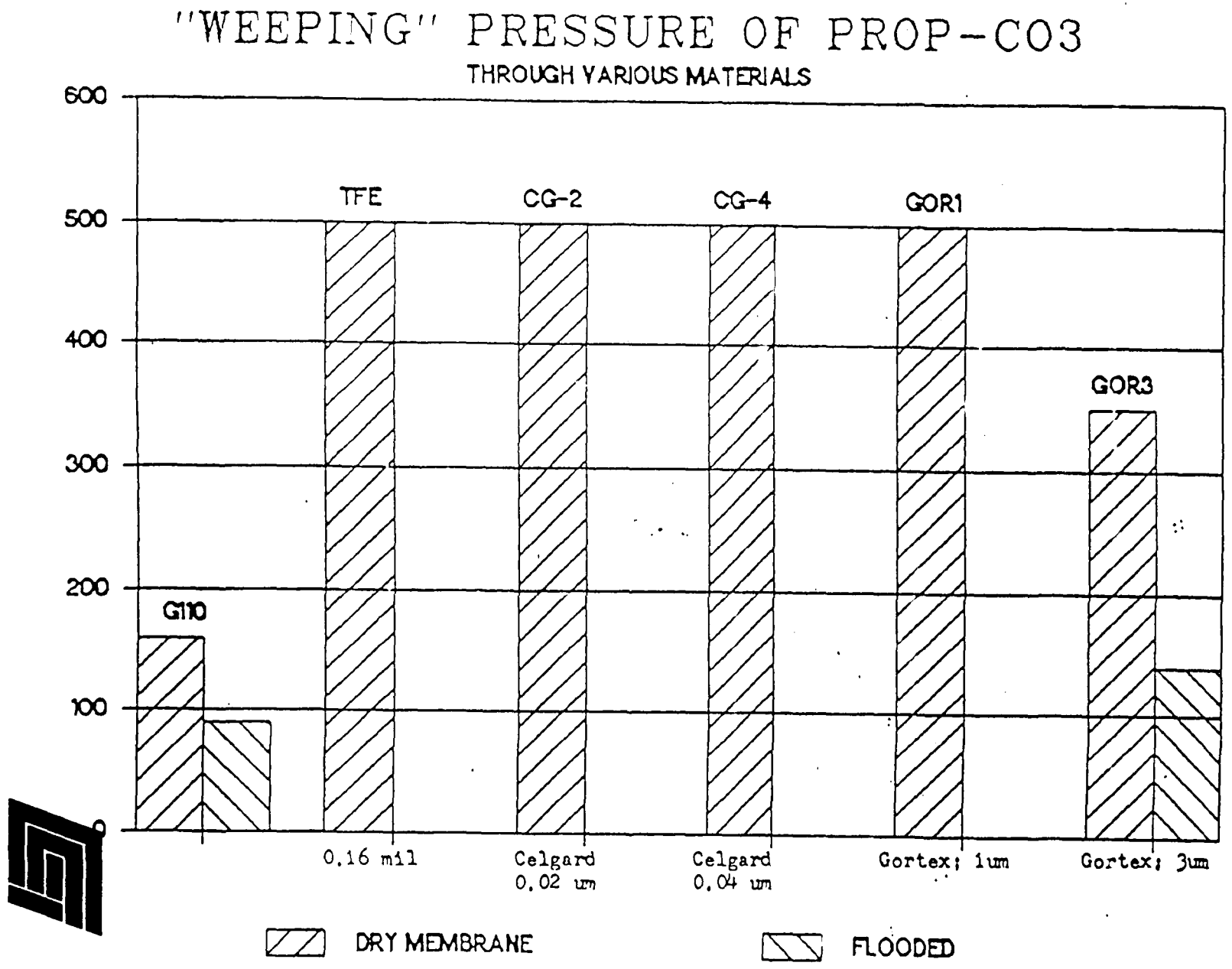

Figure 3.9

GEO-CENTERS, INC.

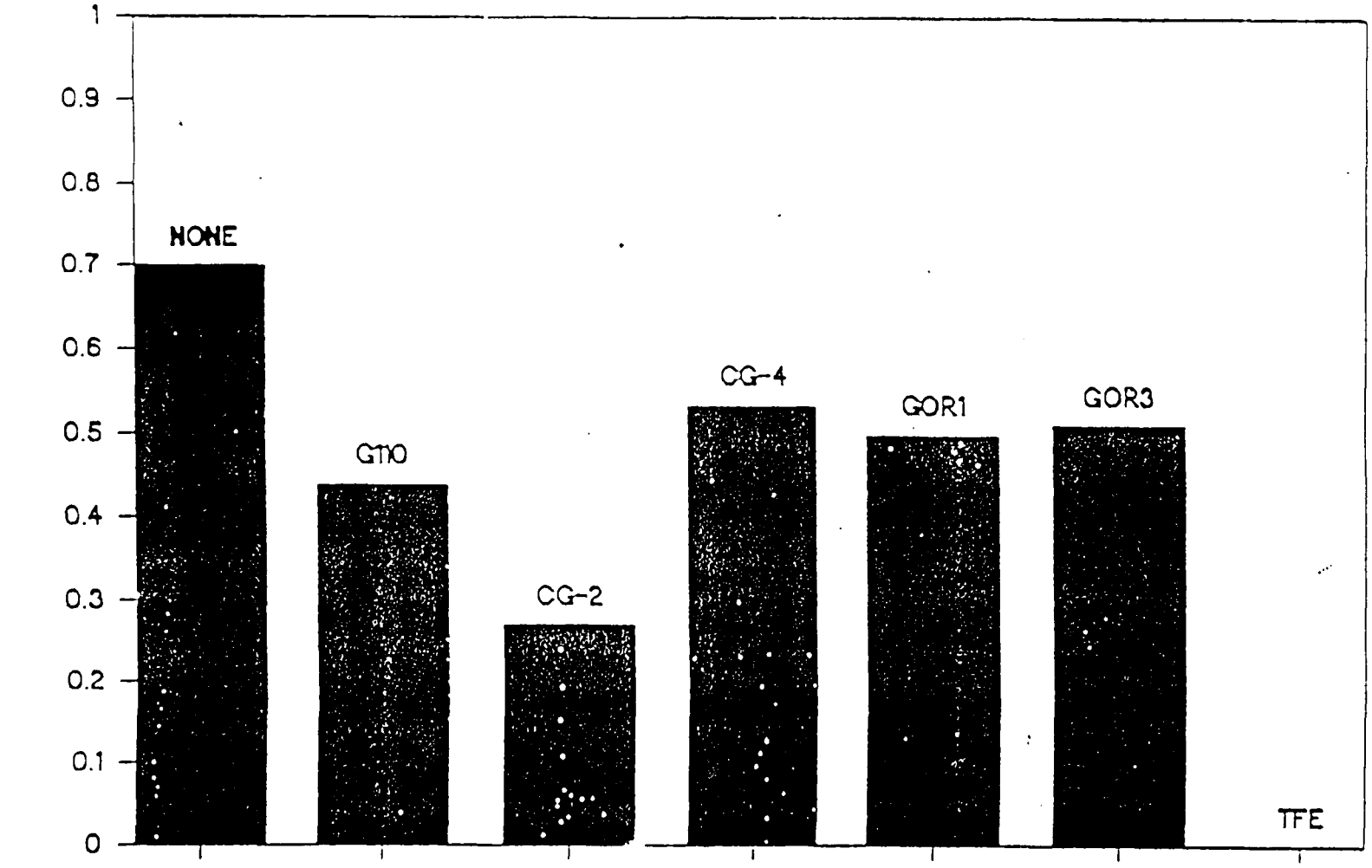

Figure 3.10 (Membrane code same as in Figure 3.9.)

Table 3.3 Prop CO_3 response data.

TRI SENSOR DATA SHEET

SENSOR TYPE AU/ PROPCO3

SENSOR HOUSING TYPE : POLYPRO BUCKET
WE (TYPE/BATCH): V. DEP. AU
CE (TYPE/BATCH): PT BLACK
RE (TYPE/BATCH): PT BLACK
ELECTROLYTE : PROPCO3
BIAS : +100 mV vs. Pt

INITIAL QC DATA: MMH SIGNAL CHARACTERIZATION; 0.5 SCFH

CELL ID	DATE ASSEMB.	TEST DATE	CONC	uA/ppm	BG (ppm)	RISE 90%	DECAY 90%	COMMENTS
PC-001	1/19/87	1/20/87	100.00	1.36	<3.5	<10 SEC	<10 SEC	50 uL SYRINGE
		1/21/87	100.00	2.13	<2.5	10	10	50 uL SYRINGE
PC-002	1/19/87	1/25/87	100.00	0.50	<1.0	60	60	10 uL SYRINGE
PC-004	1/19/87	1/20/87	100.00	1.45	<3.0	10	10	50 uL SYRINGE
		1/21/87	100.00	1.96	<2.5	10	10	50 uL SYRINGE
PC-008	1/19/87	1/20/87	100.00	0.70	<1.0	5	5	10 uL SYRINGE
PC-010	1/23/87	1/25/87	100.00	0.61	<1.0	10	10	10 uL SYRINGE
	1/23/87	1/25/87	100.00	0.46	<1.0	15	10	10 uL SYRINGE; RESP. NOT SHARP
PC-011	1/23/87	1/29/87	100.00	0.70	<3.0	10-15	10	10 uL SYRINGE
PC-012	1/23/87	--						NOT TESTED TO DATE
PC-013	1/23/87	1/29/87	100.00					RECHECK CALCS.

AVERAGE:	1.10
STD DEV:	0.61
AVG(10uL)	0.62
SD(10uL):	0.10

Figure 3.11

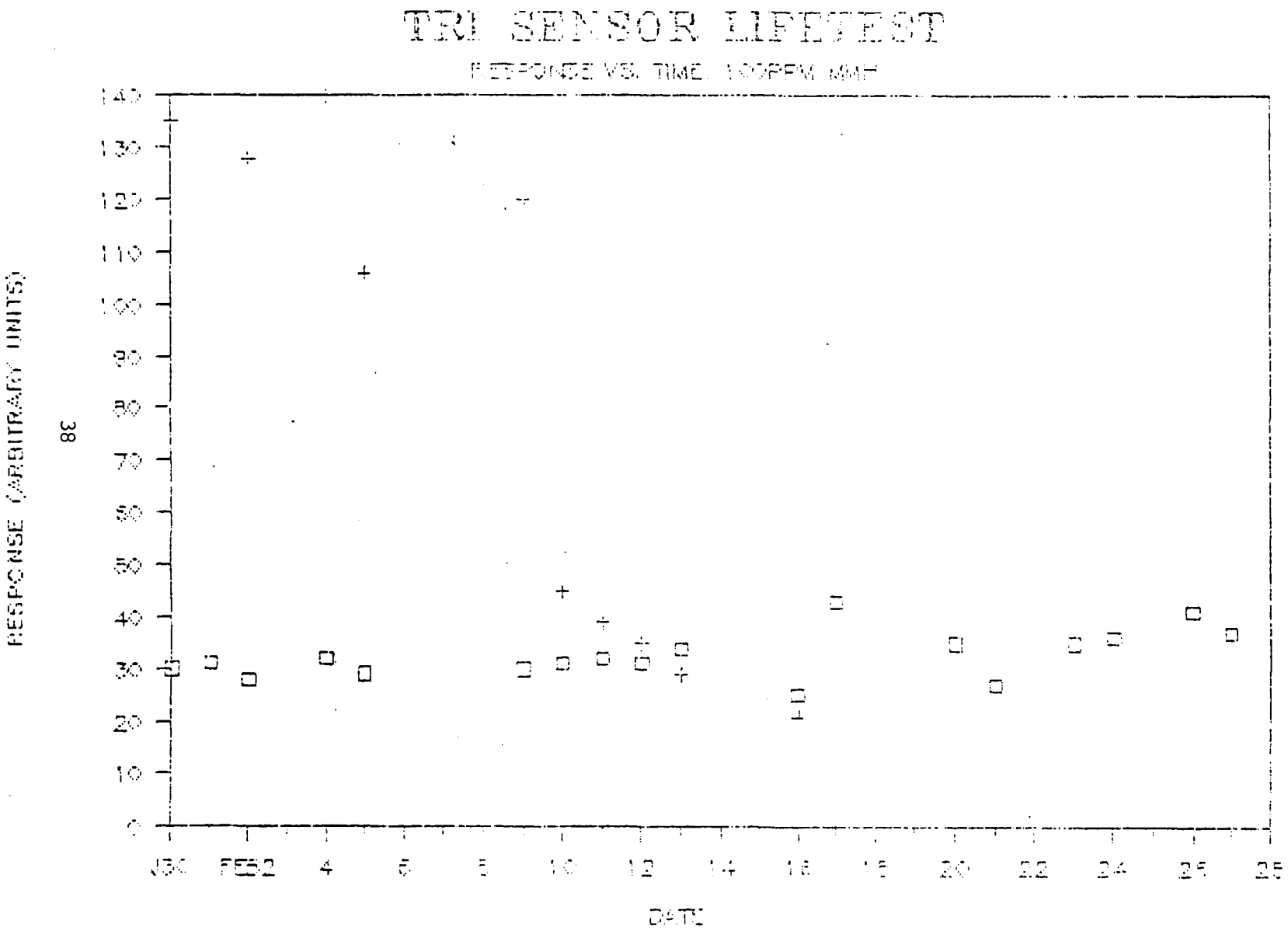
TRI SENSOR LIFETEST
RESPONSE VS. TIME, 100PPM MMH
RESPONSE (ARBITRARY UNITS)
DATE
FEB2
□ PC-008, propylene carbonate
+ PC-007, KOH electrolyte

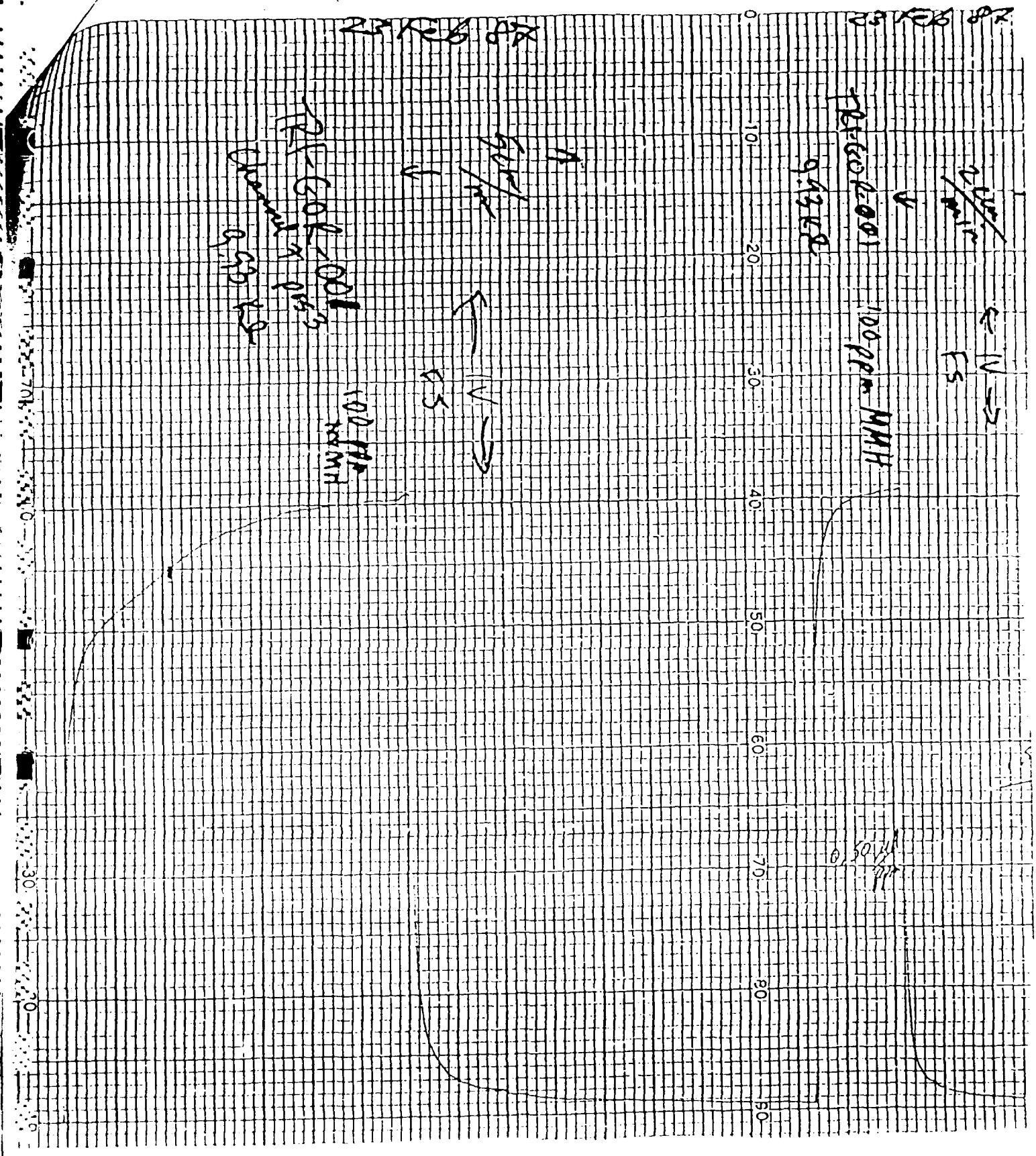

Figure 3.12 Response and Reproducibility for a Gortex Membrance Based Sensor.

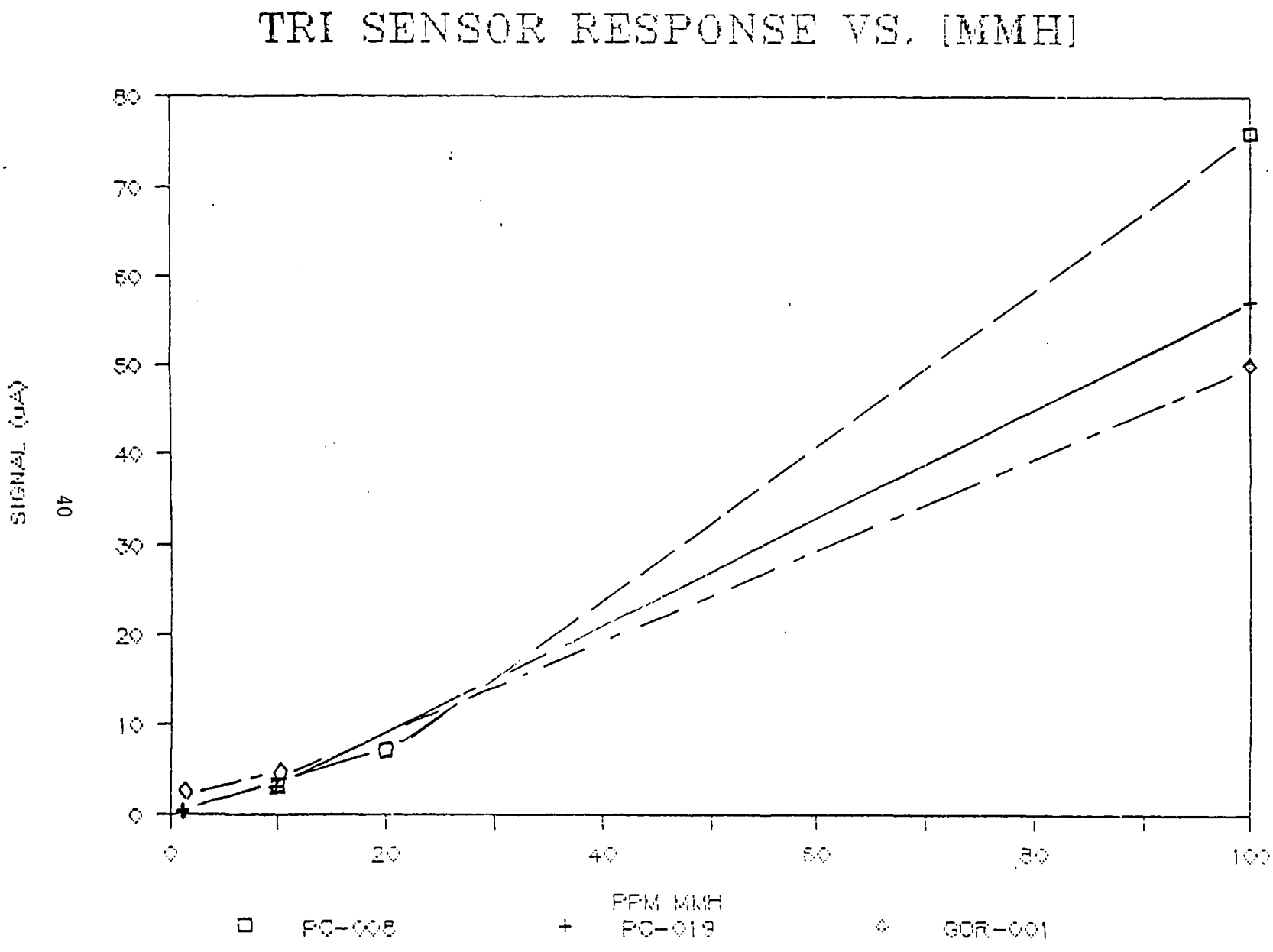
TRI SENSOR RESPONSE VS. [MMH]
SIGNAL (uA)
80
70
60
50
40
30
20
10
0
0
20
40
60
80
100
PPM MMH
PC-008
PC-019
GDR-001

Figure 3.13

4.0 DETECTION OF EXPLOSIVES VAPORS USING OPTOACOUSTIC METHODS

4.1 Introduction

Research programs concerned with detection of explosives have explored two avenues for explosives detection; namely, bulk detection and vapor detection (4.1). The applications of bulk detection techniques include examination of the use of X-rays, NMR/NQR, and neutron activation. Vapor detection techniques include the use of sampling networks, preconcentrators and adsorption tubes for sampling and analysis by the application of mass spectrometric, ion mobility, optical, electron capture/gas chromatography, chemiluminescence, biochemical and olfaction techniques. Recently, the FAA held a workshop to review explosives detection and generate additional approaches to the solution of the problem (4.2). The laser/optical methods working group at this workshop identified three optical techniques as having the most promise for future development as explosive vapor sensors. These techniques are:

- o laser multiphoton ionization (MPI) - based on generation of a small molecular fragment or daughter molecule product of explosives;
- o chemiluminescence - based on the reaction $NO+O_3 \rightarrow NO_2^*$; and
- o Zeeman modulated optoacoustic detection - based on detection of a small fragment molecule characteristic of explosives (e.g., NO)

MPI suffers from the need for elaborate laboratory equipment, high laser power requirements and skilled operating personnel. Instruments for the detection of chemiluminescence are commercially available, although they have not been applied at

the 1 part per trillion (ppt) detection limit needed for explosives detection. The optacoustic technique was therefore selected for development as an explosives detection system. The optoacoustic technique was selected because:

- it has a demonstrated high sensitivity and selectivity for NO;
- it should ultimately have a very fast response time;
- it has the flexibility to be used at any pressure above a few millitorr; thus, system conditions can dictate operating conditions;
- its sensitivity increases with diluent pressure up to 1 atm thus providing the opportunity for efficient sample collection, transfer and changing; and
- it has the potential to be less costly to produce, operate and service.

The optoacoustic detection technique is based on the following principles:

Irradiation of a gas sample within a cell or enclosure by a laser tuned to a vibrational absorption frequency of one of the gas constituents results in vibrational excitation of these molecules. Subsequent collisional de-excitation of these energetic molecules (V-T relaxation) causes a thermalization of the absorbed energy and a pressure rise within the cell. Modulation of the gas absorption generates pressure fluctuations which can be detected with a microphone. If no other absorption artifacts or interferences are present, the acoustic signal generated is proportional to the concentration of absorber molecules in the cell.

The vapors associated with explosives are generally characterized by species containing nitrogen and oxygen (4.3). While there are particular molecules such a nitromethane, EGDN, and nitrotoluenes which are common to several explosives, there is no single vapor that is common to all explosive materials which could be used to design a chemical specific detector. Vapor detection techniques are further complicated by the extremely low vapor pressures associated with many of the explosives in use. It is further recognized that measurements need to be made in the presence of a number of time-varying potentially interfering species that may be present at significant concentrations. Thus, NO, as a derivative produced from decomposition of preconcentrated explosives vapors, represents an attractive means of monitoring the presence of explosives.

An explosives detection system based on application of the optoacoustic technique would have several components; namely,

- A concentration/separation module - the explosive vapors are retained on a suitable substrate while atmospheric NO/NO_2 remain in the vapor. The retained vapors are desorbed into a sample gas stream which is NO/NO_2 free.
- A decomposition module - the explosive vapors are decomposed to fragments containing NO and NO_2. NO_2 is subsequently reduced to NO.
- An optoacoustic cell module - the NO product gas stream flows through a specially designed cell which is continuously irradiated with a low power IR laser tuned to the appropriate frequency. An electromagnet is used to generate a time varying magnetic field which tunes the NO transition in and out of resonance with the laser frequency.

- A detection module - the Zeeman modulated optoacoustic signal is detected, amplified and correlated with the NO concentration in the cell.
- A data processing module - the existence of microprocessors and data processing algorithms allows the raw signal to be manipulated using powerful statistical procedures.

In Section 4.2, optoacoustic theory and experimental design considerations are discussed. Section 4.3 discusses the feasibility experiments that were performed, and Section 4.4 is a summary of conclusions.

4.2 Theoretical and Experimental Design Considerations

A description of the gas phase optoacoustic effect can be separated into four parts; namely,

- heat generation arising from collisions between gas constituents (e.g. NO) that become excited by absorbing photon energy (light) and buffer gas molecules;
- pressure waves generated from expansion of the heated volume;
- losses generated by interaction of the expansion wave with unheated molecules, cell walls, and the microphone. A portion of the microphone contribution to these losses provides the detection signal;
- The signal to noise ratio determines the ultimate limit on detectivity.

Each part will be separately discussed and the implication(s) described.

4.2.1 Heat Generation

The maximum output signal will be generated for the largest number of photons absorbed. This maximum occurs when the largest number of gas molecules are illuminated with the most intense photon beam. Because of practical limitations on laser size, a trade off must be made between light intensity, beam size and number of molecules irradiated. This trade off is seen if one notes that as the light intensity increases due to telescoping of the light beam to smaller sizes, a smaller number of gas molecules are irradiated. One method used to maintain the number of molecules irradiated is to increase the path length of the photon beam through the sample cell. An efficient means of increasing the path length is to design a cell system to accommodate multipass optics. Multipass designs exist which increase path lengths by 10-100 times (4.4-4.8).

One restriction on the light intensity is that it remain below the onset of optical saturation. This is important since no further increases in signal can occur with increased laser intensity once optical saturation has been reached, while interfering signals can continue to increase.

In order to calculate the heat deposition, we shall assume nonsaturation of the molecular absorption which allows a rate equation description of the system. Thus, we wish to describe the time dependent behavior of a molecular excited state, N_1, in the presence of an excess of ground states, N_0. The total number of molecules in the system is $N_t=N_1+N_0$. In the system under consideration, there are two ways to create excited states, photon absorption, R_{01}, and collisional excitation, $k_{01}N_t$. The three ways to convert from an excited state into a

ground state are stimulated emission, R_{10}, spontaneous emission, A_{10}, and collisional relaxation, $k_{10}Nt$. Descriptively, we can write

$$dN_1/dt = -N_1 (R_{10} + A_{10} + k_{10}Nt) + N_o (R_{01} + k_{01} N_t) \quad (1)$$

In Equation (1), R_{01} and R_{10} are time dependent variables. This makes direct integration of Equation (1) difficult.

Maximum detectivity occurs when R_{01} approaches the saturation limit. The relationship,

$$R_{10} = 0.1 (A_{10} + k_{10}N_t) \quad (2)$$

determines the onset of saturation. R_{01} and R_{10} are related through the degeneracy of state 1 and state 0. Also, the excited state relaxation rate, C, where

$$C = A_{10} + k_{10}N_t \approx k_{10}N_t \quad (3)$$

must be at least five times faster than the chopping frequency of the laser. Thus, for a pulse width, W, of a chopped laser beam, CW>5. For NO-Argon mixtures, k_{10} in pressure related units, has been measured (4.9) as $2x10^5$ $atm^{-1}s^{-1}$. Thus, at atmospheric pressure, the pulse width of the laser is restricted to 25 μs or longer.

Under the conditions just discussed, the solution to Equation (1) is a periodic function given by,

$$N_1(t) = (N_0R_{01}/C) \{1-e^{-C(t-2nW)}\} \quad 2nW<t<(2n+1)W \quad (4a)$$

$$N_1(t) = (N_O R_{O1}/C)(e^{CW}-1)\{e^{-C(t-2nW)}\} \quad (2n+1)W<t<2(n+1)W \qquad (4b)$$

where n is the period number (1,2,3....).

From these equations, we note that the population difference during one laser pulse is given by

$$N_1\{(2n+1)W\}-N_1(2nW)=N_O R_{O1}/C \qquad (5)$$

The heat generated, H, is calculated from

$$H = (N_O R_{O1}/C)C(h\nu)V_L W \qquad (6)$$

where hv is the photon energy or the quantity of energy released by each excited molecule and V_L is the volume of gas swept out by the laser beam. Assuming one ppb NO in one atmosphere of argon with N_O = 2.46×10^{10} molecules/cm^3, $R_{01}=1.95\times10^4 s^{-1}$, $C=2\times10^5 s^{-1}$, h $=3.7\times10^{-13}$ ergs, $V_L=0.124$ cm^3 and W=1/2x6150 Hz, the heat generated is calculated as $H=8.58\times10^{-3}$ ergs. At the cell wall, where the microphone is located, the energy density in the pressure wave, is calculated as,

$$p = H/V \qquad (7)$$

where V is the cell volume, for a cell volume of 201 cm^3 the energy density is 1.78×10^{-5} ergs/cm^3 or 1.34×10^{-8} torr/cm^2.

4.2.2 Pressure Wave

As noted earlier, the heat produced acts as the source for a pressure wave which expands from the locally heated volume at the speed of sound, V_S. The differential equation that describes sound production is given by (4.10),

$$\nabla^2 p - (v_s^{-2})\delta^2 p/\delta t^2 = -\{(\gamma-1)/v_s^2\}\delta H/\delta t \qquad (8)$$

where $\gamma = C_p/C_v$ is the ratio of the constant pressure heat capacity to the constant volume heat capacity. Equation (8) ignores acoustic losses. These losses can be added as perturbations (see Section 4.2.3). The plane cylindrical wave solution to the homogeneous part of Equation (8) ($\delta H/\delta t=0$) is

$$p(r) = \Sigma_{kmn}\, J_m(\alpha_{mn} r/R)\, \cos(k\pi z/L)\, \begin{Bmatrix} \sin(m\phi) \\ \cos(m\phi) \end{Bmatrix} \qquad (9)$$

The choice of sin or cos is dependent on the positioning of the microphones and the excitation beam and our definition of axis coordinates.

The frequency at which a resonance occurs is given by

$$\omega_{kmn} = v_s \sqrt{\frac{\alpha_{mn}^2}{R} + \frac{(k\pi^2)^{1/2}}{L}} \qquad (10a)$$

$$\nu_{kmn} = \frac{v_s}{2\pi} \sqrt{\frac{\alpha_{mn}^2}{R} + \frac{(k\pi^2)^{1/2}}{L}} \qquad (10b)$$

Note that care must be taken when comparing nomenclature in different literature references. Some authors use the boundary condition $J'(\pi\alpha_{mn})=0$ at $r=R$ and use tables for which $J'(\pi\alpha_{mn})=0$ at $r=R$ and use tables for which α_{mn} is divided by π. Thus, their equation is writen as,

$$\nu_{kmn} = \frac{v_s}{2} \sqrt{\frac{\alpha_{mn}^2}{R} + \frac{(k\pi^2)^{1/2}}{L}} \qquad (10c)$$

To determine the resonance frequencies, we shall use Equation (10b) and the tables in Reference 4.11. The ordering of the subscripts is not sacrosanct, it appears in all permutations in the literature.

A physical description of the resonance modes defined by Equation 9 provides guidance in determining microphone placement and mode intensity. The product of the r, ϕ, and z distributions defines the pressure distribution for a specific kmn mode. Plots of the three functions and schematic pictures appear in Figure 4-1, (J_m); Figure 4-2, (cos mϕ) and Figure 4-3, (cos kπz/L). Figure 4-1 and Figure 4-2 are related because of value of m in cosmϕ specifies which Bessel function describes the radial dependence. Note that the cell walls must occur at minimum or maximum points of the J_m plots due to the vanishing of the acoustic velocity at the walls. These minimum and maximum points are numbered as to the value of n in the plots of Figure 4-1.

The azimuthal angle, ϕ, dependence is doubly degenerate for M>1 because either a cos or sin function satisfies Equation 8. However, the degeneracy disappears upon placement of the first microphone and choice of coordinate zero. Once this microphone is positioned the m solutions are restricted to cos terms since the pressure wave must be a maximum at the microphone and we define 0° to be in the vertical direction. The choice of mode and excitation beam position then determines optimum placement for any additional microphones. For example, a second microphone should be placed opposite the first when detecting the m=1 mode with on-axis excitation.

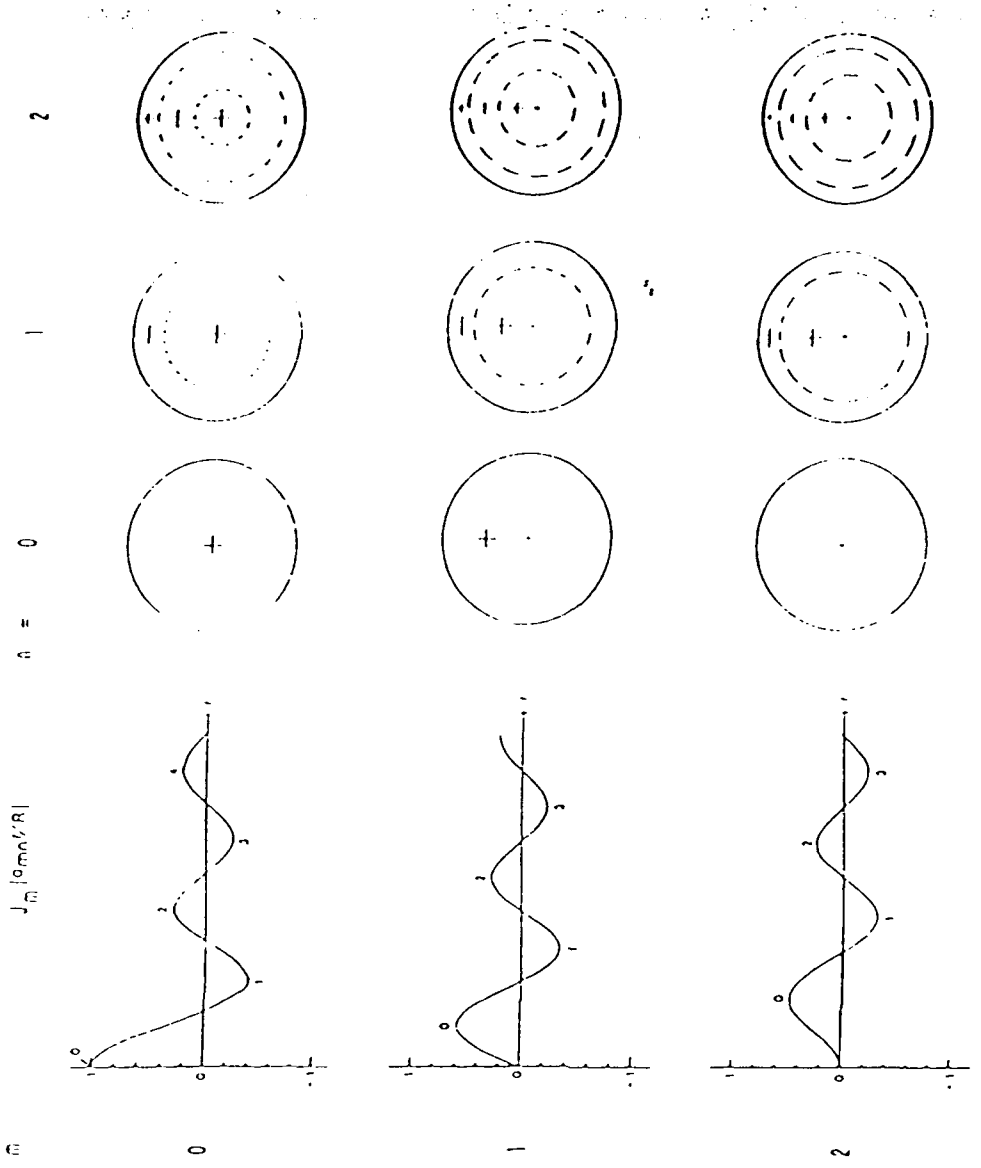

Figure 4-1. A pictorial representation of the radial variation of several standing pressure waves in a cylindrical cell. The standing wave amplitudes at any radial point (r) are proportional to a Bessel function evaluated at α_{mn} r/R when the value of R is set by the cylinder radius. α_{mn} is the n^{th} zero of the derivative of the Bessel function J_m. These zeros must occur at the cylinder wall. The value of r=R for the lowest four values of n is designated on each Bessel function plot. Note that for m 0 there exists a node along the cylinder axis. This is represented by a black dot. The complete standing wave amplitude pattern is given by the product of the radial (Figure 4-1), azimuthal (Figure 4-2), and longitudinal (Figure 4-3) descriptions.

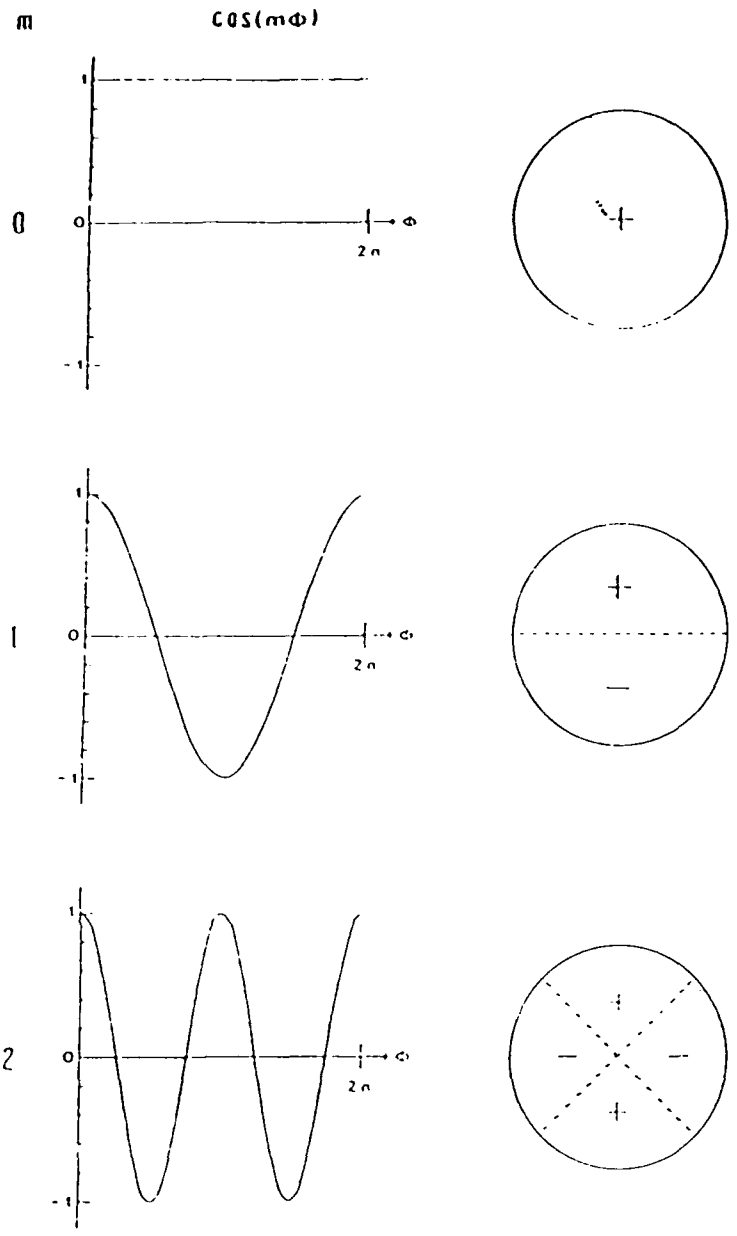

Figure 4-2. A pictorial representation of three azimuthal standing wave patterns. We have chosen the cosing function to represent our experiment and defined zero degrees as a vertical direction. Note that the azimuthal eigenvalue m determines which Bessel function J_m represents the radial distribution of standing wave amplitudes depicted in Figure 4-1. The complete standing wave amplitude patter is given by the product of the radial (Figure 4-1), azimuthal (Figure 4-2), and longitudinal (Figure 4-3) descriptions.

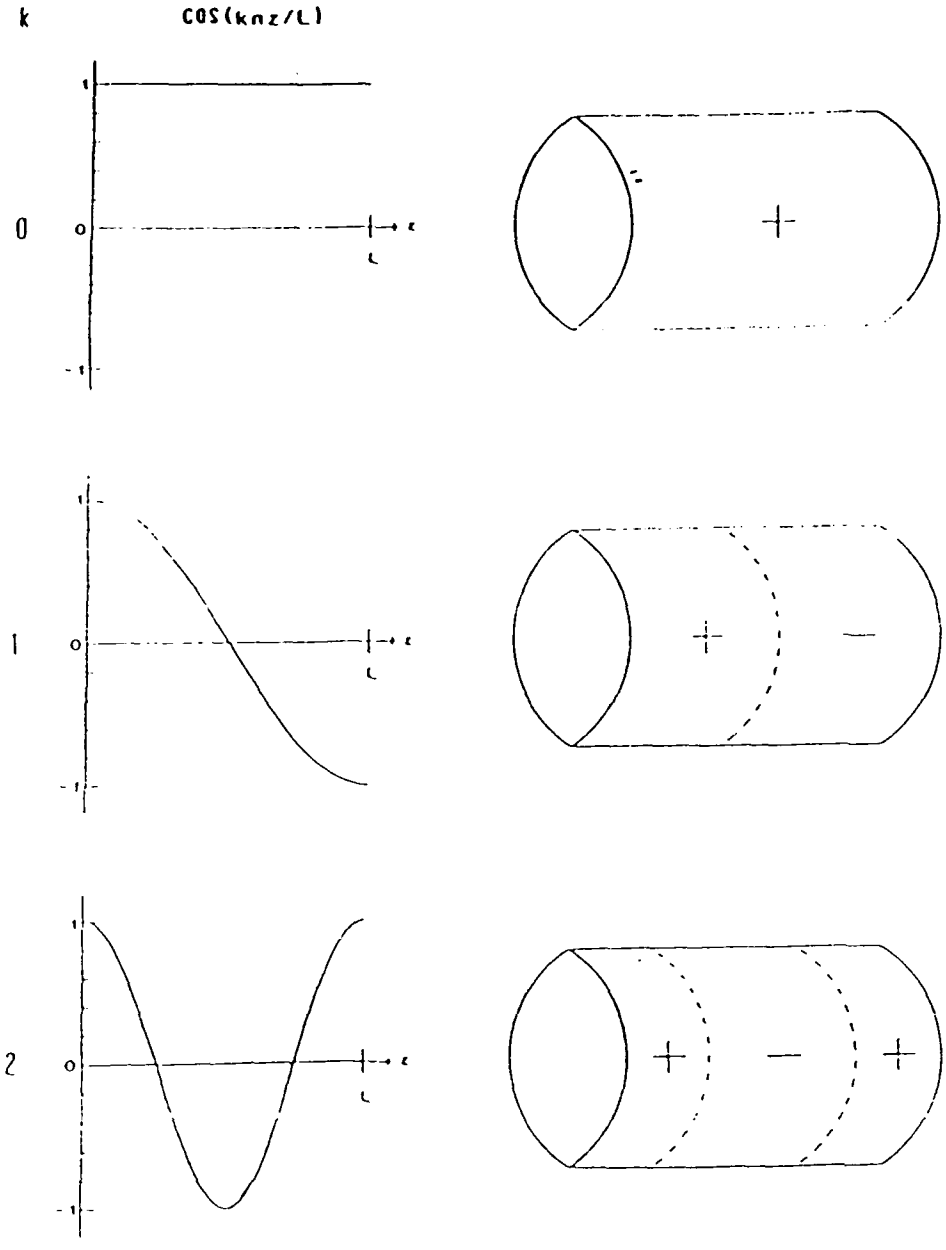

Figure 4-3. A pictorial representation of three longitudinal modes for k=0,1,2. For small absorptions most of the acoustic energy is deposited into the k=0 mode. The complete standing wave amplitude pattern is given by the product of the radial (Figure 4-1), azimuthal (Figure 4-2), and longitudinal (Figure 4-3) descriptions.

The generalized solution to the Equation 8 can be written as

$$P(r,\omega)=\Sigma_{kmn}A_{kmn}(\omega)\cdot P_{kmn}(r) \qquad (11)$$

where $A_{kmn}(\omega)$ are the mode amplitudes (related to intensity) and $P_{kmn}(r)$ describes the spatial distribution of the pressure wave. To ensure that the mode amplitudes remain finite, loss terms, expressed as damping factors, are included as perturbation terms in Equation 8. When these losses are included, the mathematical form of the mode amplitudes is

$$A_{kmn}(\omega) = \frac{-i\omega(\gamma-1)\ p_{kmn}H\ dr}{(\omega_{kmn})^2V[-1(\omega/\omega_{kmn})^2-(i\omega/\omega_{kmn}Q_{kmn})\}} \qquad (12)$$

where Q_{kmn} represents the sum of the losses. Losses due to viscosity, thermal conductivity, cell material, wall roughness, etc., determine the magnitude of Q. These losses are discussed further in Section 4.2.3.

We see from Equation (12) that setting k=0 and $\omega=\omega_{kmn}$ gives A_{kmn} 1/(ωV). From Equation (10b), ω 1/R and V R2. Overall A_{kmn} 1/R. Thus, the minimum cell radius provides the maximum mode amplitude (signal). However, other limitations include the frequency response and physical size of the microphone and the restriction that CW>5. For the case of NO-Argon at one atmosphere, we have already calculated a lower limit on the pulse width of 25μs which translates into a ceiling on the chopping frequency (50% duty cycle) of 20 kHz. Use of Equation (10b) sets a lower limit on R of 0.9 cm.

4.2.3 Losses

Energy dissipation from an acoustic wave is characterized as either from volumetric losses or as due to surface effects. Volumetric losses, which arise because the sound wave departs from equilibrium, include viscous and thermal dissipation and collisional relaxation. Viscous and thermal dissipation, known collectively as Stokes-Kirchoff losses (4.10), occur when the sound wave has a portion of its energy converted into dispersed heat (thermal loss) or a portion of its directed motion converted into random motion (viscous loss). Stokes-Kirchoff losses, Q_{SK}, are calculated from

$$Q_{SK}^{-1} = \frac{\omega}{\gamma P_O}\left(\frac{4}{3}n + (\gamma-1)\frac{k}{C_P}\right) \qquad (13)$$

where P_O is the total system pressure, n is the viscosity and k is the thermal conductivity.

Relaxation losses occur because thermally excited molecules release their energy into vibrational or rotational excitation of a collision partner. Such a loss mechanism is frequency and pressure dependent, but can readily be calculated (4.12, 4.13). As long as one uses a monatomic buffer gas and high dilution ($>10^3$), collisional relaxation losses do not contribute to the volumetric loss term.

Surface effects usually dominate the loss terms. Wave scattering into random directions by surface imperfections, viscous and thermal dissipation at the walls, energy extraction by the microphone(s) and energy absorption due to wall compliance

all contribute to surface effect losses. Theory is presently not available to calculate the degree of smoothness, ripple, planarity, etc., which chamber walls must have. However, based on optical principles, imperfections less than 1/10 the sound wavelength can be neglected. Since all other losses are calculable, scattering losses can be determined by comparing experimental and theoretical values of Q.

Viscous and thermal dissipation at the walls arises because the gas away from the walls behaves adiabatically, while the walls are isothermal. Losses occur across the boundary isothermal layer. The theory for the fractional loss per cycle has been developed for on-axis excitation in a cylindrical chamber. The result in terms of Q, is (4.14)

$$Q_{sur}^{-1} = \frac{1}{L}\, d_v + (\gamma - 1) d_h (1 + L/R) \qquad (14)$$

where d_v, the viscous boundary layer, is given by $(2\eta/\rho_o M\omega)^{1/2}$; d_h, the thermal boundary layer, is given by $(2K/\rho_o MC_p\omega)^{1/2}$; ρ_o is the density of the gas and M is the gram atomic weight of the gas.

Wall compliance or reflection losses are also readily calculable. They are a function of the wall stiffness, gas density and sound velocity (4.10). However, for a rigid nonporous wall, reflecting at normal incidence, essentially no energy is absorbed by the wall.

The microphone(s) removes energy from the standing wave in both usable (signal) and non-usable (loss) form. Thus, a more

sensitive microphone or greater numbers of microphones extract an ever increasing portion of the sound wave's energy. This decreases the Q factor which appears in Equation (12) which also decreases the mode amplitude (signal). At greater than 50% energy extraction, the summed energy output from the microphones begins to decline due to the non-usable losses each microphone introduces.

For trace amounts of NO mixed with a rare gas such as Argon or Xenon, Stokes-Kirchoff, surface scattering and boundary layer effects constitute the primary loss factors. Table 4-1 lists the parameters needed to calculate these losses. Substituting the appropriate values from Table 4-1 into equation (4.13) gives $1/Q_{sk} = 1.16 \times 10^{-5}$ and 4.72×10^{-6} for Argon and Xenon, respectively. Substitution into Equation (14) gives $1/Q_{sur} = 1.41 \times 10^{-3}$ and 7.32×10^{-4} for Argon and Xenon. Summing $1/Q_{sk}$ and $1/Q_{sur}$ for Argon and Xenon yields Q=704 and 1360, respectively, These loss values will be compared with experimental values in Section 4.3.

TABLE 4-1

Parameter Values for Calculating Losses

Buffer gas parameters necessary in the calculation of resonant acoustic wave losses as predicted by Equation 13 and Equation 14. The definitions of the various parameters appear in the text.

Parameter	Value[a]		Units
	Ar	Xe	
P_o (1 atm)	1.01×10^{6}		dyne cm^{-2}
	2.46×10^{19}		molecules cm^{-3}
M	6.64×10^{-23}	2.18×10^{-22}	g $molecule^{-1}$
$\omega 001$	3.86×10^{4}	2.12×10^{4}	rad s^{-1}
	S/3		
η	2.27×10^{-4}	2.31×10^{-4}	g cm^{-1} K^{-1}
κ	1.63×10^{3}	5.15×10^{2}	erg cm^{-1} s^{-1} K^{-1}
Cp	5.2×10^{6}		erg g^{-1} K^{-1}
L = 2·R	R=3.175		cm

a Thermodynamic values are obtained from Reference 4.15.

4.2.4 Noise

Two classes of noise occur for signals being processed with phase sensitive detection; namely, coherent and incoherent noise. Coherent or in-phase noise appears at the detector input with a constant phase relationship to the signal. Incoherent or random noise appears at the detector input with varying phases. Since the detector cannot distinguish between coherent noise and signal, any in-phase noise (i.e. interfering signal) must be smaller than the minimum detectable signal. The most important feature of our experimental design is that it shifts the coherent noise away from the detection frequency by employing a double modulation technique. In single modulation schemes, heat deposited into the sample cell due to window absorption and absorption by species other than NO will occur in-phase with any NO absorption. When only Zeeman modulation of the NO resonant frequency is used, pickup induced in the microphone and its leads by the alternating magnetic field will appear in-phase. With double modulation, all these noise sources are shifted away from the detection frequency. Consequently, any sources of coherent noise at the detection frequency must be due to molecules that absorb the CO laser radiation and Zeeman modulate at the same rate as the NO.

There are many sources of incoherent noise. These sources include room pickup, Johnson noise, turbulence, Brownian motion, and 1/f noise. Minimizing turbulence and 1/f noise were considerations in selecting the size of the sample cell. A relatively small cell boosts the detection frequency into the kilohertz regime where the 1/f noise is small. Turbulence noise

is kept small at the higher frequencies by slowing the gas flow rate through the cell and locating the gas ports at positions where nodes occur in the acoustic standing wave.

Noise (pressure) from Brownian motion (thermal noise) P_T, can be calculated from (4.16)

$$P_T(\text{torr}/\sqrt{\text{Hz}}) = 4\gamma P_0 k_B T Q/(v)^{1/2} \qquad (15)$$

where k_B is Botlzmann's constant. For the cell used in our experiment, Q=410, P_0=700 torr, V=201cm^3, ω=6150 Hz and γ=5/3. P_T is calculated as 7.02 x 10-9 torr/$\sqrt{\text{Hz}}$ which provides 9.3 nV/$\sqrt{\text{Hz}}$ of thermal noise (V_T) from our microphone.

Johnson noise can be calculated from (4.17)

$$V_J=(4k_B T R_S \Delta f)^{1/2} \qquad (16)$$

where R_S is the equivalent source resistance connected across the amplifier inputs. The Knowles microphones used in our experiments have a maximum output impedance of 2.5 kΩ. Therefore Johnson noise contributes 21nV/$\sqrt{\text{Hz}}$, a factor two greater than the thermal noise.

The final noise sources to be considered are pickup of acoustic noise and electromagnetic (e/m) noise from the room. Isolation of the cell from mechanical vibrations is accomplished by using alternate layers of stiff, dense material and soft, flexible material and by vibration isolation tables. Acoustic isolation is achieved by employing layers of lead and foam and surrounding the cell with a vacuum chamber. Electromagnetic noise is reduced through careful but straightforward shielding

techniques. Experience with phase sensitive detection indicates that signals can be detected at signal to incoherent noise ratios (S/N) of 1/100.

4.3 Experimental

Optoacoustic sensing of NO at the parts-per-trillion (ppt) level represents a need for sensitivity improvement of two orders of magnitude relative to the present state-of-the-art limit. This level of improvement requires that the detector be optimized with respect to all parameters that can either increase signal or decrease noise. For the present phase of the work, a number of the parameters that influence signal and/or noise were investigated using two different experimental setups. The parameters investigated with each apparatus are listed in Table 4-2. The two setups allow independent examination and optimization of the sample cell design and the gas composition and noise sources.

4.3.1 Cell Design

Figure 4-4 depicts the experimental apparatus used to examine the first five items listed in Table 4-2. The laser employed is a continuous wave CO_2 laser capable of being line tuned with a diffraction grating throughout the 9.5μm band (00°2)-(02°0) P branch. We chose the P(16) line at 9.52 μm because it provides the highest output power. The laser beam is mechanically chopped in a frequency range between 5 Hz and 17 KHz. The optoacoustic cells are Plexiglas cylinders (0.64 cm thick) with 2.54 cm thick Plexiglas end plates. Sodium chloride windows are mounted into the end plates such that the inner surface of the window is flush with the inner surface of the Plexiglas end plate. Thus, only a small annular grove around the

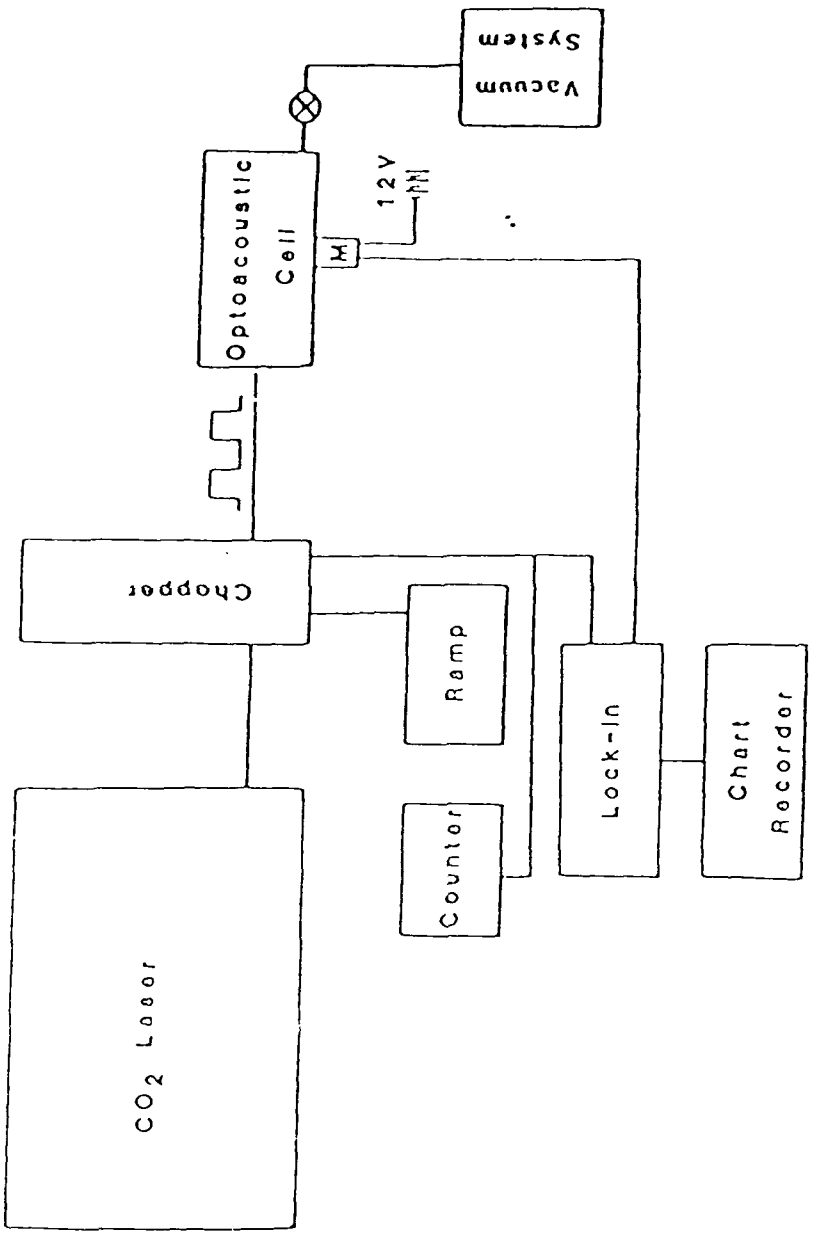

Figure 4-4. A schematic diagram of the apparatus used to measure cell design characteristics. The equipment consists of a continuous wave CO_2 laser which is grating tunable, a mechanical chopper operating between 5Hz and 17kHz, a plexiglas optoacoustic cell with a Knowles CA-1832 microphone flush mounted in the cell wall and signal processing electronics.

TABLE 4-2

Parameters Investigated with a Given Experimental Set-up

Cell Design
Cell Size
Surface Roughness
Mode Intensity
Excitation Position
Multiple Microphones
Gas Composition and Noise Sources
Total Gas Pressure
NO Partial Pressure
Buffer Gas Composition
Magnetic Field
Acoustic Isolation
Electromagnetic Field Isolation

window can cause acoustic wave scattering losses. The microphone(s) is mounted as flush as possible with the cylinder wall. Since the microphone surface is flat, even 0.64 cm diameter microphones protrude 1 to 2 mm beyond the cylindrical cell walls at microphone center. A small hole is left beside the microphone and the microphone cavity is sealed to allow for pressure equalization. The first microphone is placed at the midpoint of the cylinder's length. Additional microphones positions are dictated by the choice of excitation position and selection of the resonant acoustic mode. Knowles CA-1832 microphones are chosen because they are small in size, battery powered, have good sensitivity (1.32 mV/mTorr) and low noise. The output of the microphone is connected to a phase sensitive detector (Princeton Applied Research, Model 124) capable of band-pass filtering at Q_{PSD}=100 and with a maximum sensitivity of ~10nV. A function generator (Hewlett Packard 3010B) capable of ramp generation sweeps the mechanical chopping rate. The electrical output from the chopper is used as a reference for the phase sensitive detector system. With this apparatus, one atmosphere of neat SF_6 allows the monitoring of the greatest number of acoustic resonances for a given cell size. The parameters investigated allow the signal to be maximized with respect to the various cell characteristics.

4.3.1.1 Cell Size

In resonant optoacoustic detection, the cell radius determines the modulation frequency as long as we work with radial and azimuthal modes. A minimum radius (R=0.9cm) is set by the collisional relaxation rate, C. The two main loss mechanisms exhibit frequency dependence; however, their effects are minimized for a given radius, L=2R. The other restriction on

cell size derives from conservation of energy in the pressure wave. As it expands, the total energy remains constant. However, the surface area of the expanding cylindrical wave increases with R^2. This lowers the energy density by a factor of R^{-2}, thus driving R toward its minimum value (maximum ω). Eventually the cell becomes so small that energy is lost from the standing wave by scattering from microphone surface as that surface becomes a major perturbation to the cell wall.

Experimentally we monitor the intensity of the 001 and 002 modes for cells of various lengths having radii of 9.52, 6.98, 3.81, and 3.17 cm. Varying L at fixed R results in 10-20% signal losses for 60% changes in L away from the L=2R signal maximum. Each decrease in R for L=2R results in an ~15% increase in signal except that the 3.81 and 3.17 cm radius cells showed no change in signal.

4.3.1.2 Surface Roughness

Since the detection scheme relies on a modulated magnetic field, the cell materials are restricted to non-magnetic and non-conductive ones. This limits the choice of materials to glass, ceramic, or plastic. We test the effects of surface roughness on signal strength using Plexiglas cells which are easy to machine and bond.

In one experiment a coil of nichrome wire was inserted into the cell and allowed to expand until it pressed firmly against the cell walls. The sound wavelength is 6 cm. The wire diameter is 0.4 mm and the spacing between loops is 7 mm. Under these conditions we observed a maximum 10% decrease in signal. With the sound-wavelength to roughness-width ratio of 150,

minimal signal loss is expected. Later measurements bear out these results. The close correspondence between the measured loss in the original cell (Q=685) and the predicted value (Q=704) indicates that "off-the-shelf" surface preparation is adequate for Plexiglas cells.

4.3.1.3 Mode Intensity

The mode amplitude predicted by Equation (12) has an inverse frequency dependence; thus, the 010 or 001 mode should provide the largest signals. We have experimentally verified the strengths of the various modes. Figure 4-5 shows the signal strength measured as the frequency of the chopper is varied from 700 Hz to 7 kHz. The strongest modes are the 00n modes followed by the 01n modes. The modes are identified by comparing the measured frequencies with those calculated using Equation (10b).

The intensity difference between the 00n progression and the 01n progression can be understood by referring to the Bessel function plots in Figure 4-1. The overlap integral can be pictured as the product of a thin vertical rectangle, the laser beam, and the appropriate Bessel function. When the laser beam coincides with the cell's longitudinal axis it can be pictured as surrounding the r=o region of these plots. Clearly the overlap with J_0 is nearly 100% while the overlap with J_1 is nearly zero.

The two small peaks at 729 and 1336 Hz arise from the square wave beam modulation employed. The Fourier component of the chopper frequency at 3ω excites the acoustic resonances at 2189 and 4010 respectively. The fact that the intensity ratio is not the expected 3:1 gives some feeling for the degree to which our excitation function deviates from being a square wave.

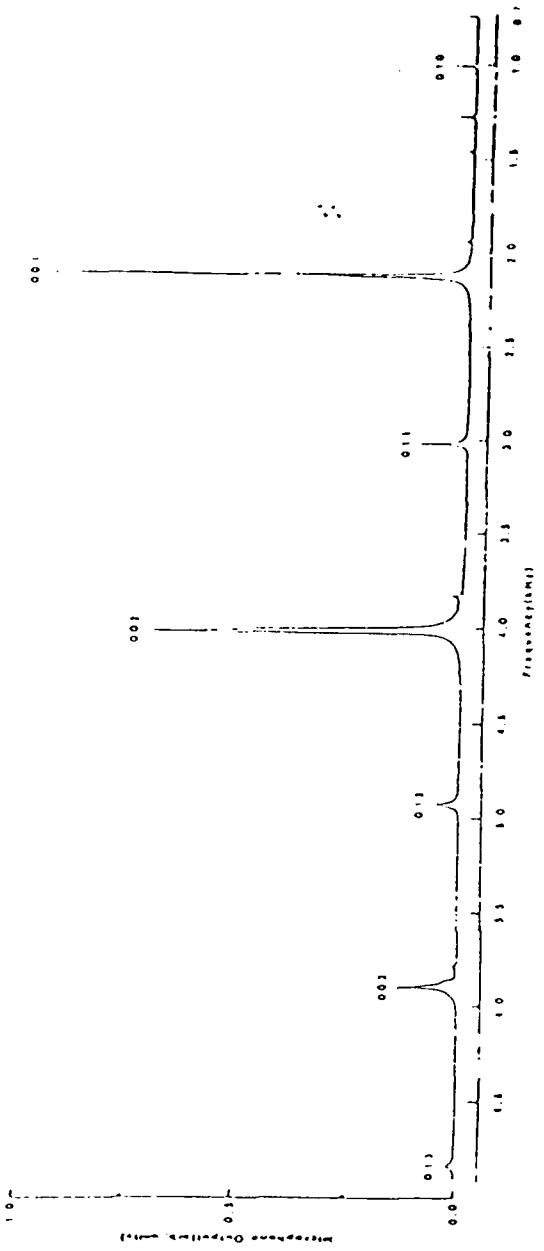

Figure 4-5. Acoustic resonant mode structure measured with on-axis excitation. The cell is a cylinder 7.62cm long and 7.62cm i.d. Experimental conditions are 700 torr of neat SF_6 irradiated at 9.52μm with 2W of laser power. The vertical scale is the same as in Figure 4-6.

4.3.1.4 Excitation Position

The overlap integral, $\int P_{kmn} H \, dr$, determines the coupling of the heat input into the standing wave. From the pictorial description of the radial portion of the standing wave (Figure 4-1), we see that on-axis excitation couples mainly with m=0 modes. At least 60% of the input energy cannot be transferred to the microphone since $|J_0(0)|=1.0$ while $|J_0(3.83)|=0.4$. As an alternative one might try coupling to the m=1 modes by passing the laser beam along one cell wall and listening at the opposite wall. In this case, the heat coupling is decreased from $|J_0(0)|=1.0$ to $|J_1(1.8)|=0.6$. However, the pressure at the microphone is also given by $|J_1(1.8)|=0.6$. The result of an on-axis excitation appears in Figure 4-5. Contrast that spectrum with the opposite wall excitation spectrum given in Figure 4-6. Notice that the mode strengths change dramatically. The most intense mode in the on-axis excitation is 001 while the off axis excitation deposits the most energy into 010. Comparison of the strengths shows that the 001 mode provides ~10% more signal than its 010 counterpart.

4.3.1.5 Multiple Microphones

Maximum sensitivity coincides with the optimum energy extracted from the standing wave by the microphone(s). This goal can be achieved by two methods; namely, increased microphone sensitivity or increased number of microphones. In the case of resonant optoacoustic detection, there is a limit to the amount of energy which can be usefully removed.

More sensitive microphones tend to have larger diaphragms which extract more energy because of the larger area. However, the noise pickup also increases. Employing several less

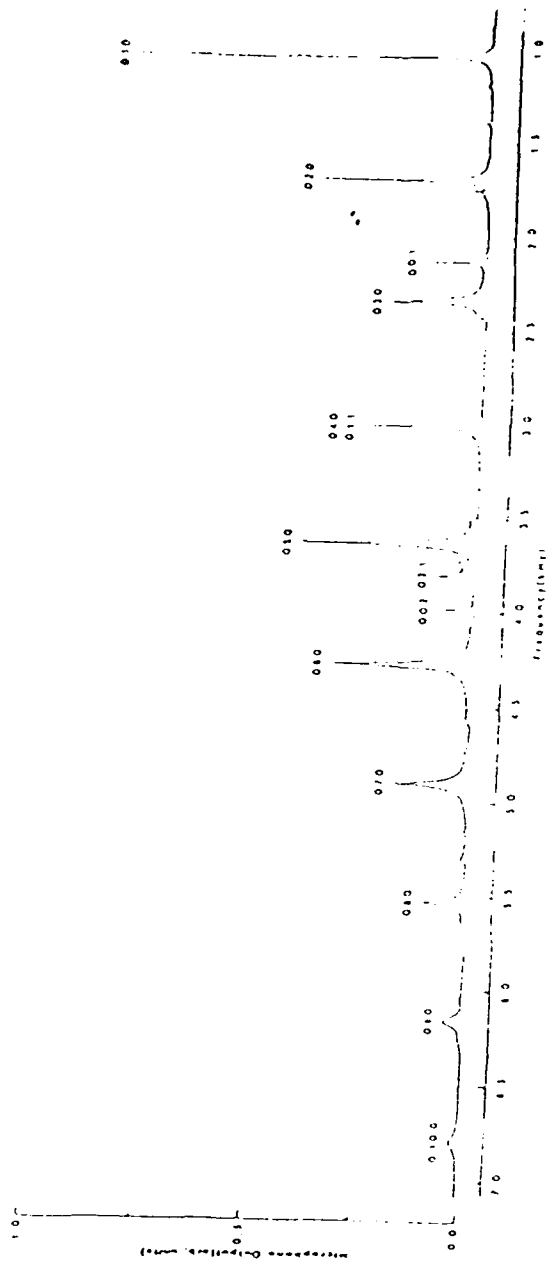

Figure 4-6. Acoustic resonant mode structure measured with excitation along the wall opposite to the microphone. The cell and experimental conditions are identical to Figure 4-5. The vertical scale is also the same as in Figure 4-5.

sensitive microphones can produce total signal levels equivalent to the more sensitive microphone while reducing the noise by the square root of the number of microphones. Working with a small diameter cell, less pressure wave scattering is expected with the smaller area microphones because they better approximate the arc of the cell wall.

A prototype cell was tested by monitoring Q as 1 to 4 microphones were embedded into the cell walls. The results of measuring Q as a function of the number of microphones is plotted in Figure 4-7. Each microphone introduces a loss of ~9% in Q. Optimum energy extraction at $Q_O/2$ corresponds to five microphones.

Q has also been measured using the apparatus described in Section 4.3.2 for a cell containing four microphones. The cell was charged with one atmosphere of Argon containing 9 ppm NO or one atmosphere of Xenon containing 1 ppm NO. The measured Q's were 410±40 and 790±80 respectively.

For a monatomic buffer gas, a plot such as Figure 4-7 can be extrapolated to zero microphones to yield Q_O. Q_O can be compared with the Q calculated from Equations (13) and (14). The difference between Q_O and Q represents the signal lost due to surface scattering when the cell has no microphones. A measurement of Q=410 for 4 microphones and a pressure of 1 atmosphere Argon extrapolates to Q_O=685. The calculated Q for Argon is 704. This implies that there is a 3% scattering loss. With Xenon/NO, Q_O is 1320 while the calculated Q is 1360. This also represents a 3% scattering loss.

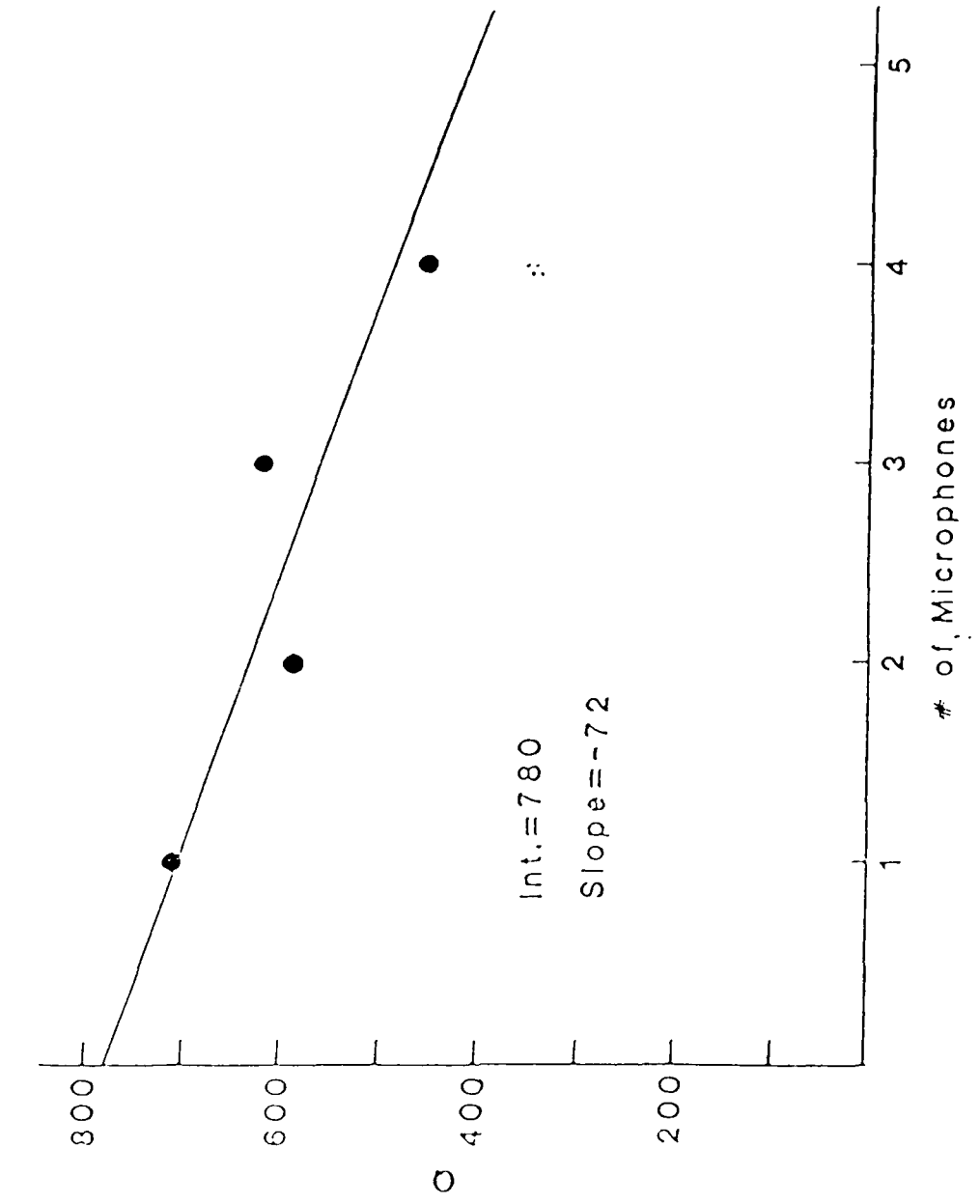

Figure 4-7. A plot of the acoustic gain factor Q versus number of microphones added to the cell. Optimum energy extraction occurs when one-half the energy is removed from the standing wave. For Q_o=Intercept the optimum extraction point $Q=Q_o/2$ in this plot falls near five microphones.

4.3.2 Gas Composition and Noise Sources

Figure 4-8 depicts the apparatus used to examine the remaining six items listed in Table 4-2. The laser used for these experiments is a continuous wave CO laser constructed to minimize both intensity and frequency fluctuations of the output beam. The laser is line tunable from 5.1 to 6.1μm (P(13)), v=9-→8). The maximum output power of this line is 1.5W. A pair of 15 cm focal length lenses, collimate the output beam. The chopper wheel located near the focus between the two lenses is positioned to ensure complete blockage of the laser beam, since deviations from complete blockage reduce the signals from the optoacoustic cell. Two mirrors are used to direct the collimated laser beam to the cell and to provide steering capability for fine tuning the passage of the beam through the cell.

The optoacoustic cell employed was a Plexiglas chamber 6.35 cm id. and 6.35 cm. long (cylinder length) with four microphones mounted at 0°, 90°, 180° and 270° halfway (3.17 cm) along the cell axis. The cell dimensions and microphone mounting positions were chosen based on the experiments described in Section 4.3.1. Compressed closed-cell foam holds the detector centered within a vacuum chamber. The vacuum jacket is wrapped with grounded carbon cloth which provides an electrical shield. The two chambers and the carbon cloth are located within the poles of a pair of Helmholtz coils capable of producing dc fields up to 1.3 kgauss which are slowly sweepable. The output from the microphones is fed into the same signal processing system as the one described in Section 4.3.1.

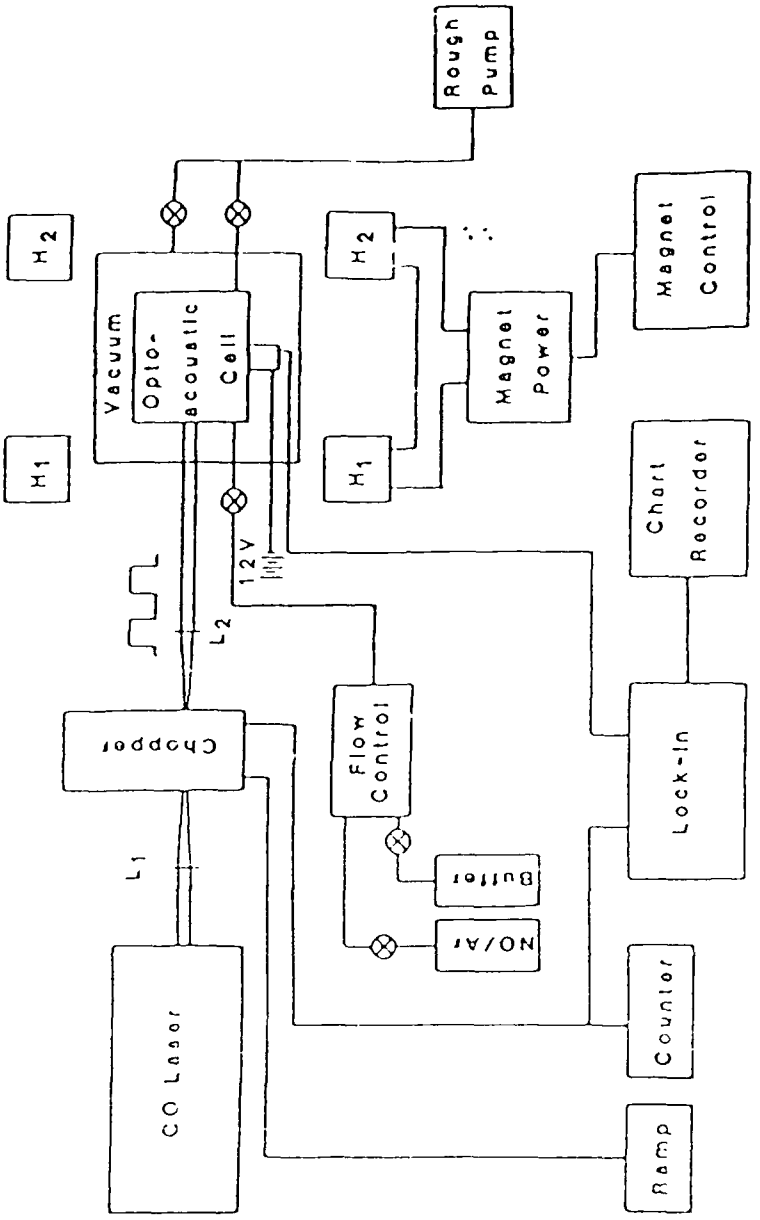

Figure 4-8. A schematic diagram of the apparatus used to measure various gas composition and noise sources. The laser is a cw CO laser operating at 5.307 m. The chopper, microphone and signal processing electronics are the same as in Figure 1-4. The optoacoustic cell is a plexiglas cylinder 6.35cm long and 6.35cm i.d. It is surrounded by a vacuum jacket for acoustic isolation purposes. The vacuum jacked is mounted inside a pair of Helmholtz coils, H_1 and H_2, which are energized by a power supply capable of producing 1.3 kgauss magnetic fields within the coils. The power supply is capable of slowly varying the magnetic field from 0-1.3 kgauss.

4.3.2.1 Total Gas Pressure

The total pressure is a major contribution to the collisional transfer of energy from the NO vibrational motion into translational motion of the buffer gas and the determination of the pressure wave amplitude via Q_{sur}. Minor contributions appear as small frequency shifts with pressure and in Q_{SK}.

Collisional changes cease to exist at Argon pressures exceeding approximately 200 torr. Similar predictions for Xenon are unavailable since the NO-Xenon relaxation rate is not known. Thus, the signal dependence versus total pressure at pressure greater than 200 torr is governed by the Q of the cell which is dominated by Q_{sur}. Combining Equation (14) and the fact that ρ_0 P_0 leads us to conclude that there is a $(P_0/\omega)^{1/2}$ dependence on the signal.

Figure 4-9 summarizes the experimental results. For these experiments, 20 torr of a 10^{-3} NO/Argon mixture was admitted to the cell, and Argon added until a total pressure between 20 torr and 700 torr was achieved. Pressures between 120 torr $(P_0/\omega)^{1/2}$ = 0.14 and 700 torr $(P_0/\omega)^{1/2}$=0.335 display the expected square root dependence. At pressures less than 120 torr, an elbow occurs as incomplete collisional relaxation effects appear. Comparison of the observed slope with a calculated slope is not possible due to the presence of other factors (see Equation (12)).

4.3.2.2. NO Partial Pressure

Use of Equations (6) and (12) allows prediction of a linear relationship between the signal (mode amplitude) and the quantity of NO (via heat production) present in the system. We

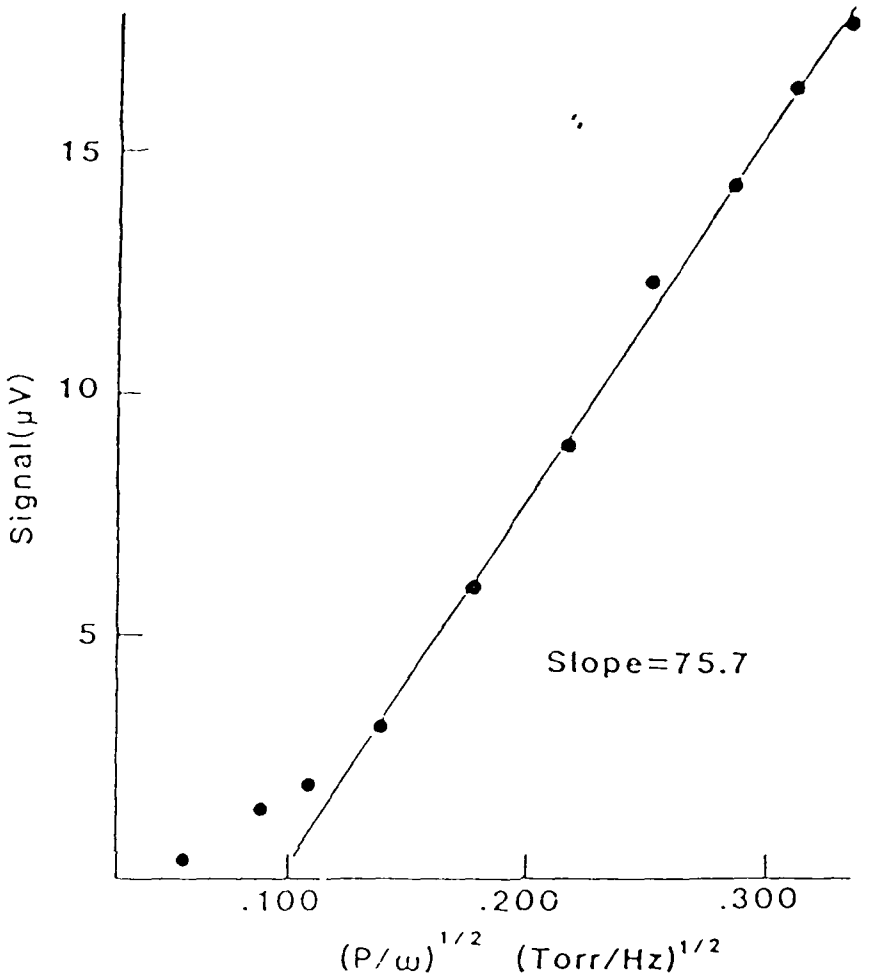

Figure 4.9 A plot of microphone signal versus total pressure using Ar as the buffer gas. 20 torr of a 10^{-3} NO/Ar mixture is admitted to the cell and Ar added to bring the total pressure to 20-700 torr. The elbow near .13 (~120 torr) arises from incomplete energy transfer as is explained in the text. Eqn 12 predicts a linear dependence of signal on the ratio $(P/\omega)^{1/2}$. Such a dependence is clearly observed at higher pressures.

have found this relationship to be valid for NO/Argon mixtures ranging from 1000 to 0.1 ppm NO. The lower limit occurs in the ppb range when the signal cannot be differentiated from the background noise in the test cell. At 1.4 ppm NO, 1 μvolt of signal is measured at a total pressure of 700 torr and a laser power of 600 mW.

Based on the 1 μvolt measured signal at 1.4 ppm and a linear extrapolation of signal with NO concentration, we predict a signal strength of one picovolt at 1.4 ppt NO. Presently, such a signal is undetectable. However, multipass optics should provide at least a signal increase of 10-20 times. Experiments indicate a signal increase of 40 times when Xenon replaces Argon as the buffer gas. Therefore, in an optimized multipass system we expect signals around 100-300 pV from 1 ppt NO/Xenon. This signal should be detectable with an optimized, low noise system. Thus, the anticipated detection limit of 1 ppt appears reasonable.

In our most recent and most sensitive experiments to date we have observed ~100 nV of signal from 5 ppb of NO in 700 torr of Xenon in a single pass system. The extrapolated signal based on this measurement of 20 pV at 1 ppt NO/Xe again agrees with the previous signal level expectations.

4.3.2.3 Buffer Gas

The initial choice of buffer gas was dictated by three constraints; namely the buffer gas must convert the maximum percentage of NO vibrational energy into translational motion, it must be non-absorbing and it must be readily available, relatively inexpensive, and non-toxic. Monatomic noble gases

fulfill some or all of these constraints. Helium is an extremely inefficient collisional partner and has a very large sound velocity. Xenon is the most efficient collision partner but is more expensive than Argon. On the basis of cost and performance, Argon appears to be the buffer gas of choice at the present time and has been used primarily in our present experiments. A search has started for a polyatomic collisional relaxer to increase the overall efficiency of the NO-Argon energy transfer. To date, a suitable candidate has not been found.

A series of experiments was performed to test the efficiency of Xenon as a collision partner. These results are given in Figure 4-10. In this series of experiments, 1.1 torr of a 10^{-3} NO/Argon mixture is introduced into the cell and Xenon added to bring the total pressure up to its measured value. This plot exhibits a shoulder at approximately 300 torr. We expect the shoulder to appear at pressures below the 120 torr limit for Argon. As yet we cannot explain the Xenon result. Note that ~3 times the signal amplitude is produced at 700 torr by approximately 1/13 the quantity of NO compared with NO/Argon at 700 torr (Figure 4-9).

4.3.2.4 Magnetic Field

The presence of an unpaired electron in the NO molecule accounts for the shift in energy (wavelength) when an external magnetic field is applied. The strength of the magnetic field determines the magnitude of the wavelength shift (Zeeman shift). Thus, sufficient displacement must exist between a CO laser line and an NO absorption line, to allow significant shift of the absorption line compared to its width by increasing the magnetic field strength. For our purposes, there must be sufficient

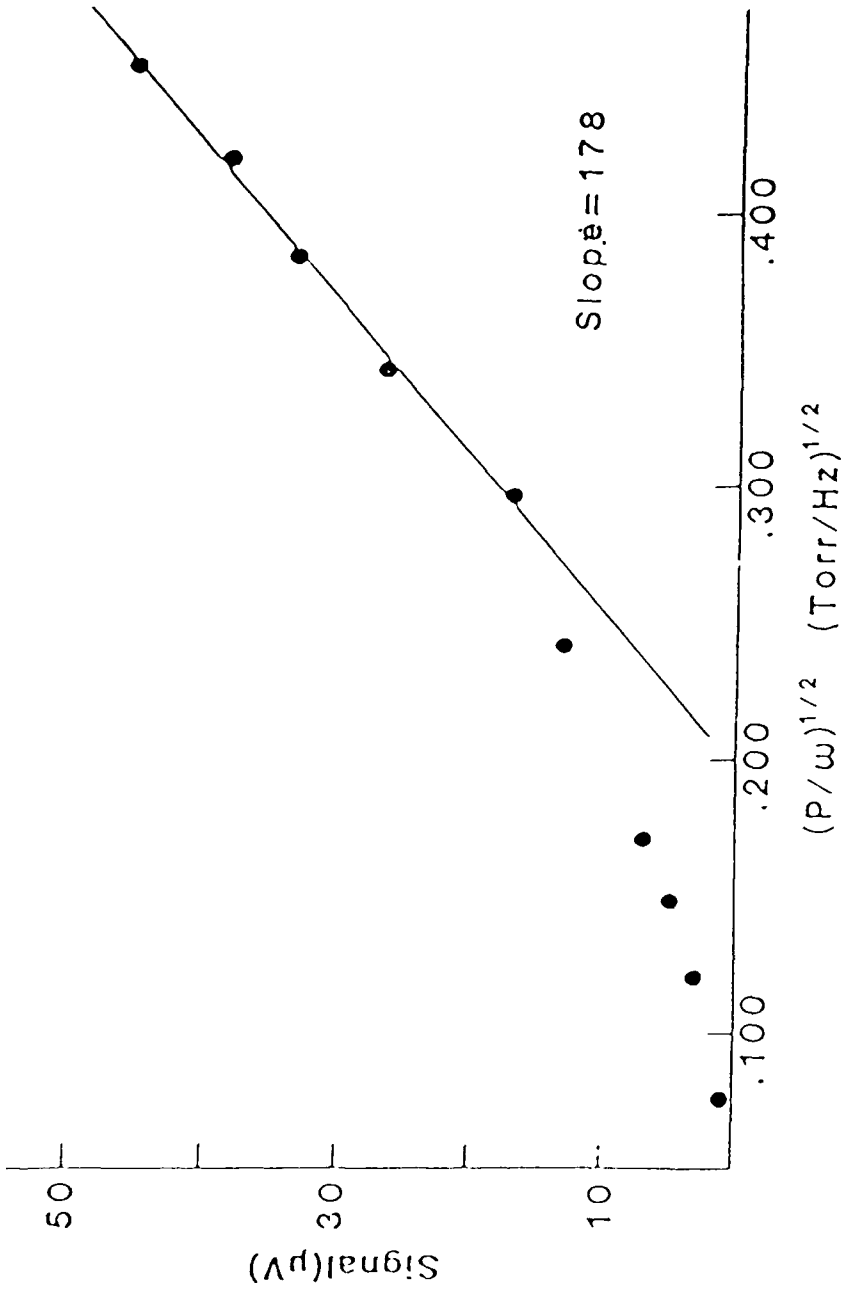

Figure 4-10. A plot of microphone signal versus total pressure when Xe is used as a buffer gas. 1.5 torr of a 10^{-3} NO/AR mixture is admitted to the cell and Xe added to bring the total pressure into the 20-700 torr range. The elbow occurs near .30 (∿300 torr). We do not understand why the elbow occurs at such high pressure in this instance. The expected $(P/\omega)^{1/2}$ dependence is again seen at the highest pressures. Note that at 700 torr nearly 3 times the signal is seen for 1/13 the amount of NO present when Xenon replaces Argon as the buffer gas (see Figure 4-9 for the Ar results).

magnetic field strength to shift the NO line into resonance with the CO laser line.

For the CO laser line P(13), 9→8 and the NO $^2\pi_{3/2}$ (1<-- 0) R(3/2) absorption line, the spacing is sufficient at pressures below ~50 torr to map two Zeeman line profiles for magnetic fields less than 1.3 kgauss. Figure 4-11 depicts the results of sweeping the magnetic field from 0 to ~1.3 kgauss with 20 torr of a 10^{-3} NO/Argon mixture in the cell. At a maximum field strength of 1.3 kgauss, two of the NO Zeeman components shift through the CO laser line. These two Zeeman transitions are the M_J = 1/2 <-- 3/2 line at ~ 620 gauss and the M_J = -1/2 <--1/2 line at 1.14 kgauss. These ΔMJ = ± 1 transitions are spectroscopically allowed for light polarized perpendicular to the magnetic field. Other possible M_J transitions for this NO-CO line pair are listed, along with their absorption strengths and field strengths, as determined by Kaldor et al. (4.18).

For pressures exceeding approximately 300 torr Argon, the NO line has broadened to the point that no magnetic field dependence can be seen at field strengths less than 1.3 kgauss. This result agrees with the pressure broadening parameter for NO/Argon, ΓAr ~0.065 $cm^{-1}atm^{-1}$, which leads to prediction of a line width of 0.025 cm^{-1} at 300 torr. The Zeeman tuning rate of the R(3/2) NO line is ~2.5 x 10^{-3} cm^{-1} $kgauss^{-1}$. Using the line width and tuning rate values, we deduce that a 10 kgauss field should enable us to Zeeman shift from the absorption maximum to almost zero absorption.

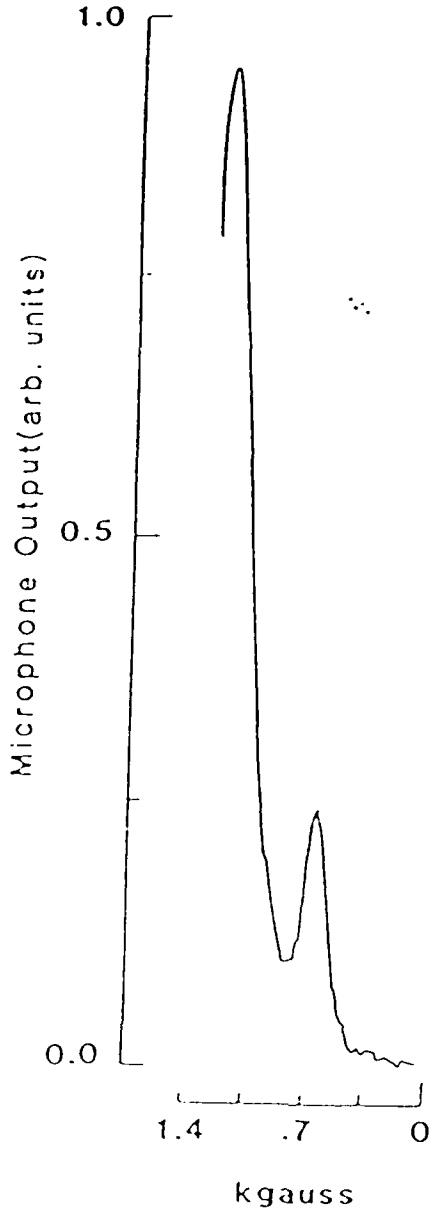

Figure 4-11. The magnetic field dependece of the NO $^2\Pi 3/2$, 1 <--0, R(3/2) transition. In this experiment the magnetic field is swept from 0-1.3 kgauss with 20 torr of a 10^{-3} NO/Ar mixture in the cell. The peak near 620 gauss corresponds to the M_J=-1/2 <---M_J=3/2 Zeeman component while the peak near 1.1 kgauss corresponds to the M_J=-1/2 <--- M_J=1/2 Zeeman transition. Both transitions are allowed when the laser beam is polarized perpendicular to the magnetic field.

4.3.2.5 Acoustic Isolation

The prediction that 1 ppt NO in an atmosphere of Xenon produces ~200 pV of signal sets the acoustic isolation requirement at less than 20 nV broadband noise within the pass-band of our lock-in amplifier. However, we note from our present preliminary set-up for testing feasibility that acoustic noise voltage in the 50 μV range occur (0 to 50 kHz). Low frequency floor vibrations appear to dominate as our noise source (< 150 Hz). The large low frequency content means that only a small percentage of this noise should appear at kilohertz detection frequencies. Improved vibration isolation and reduced mechanical coupling between the optoacoustic cell and the walls of the vacuum jacket can be expected to reduce acoustic noise by at least two orders of magnitude.

4.3.2.6 Electromagnetic Field Isolation

Electromagnetic pickup must also be less than 20nV since the total noise from all sources (e.g. acoustic, electromagnetic, etc.) must be less than this value. In the present test apparatus (Figure 4-8), the total e/m noise is approximately 100 μV (0 to 50 KHz). Only a minimum amount of shielding and e/m filtering has been used. A two order of magnitude reduction in e/m noise can be accomplished by using triply shielded signal leads and 1 Hz low pass filters on the microphone power leads.

The expected reduction in both acoustic and e/m noise should be sufficient to reduce the noise pickup from the room to less than the 20 nV level required. The present total noise level of 150 μV reduces to 200 nV of noise within the 600 Hz band-pass we presently use. A reduction of the experimental band-pass to 6 Hz will decrease this value to 20 nV. A two

orders-of-magnitude reduction in noise and a two orders-of-magnitude reduction in bandwidth should reduce the incoherent noise level to approximately 1 nV.

4.4 Conclusions

The influence of and interaction between components of an optoacoustic detection system for ultimately detecting explosives at the 1 ppt level have been examined from the theoretical and experimental system design aspect and feasibility experiments carried out. Particular attention has been paid to examining the behavior of the parameters that influence either signal or noise levels. Theoretical predictions relating signal levels to various parameters exhibit good agreement with experimental results. We conclude that 1 ppt detection of NO is achievable using only modest and straightforward extrapolation of the present experimental results.

Nitric oxide, the gaseous component to be detected, should be isolated in a buffer gas in a cell that takes advantage of signal gains derived from multiple pass optics and optoacoustic resonances. The detection system relies on careful acoustic and electromagnetic isolation (incoherent noise sources), and the ability to shift coherent noise sources away from the detection frequency. Double modulation, by a mechanically chopped laser beam and a Zeeman modulated NO absorption, provides the mechanism to accomplish such a shift.

Investigation of the individual parameters that influence signal and/or noise levels place design limits or restrictions on the components used for the measurements and detection. A cylindrical cell needs a radius between 2.5 and 3.7 cm (5.0 and

7.4 cm diameter) and the length of the cell should be equal to twice the radius. Additional machining of commercial plastics (e.g. Plexiglas, etc.) to produce ultra smooth inner walls is not necessary.

The largest signals arise at a frequency set by the lowest order radial-only acoustic resonance when on-axis excitation is used. Maximum signal extraction occurs when half of the energy in the acoustic standing wave is extracted by the microphone(s). With the Knowles CA-1832 microphones used in our experiments, this $Q_0/2$ point is attained with 5 microphones.

Monatomic buffer gases are required and Xenon appears to represent the best collision partner for NO, supplying 40 times more signal than Argon. Signal enhancement using Argon/Xenon mixtures or other collisional relaxers for Argon needs further investigation. The dependence of signal on total pressure requires cell operation at or above atmospheric pressure. Collisional line broadening by the buffer gas at such pressures complicates the Zeeman modulation.

Further investigations would be necessary to isolate and eliminate/minimize both coherent and incoherent noise sources including acoustic and electromagnetic noise sources. Filtering and band-pass restrictions appear able to help achieve the low noise levels that are necessary for successful detection of the signal levels present at 1 ppt.

AD-A193 633 DEVELOPMENT AND EVALUATION OF CHEMICAL DIAGNOSTIC METHODS(U) GEO-CENTERS INC NEWTON CENTRE MA L ISSACSON MAY 88 GC-TR-88-1429 N00014-84-C-2011 2/2

UNCLASSIFIED F/G 7/2 NL

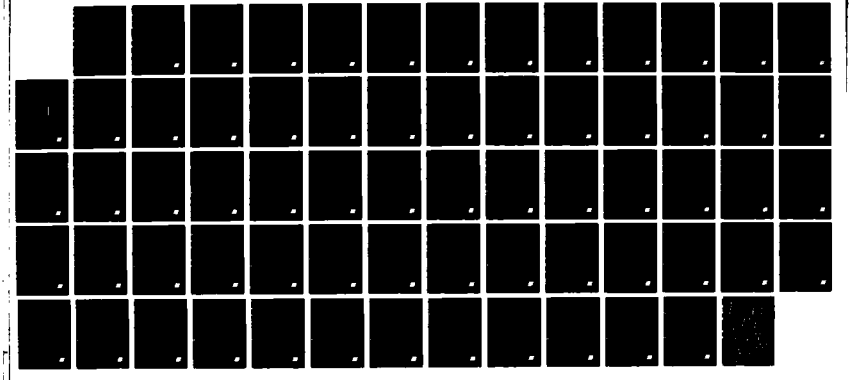

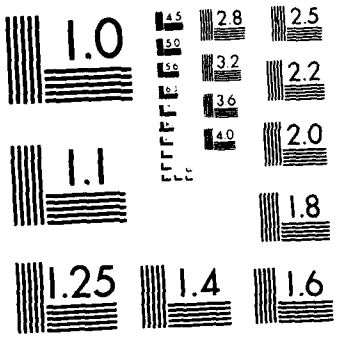
1.0
1.1
1.25
1.4
1.6
1.8
2.0
2.2
2.5
2.8
3.2
3.6
4.0
4.5
5.0
5.6
6.3

4.5 References

4.1 "Proceedings of the New Concepts Symposium and Workshop on Detection and Identification of Explosives Held at Reston, Virginia on October 30, 31, and November 1, 1978," Aerospace Corp., Washington, DC, sponsored by the U.S. Departments of Treasury, Energy, Justice and Transportation.

4.2 J. Hobbs, "Explosive Vapor Detection Summary", FAA Aviation Security R&D Workshop, April 18-19, 1983, U.S. Dept. of Transportation, Transportation Systems Center, Cambridge, MA 02142.

4.3 F.H. Jarke, S.M. Gordon, "Explosives Vapors Characterization", Report No. DOT/FAA/CT-82/65, IIT Research Institute, Chicago, Illinois, 1982.

4.4 D.L. Hartley and R.A. Hall, J. Appl. Phys. 43 (1972) 4134.

4.5 J.U. White, J. Opt. Soc. Am. 32 (1942) 285.

4.6 J.U. White, J. Opt. Soc. Am. 41 (1951) 732.

4.7 J.U. White, N.L. Alpert, and A.G. DeBell, J. Opt. Soc. Am. 45 (1955) 154.

4.8 H.J. Bernstein and G. Herzberg, J. Chem. Phys. 16 (1948) 30.

4.9 H.O. Kneser, H.J. Bauer, and H. Kosche, J. Acoustic. Soc. Am. 41 (1967) 1029.

4.10 P.M. Morse and K.V. Ingard, "Theoretical Acoustics", (McGraw-Hill, New York 1968).

4.11 M. Abramowitz and I.A. Stegun, "Handbook of Mathematical Functions", NBS Applied Mathematics Series 55, 1964.

4.12 R.H. Johnson, R. Gerlach, L.J. Thomas III, and N.M. Amer, Appl. Opt. 21 (1982) 81.

4.13 A. Karbach, J. Roper, and P. Hess, Chem. Phy. 82 (1983) 427.

4.14 R.D. Kamm, J. Appl. Phys. 47 (1976) 3550.

4.15 J.O. Hirschfelder, C.F. Curtiss, and R.B. Bird, "Molecular Theory of Gases and Liquids", (Wiley, New York, 1954).

4.16 L.B. Kreuzer in "Optoacoustic Spectroscopy and Detection," Y.H. Pao ed., (Academic Press, New York, 1977).

4.17 H.V. Malmstadt, C.G. Enke, S.R. Crouch, and G. Horlik, "Optimization of Electronic Measurements" Module 4, (W.A. Benjamin, Inc., Menlo Park, California, 1974).

4.18 A. Kaldor, W.B. Olson, and A.G. Maki, Science 176 (1972) 508.

4.19 B.P. Lathi, "Signals, Systems, and Communications", (John Wiley and Sons, New York, 1965).

4.20 L.L. Abels and J.H. Shaw, J. Mol. Spec. 20 (1966) 11.

4.21 J.I. Steinfeld, "Molecules and Radiation", (Harper and Row, New York, 1974).

4.22 D.A. McQuarrie, "Statistical Thermodynamics" (Harper and Row, New York, 1973).

4.23 G.D.T. Tejwani, B.M. Golden, and E.S. Yeung, J. Chem. Phys. 65 (1976) 5110.

5.0 DETECTION OF WATER VAPOR IN AIR USING A SURFACE ACOUSTIC WAVE SENSOR

5.1 Background

5.1.1 Problem Definition

The U.S. Navy has many situations in which it is essential to know the humidity level. In particular, the 4500 psi (i.e. 300 atm.) compressed air stored in flasks of submarines must be maintained at a dew point below -65°F in order to prevent moisture condensation and freeze up when ballast tanks are discharged under emergency conditions. Based on tables published by Laudsbaum, Dodds, and Stutzman (Figure 5.1) it is apparent that air at a pressure of 300 atmospheres and a dew point of -65°F will contain about 5×10^{-7} pounds of water per pound of air. A gram of air under these same conditions will therefore contain 5×10^{-7} grams of water. If this 1 gram sample of air is slowly expanded so that its pressure is 1 atmosphere, then it will occupy a volume of about 850 cm^3 at a temperature of 25°C. Thus, air with a dew point of -65°F at 300 atmospheres of pressure will contain a water vapor concentration of approximately 6×10^{-7} grams per liter of air at 1 atmosphere of pressure (i.e. ~0.6µg/L). Air at 1 atmosphere pressure with ~0.6µg/L of water vapor has a dew point below -110°F.

There are several sensor technologies that are able to detect water vapor at this concentration level. One method relies on the trapping and subsequent electrolysis of the water vapor. Another relies on the adsorption of water vapor onto a thin film of aluminum oxide whose capacitance is perturbed by the presence of the water vapor. Both methods are capable of

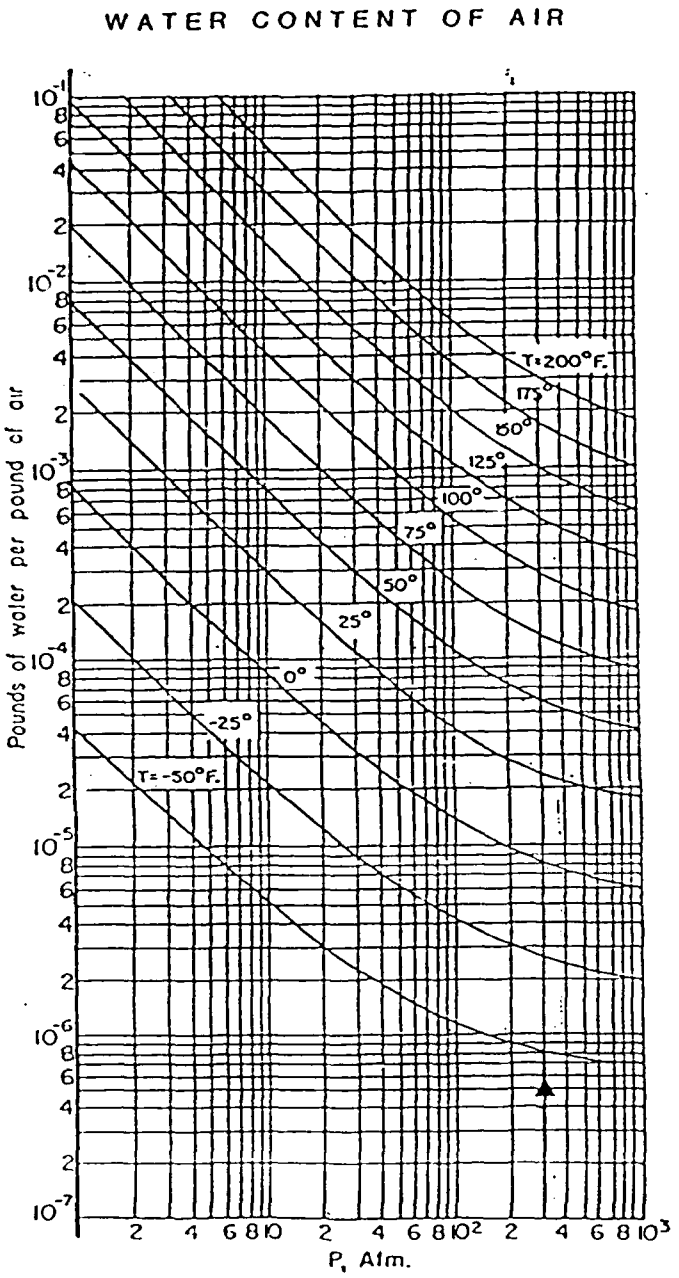

FIGURE 5.1

GEO-CENTERS, INC.

measuring water at these concentrations but their response times are rather slow. The aluminum oxide device reportedly takes as much as 30 minutes to respond at such low concentration levels and experiences problems with zero drift over time. Furthermore, no humidity sensor technology is available that can operate inside the high pressure air storage system.

A new vapor sensor technology based on Surface Acoustic Wave (SAW) devices may offer the sensitivity, ruggedness, and small size required to meet the Navy's need for dew point measurement applications. The objective of this task was to adapt existing SAW vapor sensor technology to detect water vapor at low concentrations.

5.1.2 Performance Goals

The objective of this program was to develop a simple instrument using a SAW vapor sensor that could detect water vapor concentrations of less than ~0.6µg/L at ambient pressure and temperature conditions. This concentration of water vapor corresponds to that which would be observed in a sample taken from a 4500 psi air cylinder whose dew point was -65°F. It was intended that this instrument provide a 9600 Baud RS232C serial output signal that could be monitored and recorded by a personal computer such as an Apple MacIntosh or Apple IIe. It was desired that the response time of the instrument be rapid enough to permit a complete water analysis to be performed in less than 5 minutes.

5.2 SAW Vapor Sensor Operating Principles

The use of Surface Acoustic Wave (SAW) devices for chemical vapor detection was first reported in 1979. Thus, SAW vapor sensors are a very new concept. The following discussion intends to offer a brief review of the important features of SAW vapor sensors.

5.2.1 Physical Operating Mechanism

SAW devices are mechanically resonant structures whose resonance frequency is perturbed by the mass or elastic properties of a thin layer deposited onto the device surface. Rayleigh surface waves can be generated on a very small polished slab of a piezoelectric material (e.g. quartz) with an interdigital electrode array that is lithographically patterned on the surface at each end of the device. When the electrode is excited with a radio frequency voltage, a Rayleigh wave is generated that travels across the device surface until it is "received" by the electrode at the other end. The Rayleigh wave has most of its energy constrained to the surface of the device and thus interacts very strongly with any material that is in contact with the surface (e.g. a chemically absorbent coating). Changes in mass or mechanical modulus of the coating produce corresponding changes in the Rayleigh wave velocity. The most common configuration for a SAW vapor sensor is that of a delay line oscillator in which the RF voltage output of one electrode is amplified and fed into the other electrode. In this way the device resonates at a frequency determined by the Rayleigh wave velocity and the electrode spacing. If the mass of the chemically selective coating is altered, then changes occur in the wave velocity that can be measured as a shift in resonant frequency of the device.

The SAW vapor sensor is clearly quite similar to bulk wave piezoelectric quartz crystal sensor such as that originally described by King and subsequently investigated extensively by Guilbault, et al. Both devices respond to mass changes of coating deposited on the device surface. However, SAW devices possess several distinct advantages including substantially higher sensitivity (owing to the much greater device operating frequencies that are possible with SAW), smaller size, greater ease of coating, uniform surface mass sensitivity, and improved ruggedness. Practical SAW vapor sensors currently have active surface areas of a few square millimeters and resonance frequencies in the range of hundreds of MHz. Modern microlithographic techniques permit the fabrication of SAW devices having a total surface area significantly less than a square millimeter and resonant frequencies in the gigahertz range. Most of the SAW vapor sensors reported employ two delay line oscillators fabricated side by side on the same chip and the difference between the two oscillator frequencies is monitored. In this way, drift from ambient temperature and pressure changes can be accurately compensated. Direct comparisons of SAW and bulk wave quartz crystal vapor sensors have been conducted by Vetelino et al. who observed significantly larger signals using SAW devices. Other workers at the Naval Research Laboratory have reported on the mechanism of SAW vapor sensor response and model coating studies.

5.2.2 Sensitivity and Selectivity

A 158 MHz SAW device having an active area of $8mm^2$ is able to provide resonant frequency shift of about 365 Hz when perturbed by a surface mass change of 1 nanogram. This level of sensitivity is predicted theoretically and has been confirmed

experimentally by using Langmuir-Blodgett films as calibrated mass loadings on the device. The same device exhibits a typical frequency "noise" of less than .16 Hz RMS over a 1 second measurement interval (i.e. 1 part in 10^7). Thus, the 1 nanogram mass change will provide a signal-to-noise ratio of almost 23 to 1. For vapor sensing applications, the trick is to have the vapor of interest selectively adsorb onto the mass sensitive surface of the device. Chemically selective coatings are used to perform this critical operation.

The development of selective coatings for water vapor is proceeding steadily. Solubility has been found to be a very effective guiding principle in the design of sensitive and selective coatings. In this approach, the coating of the SAW device is used as a "solvent" for the vapor to be detected. Both organic and inorganic materials were investigated in this study as candidate coatings for the SAW humidity sensor.

5.3 System Configuration

5.3.1 Hardware

In normal operation, a SAW sensor provides a signal that is the difference frequency between the clean and coated oscillators. This signal is processed into a TTL compatible pulse train whose frequency is determined by a digital frequency counter that is located on a printed circuit card that is plugged into the system motherboard. The difference frequencies obtained from the SAW sensor are usually in the range of 100 to 800 kilohertz. Ambient air is drawn across the sensor with suction from a small air pump. An electric solenoid valve is used to control the air exposed to the sensors. This valve is controlled by the system microcomputer. It can select either air whose

humidity is to be determined or a reference stream obtained from ambient air that has been scrubbed in a vessel containing 13X molecular sieves to strip out moisture. By switching back and forth between these two sources of air, it is possible to rezero the sensor and obtain compensation for baseline drift. SAW sensor frequencies are monitored and processed by the system microcomputer. Data is reported to the user over a 9600 baud RS232C serial communications line.

The SAW water vapor sensor instrument is described schematically in Figure 5.2. The system consists of a 158 MHz dual delay line oscillator having one side coated with a selective film chosen for its ability to absorb water vapor. Numerous coatings were evaluated for their ability to detect water vapor and their performance will be described later.

In addition to the SAW device and its associated RF support electronics, the system also contains regulated DC power supplies to permit operation from 120 volt 60 Hz power sources, microcomputer controlled 24 bit binary frequency counters (16 MHz maximum frequency with a crystal controlled time base), an air pump to draw ambient air across the sensors, and Teflon solenoid valves with TTL drive electronics. The system communicates with the outside world by means of a 9600 baud serial RS232C communications line.

A brief description of the instrument subsystems is provided in the following section.

NAVY HUMIDITY MEASUREMENT SYSTEM

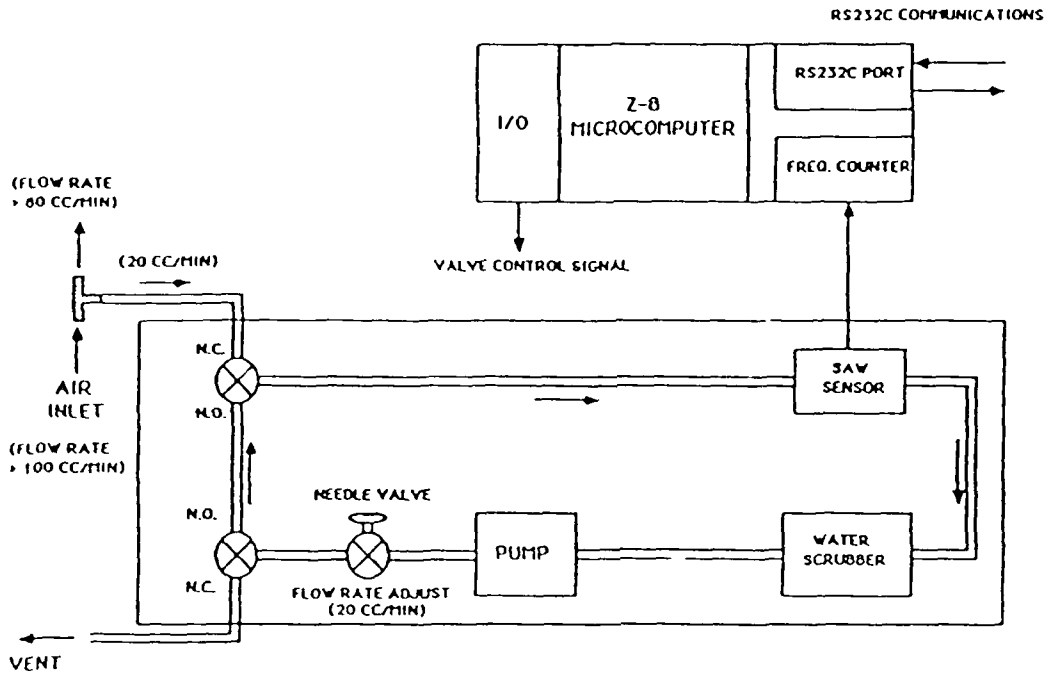

FIGURE 5.2

GEO-CENTERS, INC.

1) SAW Devices

The dual 158 MHz SAW device used in this system is shown schematically in Figure 5.3. ST-quartz is used as the substrate material in order to obtain low temperature drift. The SAW "chips" are attached to a conventional TO-8 header (Figure 5.4) where electrical connections to the chip are made via gold wire bonds. The side of the device nearest to the TO-8 tab is coated with the vapor sensitive coating. The other side is left uncoated.

2) RF Electronics

RF amplifiers are required by the SAW delay line oscillators to provide enough gain to overcome the insertion loss of the SAW devices. In addition, the output of these two, independent 158 MHz oscillators must be mixed to provide a signal equal to the difference between the two oscillators. This is accomplished in a mixer stage followed by a comparator to provide a TTL compatible output frequency. The schematic for the 158 MHz dual SAW sensor RF electronics in shown in Figure 5.5. A pictorial layout is provide in Figure 5.6.

3) Frequency Counter/Microcomputer

The frequency counter subsystem consists of 12 eight bit binary counters (3 counters per SAW sensor), a crystal controlled 1 second time base, and interface circuitry for the microcomputer. The frequency counter has an upper frequency limit of 16 MHz (limited by the 24 bit range of the counters). Resolution is 1 Hz and data is updated every 2 seconds.

The system microcomputer controls the sequencing of the measurement, the acquisition and processing of frequency data, the control of the solenoid valve, and the reporting of results over a 9600 baud RS232C serial communications line. The microcomputer subsystem is based on a Zilog Z8 along with 12K of static RAM. The application program is stored in EEPROM.

158 MHz DUAL SAW DEVICE

DIE SIZE	:	5 MM X 5 MM
WAVELENGTH	:	20 MICRONS
SUBSTRATE	:	ST - QUARTZ
ELECTRODES	:	ALUMINUM

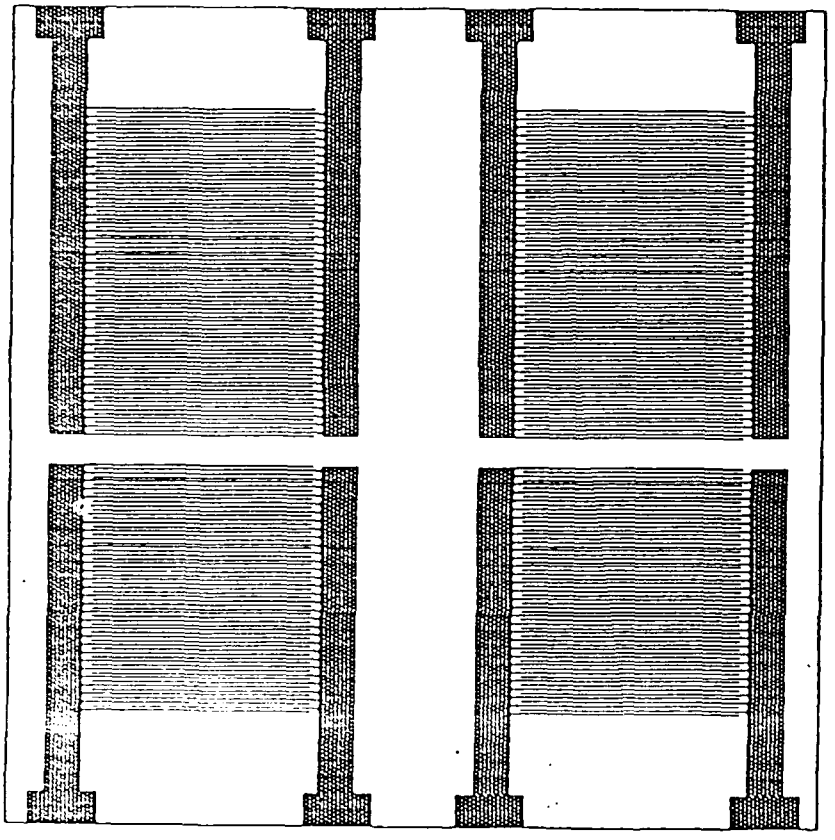

FIGURE 5.3

GEO-CENTERS, INC.

158 MHz DUAL SAW DEVICE
TO-8 Header / 0.600" Diameter
12 Pin Package

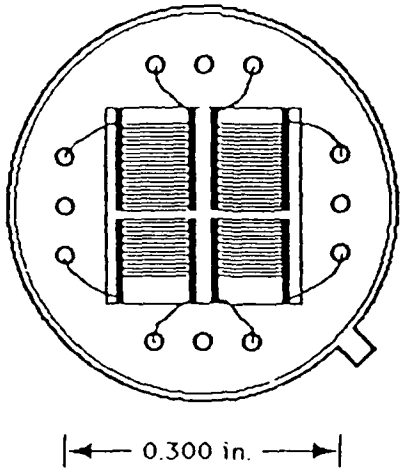

INTERNAL VOLUME OF PACKAGE ≈ 230 μL

FIGURE 5.4

GEO-CENTERS, INC.

158 MHz

DUAL SAW DELAY LINE OSCILLATOR (5 VOLT)

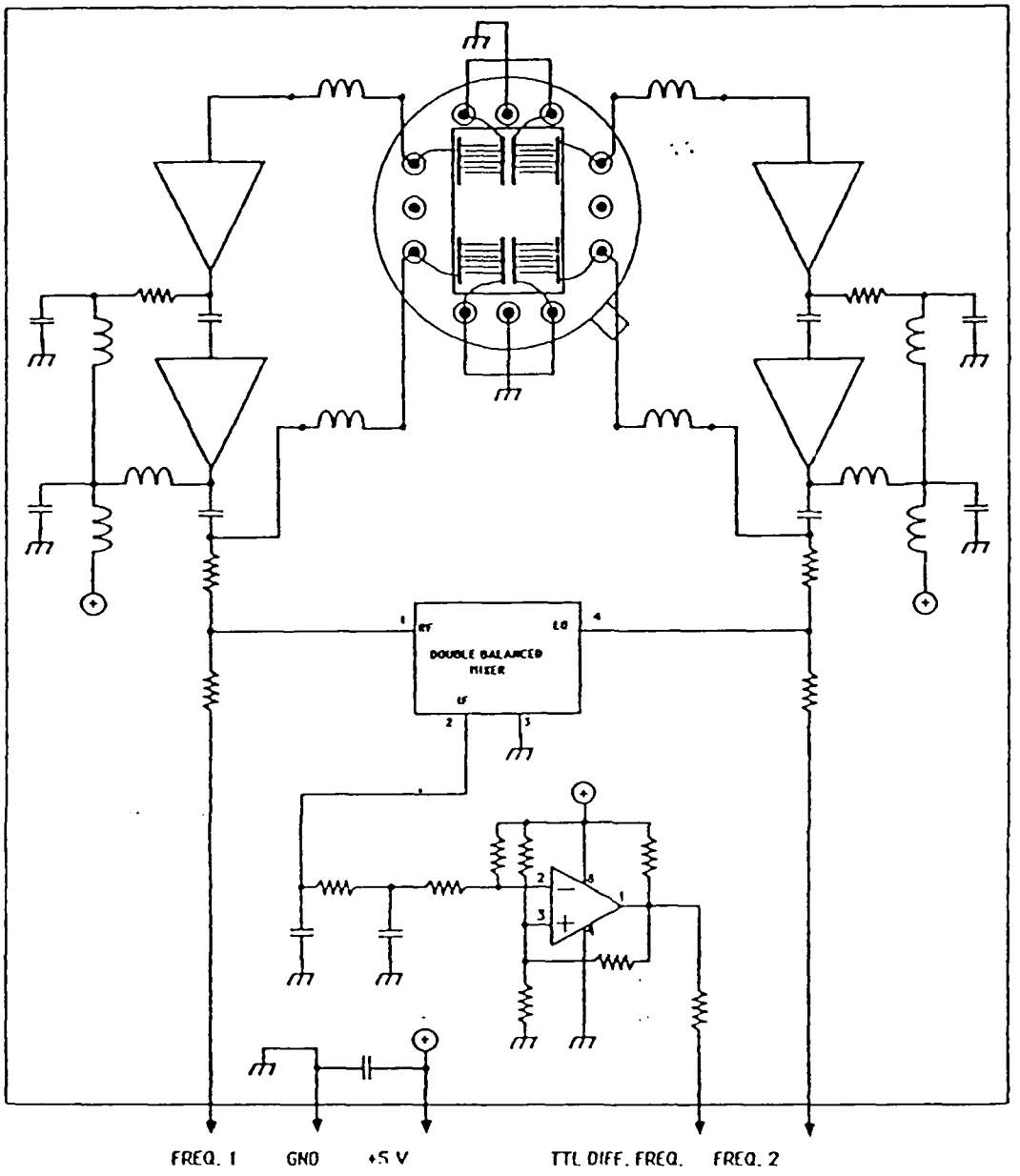

FIGURE 5.5

GEO-CENTERS, INC.

158 MHz DUAL SAW DELAY LINE OSCILLATOR
PICTORIAL DIAGRAM

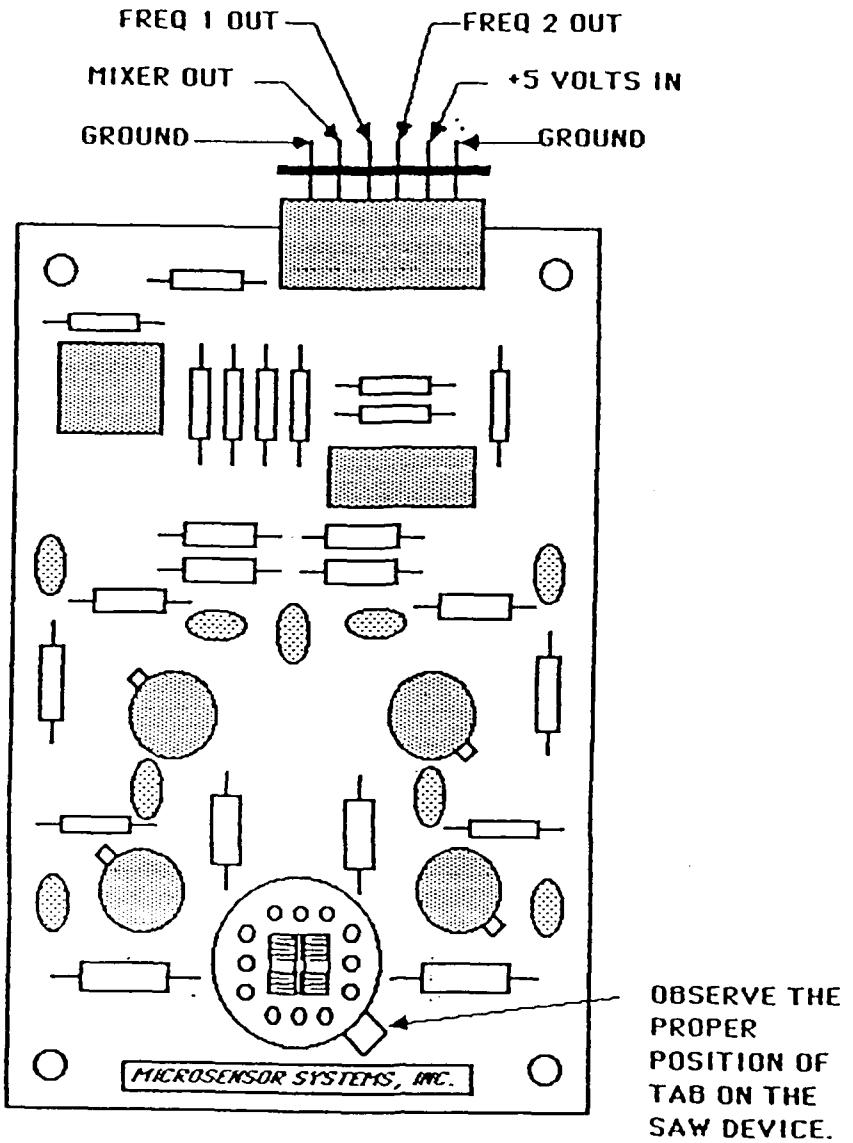

FIGURE 5.6

GEO-CENTERS, INC.

4) Power Supply

A compact linear power supply is used to convert 120V, 60Hz AC into regulated +5, +12, and -12 Volt power for the system.

5) Pneumatic System

The pneumatic system is illustrated most clearly in Figure 5.2. It consists of miniature 120 volt solenoid valves with Teflon seals, a miniature 12 volt diaphragm pump, stainless steel swagelok fittings and Teflon tubing. The SAW sensors are enclosed on gold TO-8 headers with nickel-plated lids that are modified with 1/16 inch stainless steel tubing. The lids are epoxied onto the TO-8 headers. Teflon tubing is used to interconnect the sensors with the pump, solenoid valves, and bulkhead vents and inlets.

The system requires an air scrubber to provide a source of dry reference air when the auto sample mode is used. This is obtained from a drying chamber containing about 100 cc of molecular sieves. The dryer is fabricated from a block of aluminum into which 4 holes are drilled. These 4 chambers are filled with 13X Molecular Sieves and sealed with an aluminum cover with a Teflon gasket. The chambers are connected to the rest of the system by means of teflon tubing and 1/4-28 plastic fittings.

5.3.2 System Software

1) Operating Modes -- Depending on the EEPROM that is installed into the microcontroller, the system can provide either a continuous report of the SAW sensor signal (i.e. "CONTINUOUS" mode) or it can automatically sample the air present at the sample inlet, record the SAW sensor responses and report the total signal measured during the experiment (i.e. "AUTOSAMPLE" mode).

Continuous Mode

In CONTINUOUS mode, operation of the instrument begins as soon as the power is turned on. Data are transmitted at 9600 baud on the RS232C line with 8 data bits, no parity, and 2 stop bits. Basically, the instrument monitors the frequency of the SAW sensor and transmits a 12 byte message every 2 seconds that reports the difference frequency (in Hertz) between the sample and reference oscillators of the SAW sensor. The message consists of four 24 bit binary numbers from the frequency counters with a carriage return/line feed delimiter every 3 bytes. The user must convert this message from 3 byte binary format into a decimal frequency value.

In CONTINUOUS mode, it is presumed that a flowing stream of air is being supplied to the SAMPLE INLET by some external system (such as a vapor generator). The flow rate provided to the instrument should be in the range of 10-200 cc/min. Periodic rezeroing of the SAW sensor can only be accomplished by externally switching a zero gas into the sample inlet.

Autosample Mode

The data transmitted in AUTOSAMPLE mode is intended to be printed out directly with no further processing required. The system has a 128 second measurement cycle during which the pump pulls air through the sensor array at about 20 cc/min. The air source to the array is selected by the solenoid valve from either the sample inlet or the molecular sieve dryer. Dry air is supplied to the array for 32 seconds followed by sample air for 64 seconds and dry air for 32 seconds. The dry air allows a "zero" reading for the sensors to be obtained. During this 128 second measurement cycle, a period (i.e. ".") is transmitted

every 2 seconds to indicate that the system is alive and well. At the end of the 128 second measurement cycle the system prints the change in SAW sensor frequency that occurred between the time that the array was exposed to scrubbed "zero" air and the time it was exposed to "contaminated" ambient air. This allows changes in sensor output to be more readily observed. The data is printed as a decimal value (in the range of +/- 1.6000 Hz) of the SAW frequency change with carriage return/line feed delimiter between the data for each sensor.

In AUTOSAMPLE mode, it is presumed that a flowing stream of air is being supplied to the SAMPLE INLET by some external system (such as a vapor generator). The flow rate provided to the instrument should be in the range of 100-200 cc/min. and must be maintained at ambient pressure. This is best accomplished by using a "TEE" fitting at the instrument sample inlet. The instrument will pull air in at about 20 cc/min. and the remaining flow from the water vapor source will be vented through the TEE to the ambient air. Pressurization of the sample inlet must be avoided since it will cause an abrupt flow rate change over the sensor when the solenoid valve is switched from dry air reference to sample air. Flow rate variations over the sensor can result in spurious readings.

It should be noted that the 13X molecular sieve used in the dryer requires replacement after about 100 hours of use.

2) Signal Processing Algorithm -- All sensor devices exhibit drift and most sensors must be kept reasonably clean if they are expected to reliably detect chemicals at low ambient concentrations. One very good way to compensate for sensor drift

and to keep the sensor clean is to frequently expose the sensor to the air stream to be measured followed by exposure to dry reference air. The difference between the sensor response to dry air and moist air can be recorded. Since the drift during this brief measurement cycle is sure to be small, its effects can be virtually eliminated. Furthermore, the sensor device spends a significant percentage of its time being flushed with clean, dry air. In this way, contaminants which may have collected on the device can be swept away.

This system can work on a 128 second measurement cycle during which the sensors are exposed to scrubbed reference air for 32 seconds, contaminated (perhaps) ambient air for 32 seconds, and scrubbed reference air for the final 64 seconds. The signal processing algorithm is illustrated graphically in Figure 5.7.

5.4 Sensor Response Data

5.4.1 Experimental Conditions

The primary objective of this study was to evaluate a number of promising coating materials for their water sensitivity when deposited onto a 158 MHz SAW device. The 158 MHz dual SAW devices were used because they are readily available (Microsensor Systems, Inc., part number SD-158-A). All coatings were deposited using a spray deposition technique. A dilute mixture (typically 0.2% by weight) of the desired coating material was prepared in a volatile solvent such as methanol or chloroform and sprayed through a fine nozzle and mask onto one side of the SAW device. Clean 20 psi air was used as a spray propellant. The coating materials were all commercially available organic

SAW SIGNAL PROCESSING ALGORITHM

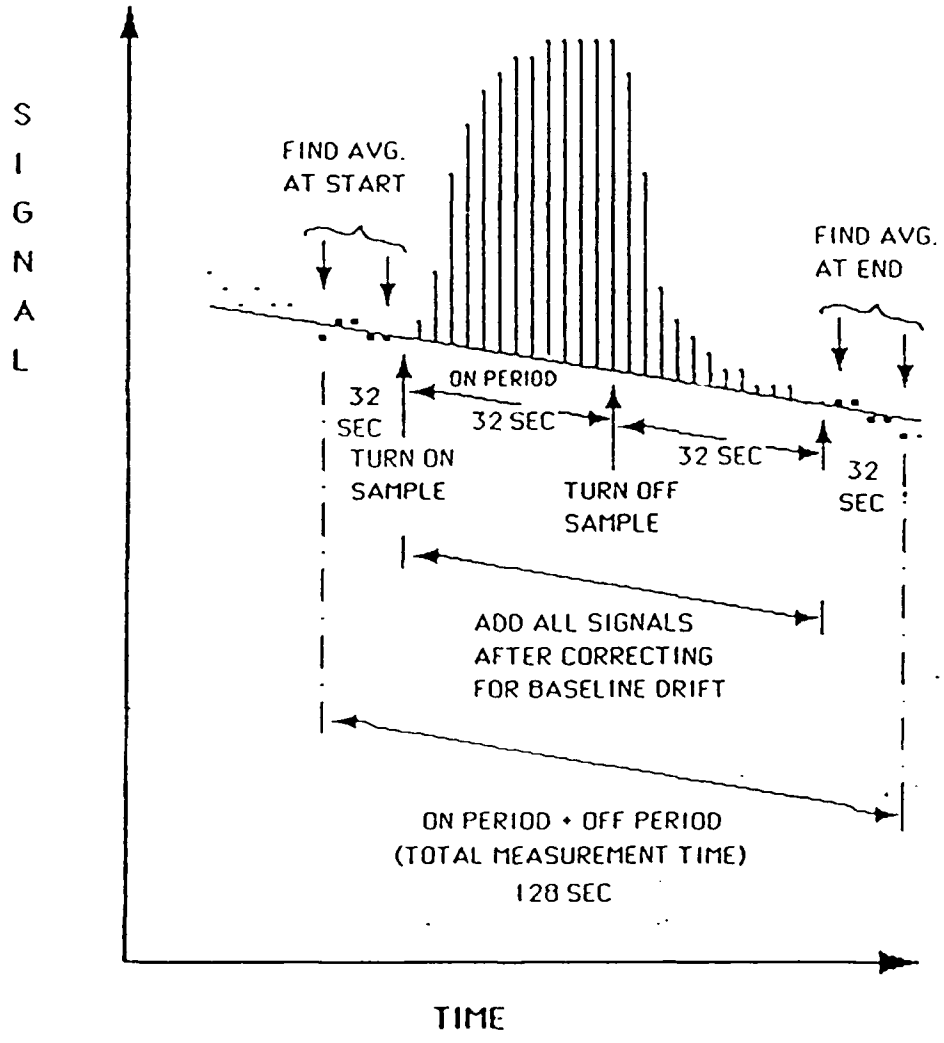

FIGURE 5.7

GEO-CENTERS, INC.

polymers except for a crystalline material called "Humisorb" whose composition is proprietary to Microsensor Systems, Inc. Film thicknesses were gauged by the SAW oscillator frequency shift (in KHz) that they produced during the spray deposition process. Actual film thicknesses can be inferred from the theoretical SAW mass sensitivity of the 158 MHz device (i.e. 365 Hz/nanogram), the active area of the device (i.e. 0.08 cm^2) and the density of the coating material. An attempt was made to coat all devices with films that produced a frequency shift of about 200 KHz. This was possible for all of the polymeric coatings but the Humisorb would damp the SAW oscillations before a frequency shift of 200 KHz could be obtained. As a result, the Humisorb coatings used in this study produced frequency shifts that were in the range of 50 KHz. Since the SAW vapor sensitivity is directly related to the effective coating thickness, all results have been normalized to assume a coating frequency shift of 250 KHz in an attempt to allow accurate comparison of the intrinsic performance of the coating materials. The devices included in this study and the coatings investigated are tabulated below.

DEVICE ID	COATING	THICKNESS (KHz)
B-064	Poly(ethyleneimine)	264
8647-01	Poly(styrene sulfonate)	192
B-062	Poly(vinyl pyrrolidone)	266
8726-07	HUMISORB	48
8726-02	Humisorb + Poly(styrene)	223
8708-02	Humisorb + Poly(styrene sulfonate)	234
8709-1	Humisorb + Poly(ethyleneimine)	232

Humisorb was found to be a very sensitive coating but its response saturated at water concentrations above 200 mg/m^3. Attempts were made to increase the amount of Humisorb that could be deposited and also increase the dynamic range of the sensor by

blending the highly sensitive Humisorb with less sensitive hygroscopic polymers.

Vapor calibration curves were obtained by exposing each SAW device alternately to dry air and then to humidified air using a two minute on/two minute off cycle programmed into a Microsensor Systems, Inc. model VG-7000 automatic vapor generation system. The VG-7000 supplied a flow rate of 100 cc/min. at ambient pressure. All SAW vapor sensors were maintained at room temperature (i.e. 25°C ± 2°C). The 9600 Baud serial data from the SAW vapor sensor instrument operating in continuous mode was received by an Apple MacIntosh for plotting and display.

In addition to obtaining water vapor calibration curves, several of the sensors were evaluated for their day-to-day and sensor-to-sensor repeatability.

5.4.2 Water Vapor Calibration Results

Water vapor concentrations in the range from 4 mg/m^3 (i.e. 4 µg/L) to as much as 4000 mg/m^3 (i.e. 4000 µg/L) were generated with the VG-7000 and exposed to the various SAW coatings while SAW oscillator frequency shifts were recorded. Response data were then normalized to compensate for variations in the applied coating thickness. Each data point on the calibration curves represents the average SAW signal obtained from 4 consecutive 2 minute on/off vapor exposures. The vapor calibration data for each of the coatings studied are presented in Figures 5.8-5.14. Figures 5.15, 5.16, and 5.17 illustrate the repeatability of response that is typically available from

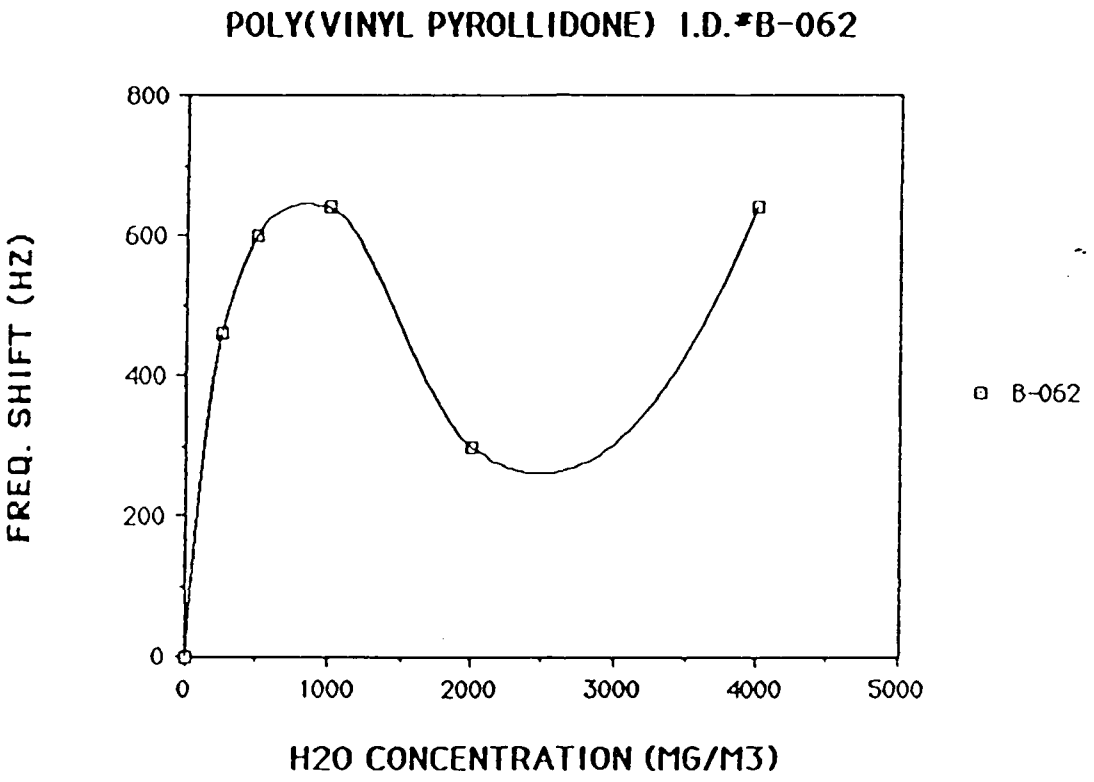

FIGURE 5.8

GEO-CENTERS, INC.

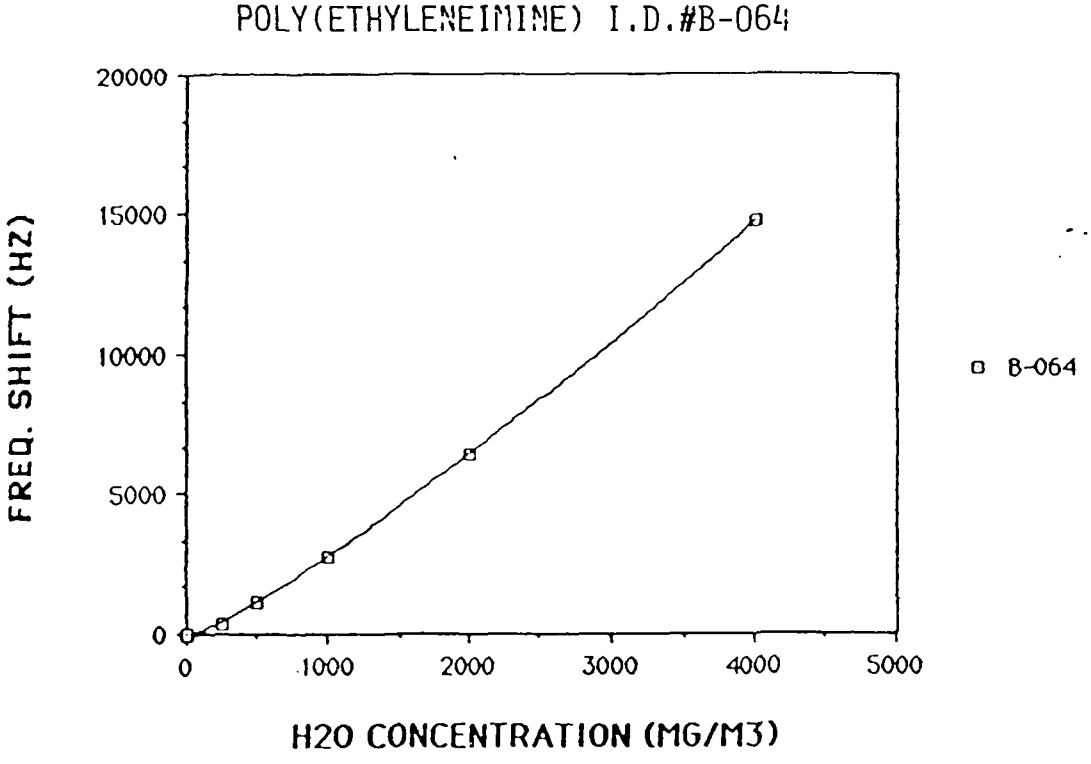

FIGURE 5.9

GEO-CENTERS, INC.

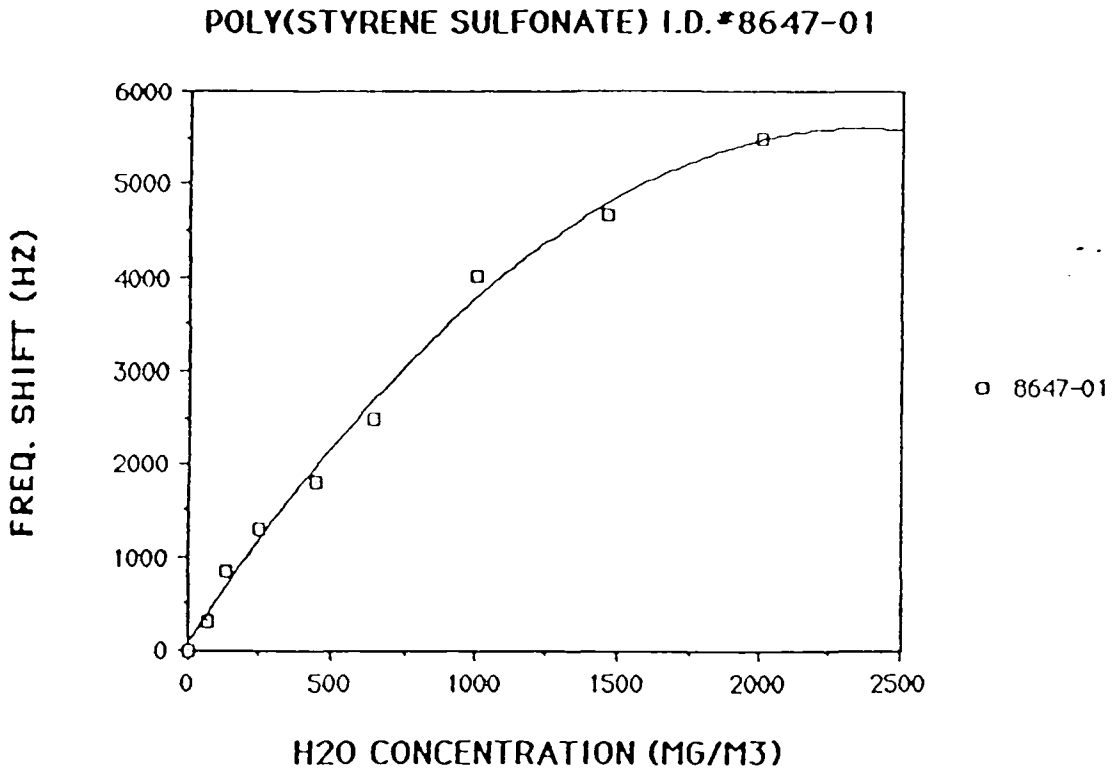

FIGURE 5.10

GEO-CENTERS, INC.

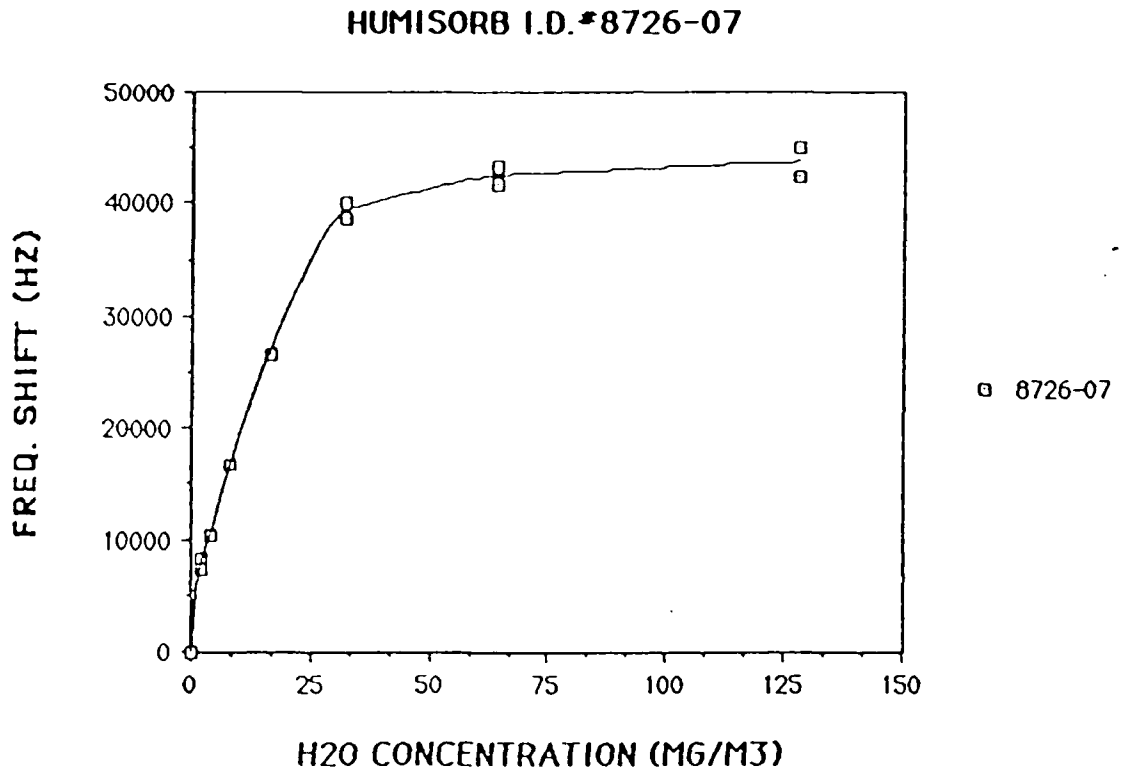

FIGURE 5.11

GEO-CENTERS, INC.

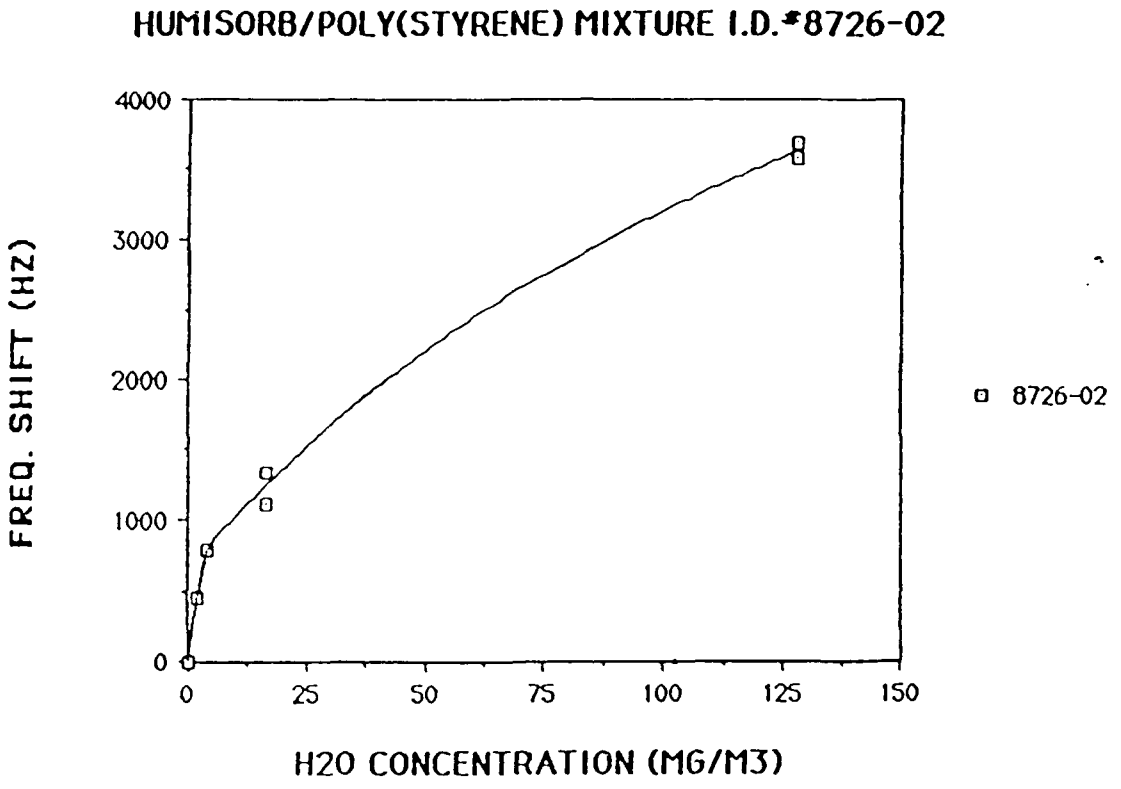

FIGURE 5.12

GEO-CENTERS, INC.

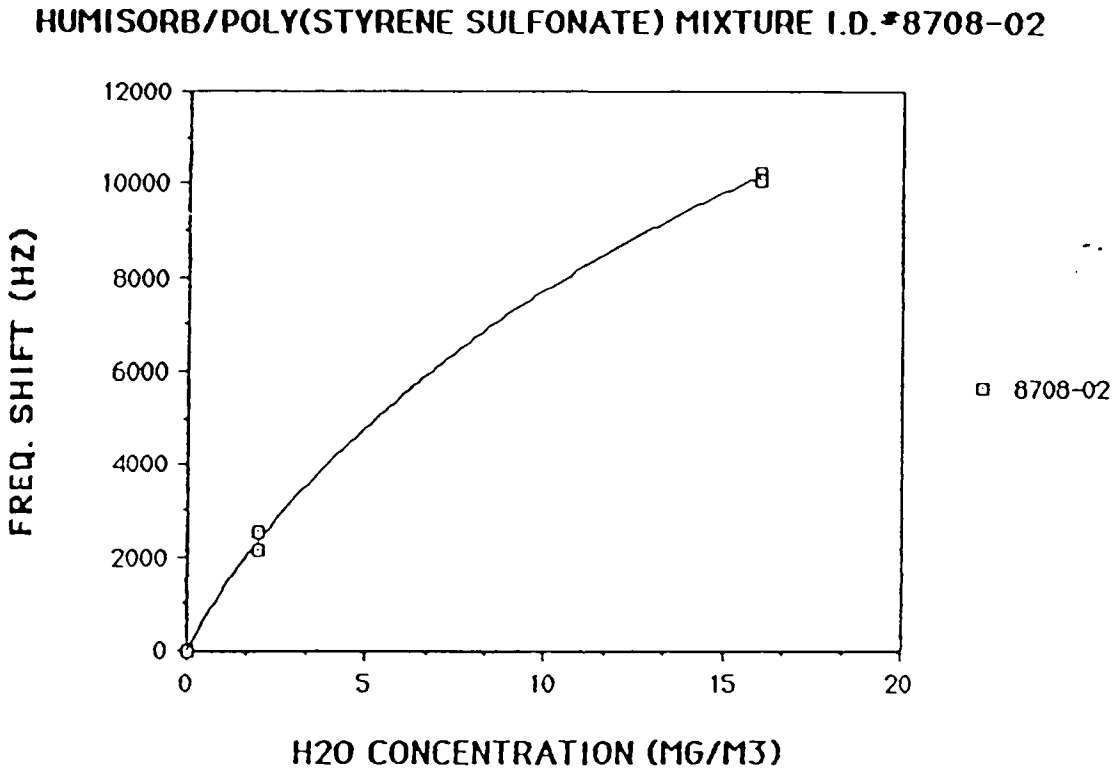

FIGURE 5.13

GEO-CENTERS, INC.

HUMISORB/POLY(ETHYLENEIMINE) MIXTURE I.D.#8709-01

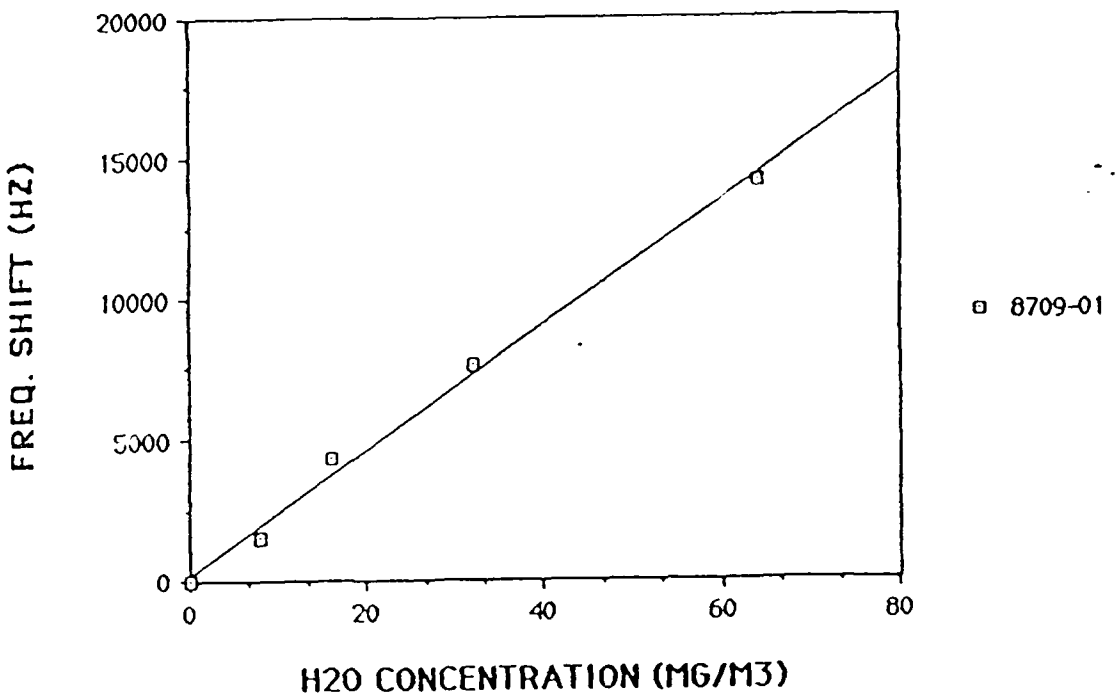

FIGURE 5.14

GEO-CENTERS, INC.

COMPARISON OF POLY(ETHYLENEIMINE) COATING REPEATABILITY

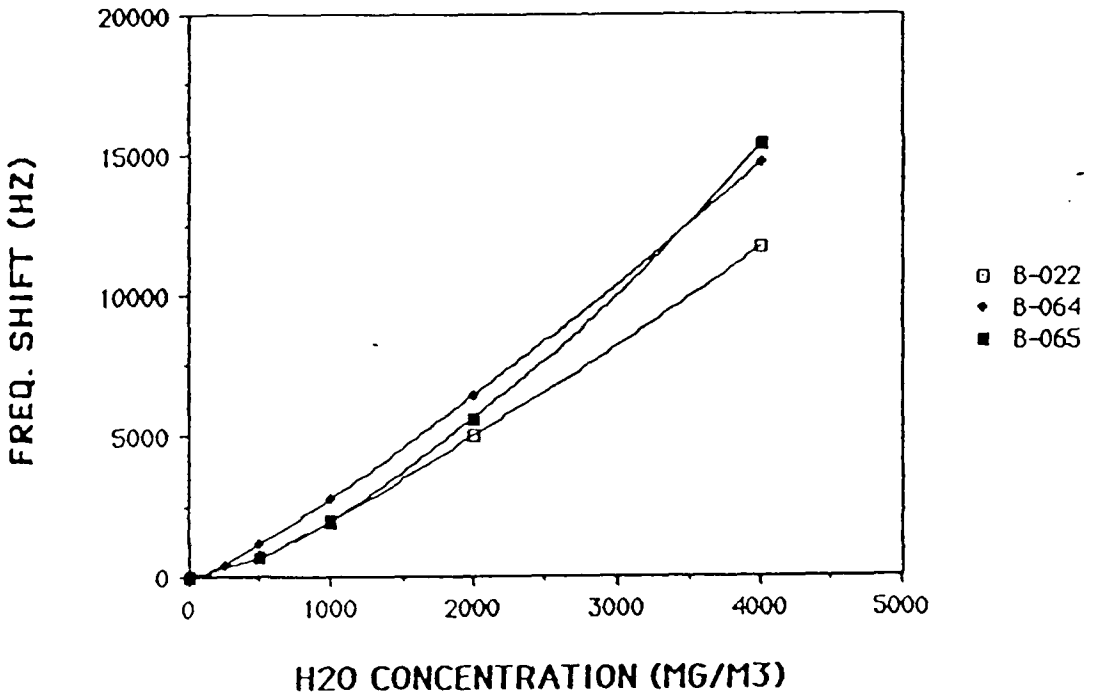

FIGURE 5.15

GEO-CENTERS, INC.

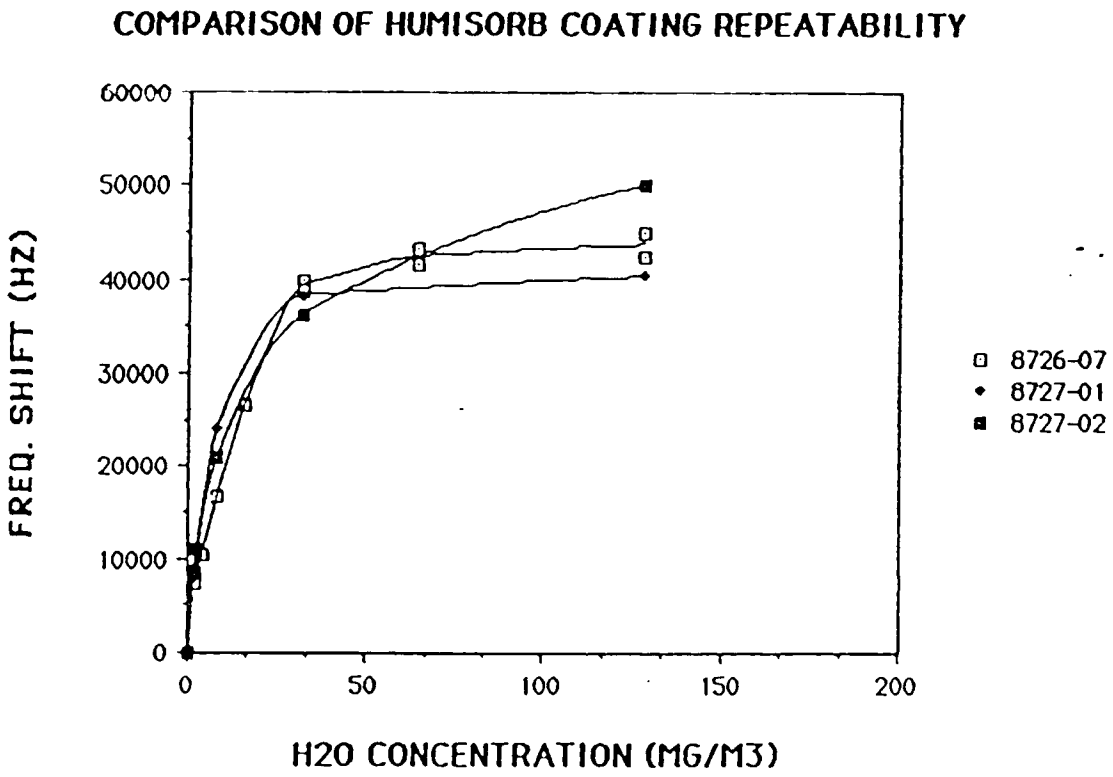

FIGURE 5.16

GEO-CENTERS, INC.

COMPARISON OF POLY(VINYL PYROLLIDONE) COATING REPEATABILITY

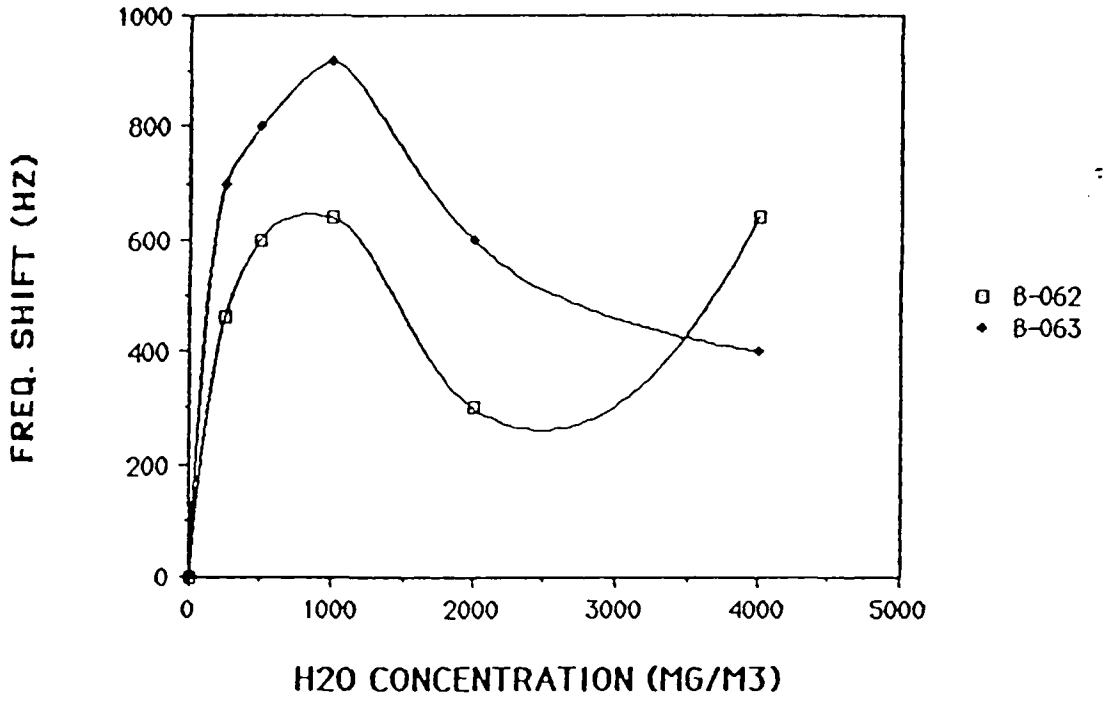

FIGURE 5.17

GEO-CENTERS, INC.

different SAW devices coated with the same material (i.e. poly(ethyleneimine), Humisorb, and poly(vinyl pyrrolidone), respectively). Figure 5.18 illustrates the variation in response obtained from the Humisorb coating over a period of several days. No consistent change in sensitivity with time is apparent. The various sensor responses are compared graphically in Figures 5.19-5.21. Finally, quantitative sensitivity values are tabulated in Table 5.1. The results are normalized to a standard 250 KHz film thickness and are calculated from responses obtained at a water vapor concentration of 16 mg/m^3. It should be noted that the SAW sensor baseline noise was typically less than 16 Hz RMS in all cases.

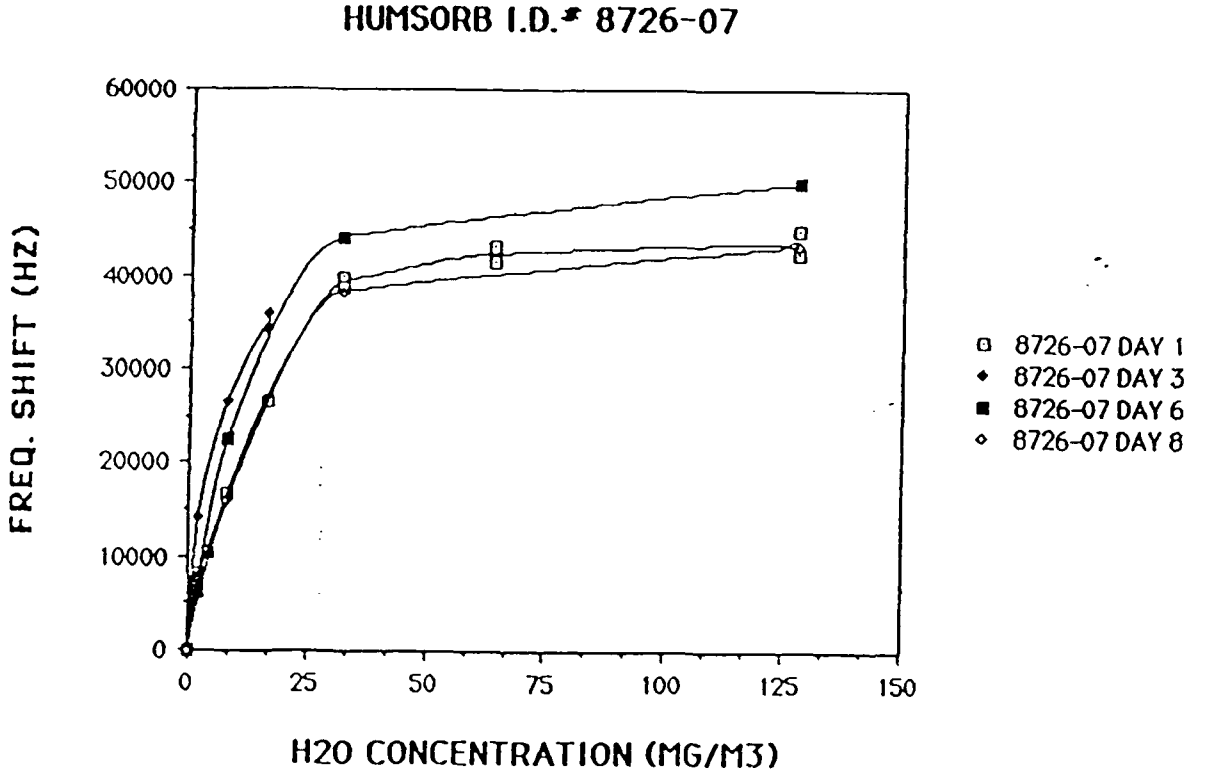

Figure 5.18 Variation in response over eight days.

GEO-CENTERS, INC.

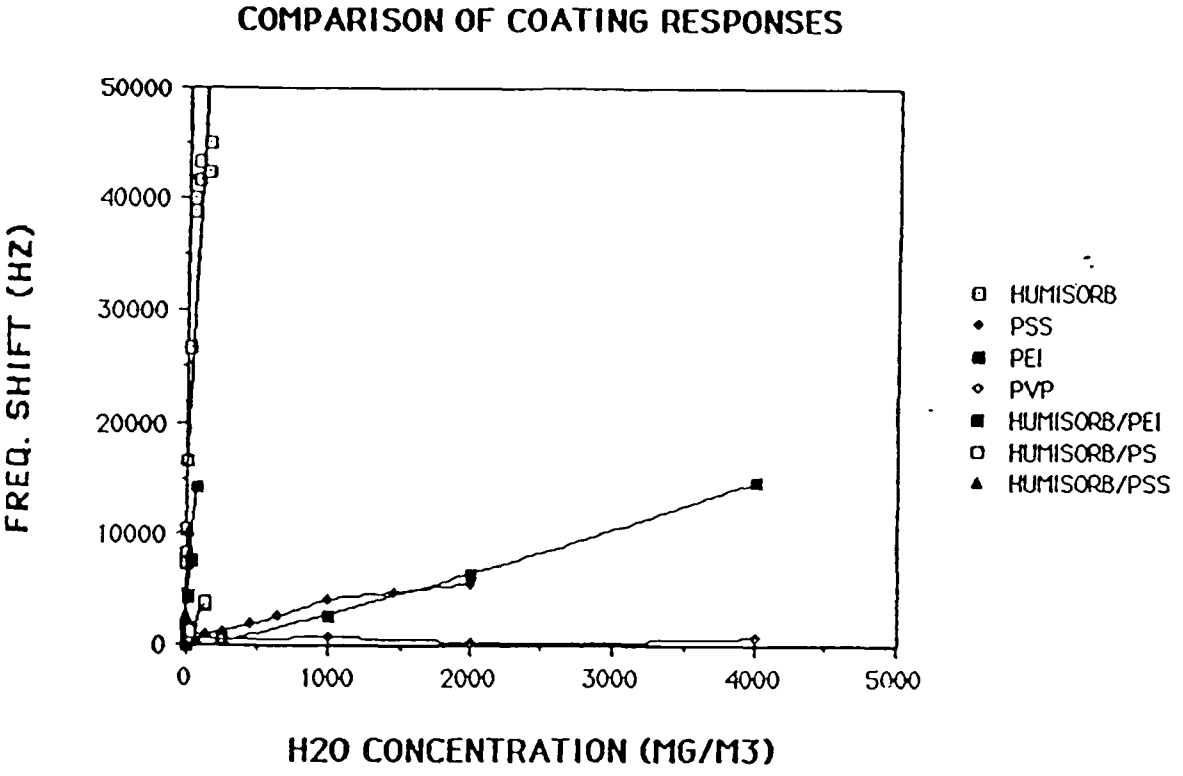
COMPARISON OF COATING RESPONSES
FREQ. SHIFT (HZ)
50000
40000
30000
20000
10000
0
0
1000
2000
3000
4000
5000
H2O CONCENTRATION (MG/M3)
HUMISORB
PSS
PEI
PVP
HUMISORB/PEI
HUMISORB/PS
HUMISORB/PSS

FIGURE 5.19

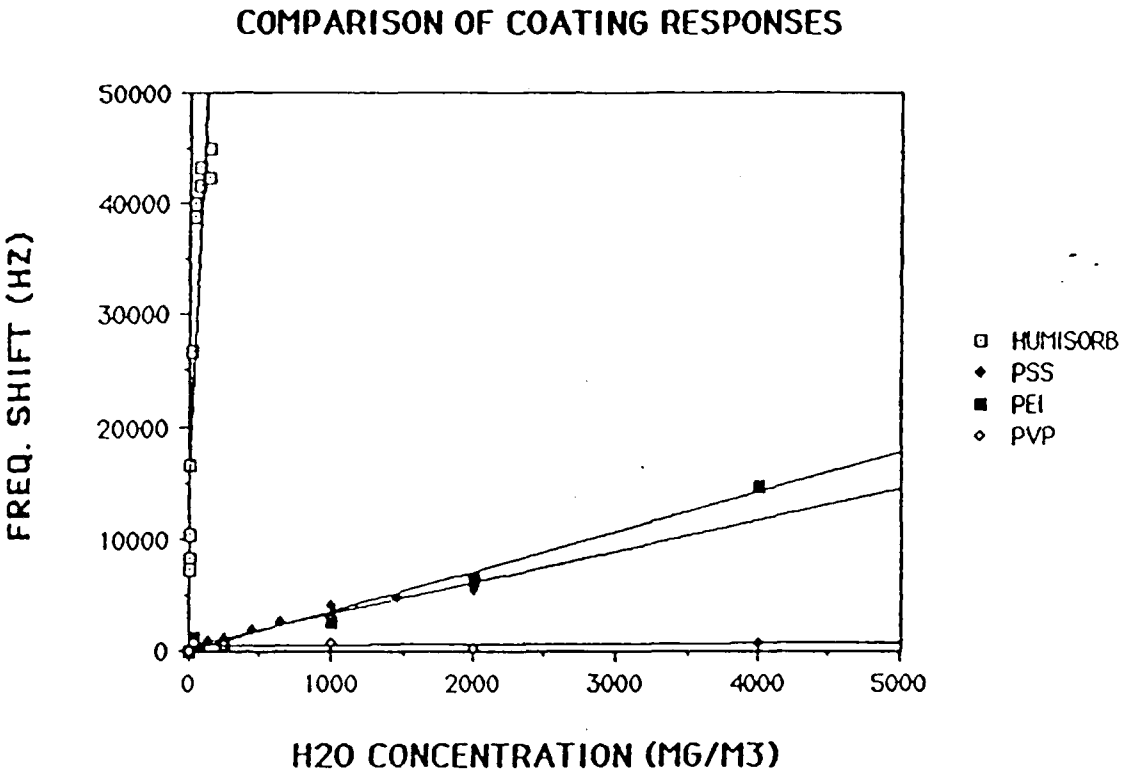

FIGURE 5.20

GEO-CENTERS, INC.

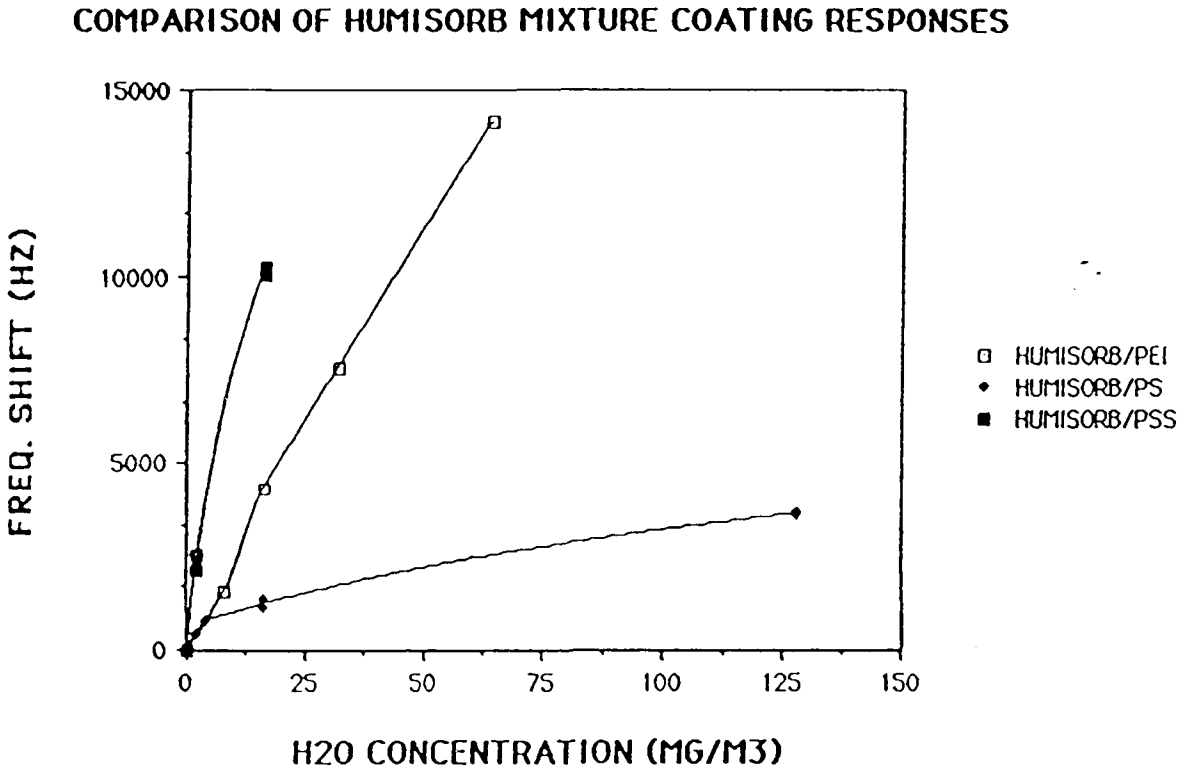

FIGURE 5.21

GEO-CENTERS, INC.

TABLE 5.1

SUMMARY OF SAW SENSOR
RESPONSES TO WATER

COATING	RESPONSE* (HZ/MG/M^3)
Humisorb I.D.#8726-07	1667
Humisorb/PEI Mixture I.D. #8709-1	222
Humisorb/PS Mixture I.D. #8726-02	84
Humisorb/PSS Mixture I.D. #8708-02	592
Poly(styrene Sulfonate) I.D. #8647-01	4.5
Poly(vinyl Pyrrolidone) I.D. #B-062	0.6
Poly(ethyleneimine) I.D. #B-064	2.7

* Responses normalized to coating thickness of 250 KHz.

5.5 Summary and Conclusion

5.5.1 Summary

The results of the coating evaluations (tabulated in Table 5.1) clearly indicate that "Humisorb" is, by far, the most sensitive coating for water exhibiting an intrinsic response hundreds of times greater than the organic polymer sorbents. If one defines a water vapor detection limit as that concentration required to produce a signal that is 3 times larger than the noise level of the sensor, then the intrinsic response of a Humisorb coated sensor (250 KHz thick) should provide a detection limit of approximately 0.03 mg/m^3, nearly a factor of 20 better than the desired goal of 0.6 mg/m^3. The sensors fabricated in this study were able to accept only 50 KHz of Humisorb coating resulting in an actual detection limit of approximately 0.15 mg/m^3, still a factor of 4 better than the goal. The sensor is useful up to water concentrations of about 150 mg/m^3, thereby demonstrating a usable concentration range of more than 3 orders of magnitude.

The polymeric coatings exhibited less sensitivity than the humisorb but were more linear and useful at much higher water vapor concentrations. Among the polymers studied, poly(ethyleneimine), PEI, stands out as a highly reproducible, sensitive, and linear water sensor. Unfortunately, it exhibited a detection limit of about 15 mg/m^3, not adequate for the Navy application. Poly(vinyl pyrrolidone), PVP, was significantly less sensitive than the poly(ethyleneimine) and exhibited a highly non-linear response. In addition, PVP was difficult to reproduce from sensor-to-sensor. Poly(styrene sulfonate), PSS, was reasonably sensitive but was less linear than the PEI.

The attempts to blend the Humisorb with other hygroscopic polymers were successful in extending the dynamic range of the sensor but at the expense of reduced sensitivity (compared to pure Humisorb). The Navy application does not require a large dynamic range so this strategy is not a useful one.

Day-to-day measurements of the Humisorb sensor behavior (Figure 5.18) indicated that the sensor was stable and that there were no obvious variations in device sensitivity with time that could not be attributed to variations in room temperature or vapor generator output.

Tests of the completed instrument in which the on-board microcomputer controlled the exposure of water vapor to the SAW sensor produced signals typical of those illustrated in Figure 5.22. In Figure 5.22 a Humisorb coated SAW device was exposed periodically to dry air and then to air containing 16 mg/m^3 of water vapor. Excellent sensitivity was observed along with a response time of approximately 30 seconds. The magnitude of the signal was very repeatable. Unfortunately, when the instrument was exposed to dry air at the system input, a small but easily measured signal was obtained (e.g. 400 Hz corresponding to about 1.2 µg/L of water) when a signal of 0 Hz was expected. The source of this residual signal was identified as ambient water vapor diffusing through the Teflon tubing used to connect the pumps, valves and sensor.

5.5.2 Conclusion

This study has demonstrated that SAW vapor sensors are readily able to detect water vapor rapidly, reproducibly, and

TYPICAL SAW VAPOR SENSOR INSTRUMENT RESPONSE

48 KHZ HUMISORB COATING

16 mg/m^3 WATER VAPOR CONCENTRATION

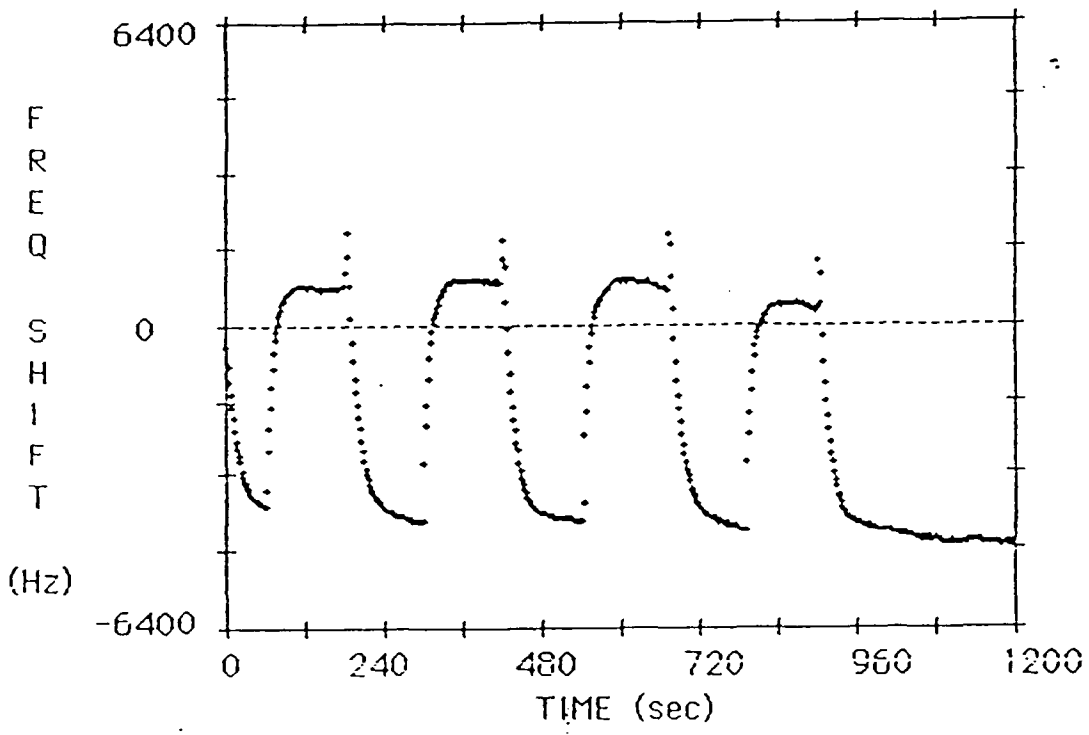

FIGURE 5.22

GEO-CENTERS, INC.

with sensitivities that are more than adequate to meet the Navy requirements.

Ironically, the present instrument design failed to function as expected owing to the extraordinary sensitivity of the SAW device. The current design of the instrument uses Teflon tubing and fittings through which traces of ambient water vapor apparently can diffuse. The presence of these traces of moisture results in a small signal from the SAW sensor even when dry reference air is supplied to the sample inlet of the instrument. A redesign of the instrument using stainless steel tubing instead of Teflon will undoubtedly eliminate the problem. Once these leaks are eliminated, the existing instrument should be capable of measuring water vapor in air at concentrations around 0.15 mg/m^3, in less than 3 minutes.

6.0 EMISSION CHARACTERISTICS OF INFRARED DECOY MATERIALS

THE WORK CONDUCTED ON THIS TASK IS CLASSIFIED CONFIDENTIAL (C)

A portion of this task has been reported as

R.A. Jeffries, H.H. Nelson, J.R. McDonald, "Emission Spectral Output Characteristics of the MK-264 Grain From 250-850 nm," Proceedings of the 33rd IRIS Symposium, 1985.

7.0 MONITORING OF DEUTERATED LUBRICANT PERFORMANCE

7.1 Introduction

Lubricant failure is considered (7.1) to be the cause of the high rate of bearing failures found in the blower motors that are used throughout the U.S. Navy Submarine fleet as standard equipment in the Sperry-Univac 0J172 (V) UYK computer I/O consoles. A promising lubricant for extending the life of these bearings is a formulated deuterated neopentyl polyol ester. This choice of basestock is based on the excellent physical and chemical properties of the neopentyl polyol esters over a wide temperature range (-55°C to 260°C) and the increase in lubricant oxidative stability on deuteration (7.2-7.5), i.e. substitution of hydrogen with deuterium.

The effect of deuteration on the oxidative stability of a neopentyl polyol ester, namely, pentaerythritol tetrahexanoate (PETH) at 220°C and ~237°C has been described in previous reports (7.6, 7.7). In an earlier investigation (7.5, 7.7), with the same additives and additive concentration employed, deuteration of both acid and alcohol moieties of PETH, i.e. d_{52}: perdeutero pentaerythritol perdeutero tetrahexanoate (dPEdTH) effected no appreciable increase in oxidative stability versus deuteration of only the acid moiety, i.e. d_{44}: pentaerythritol perdeutero tetrahexanoate (PEdTH). Consequently, a PEdTH ester was selected as the candidate basestock for bearing tests (7.8).

Results from a previous study (7.7) have indicated the higher oxidative stability of a PEdTH ester, in the presence of an amine antioxidant, to be a multiplicative product of the deuteration effect and an alkali metal effect.* This alkali

metal effect, which is synergistic with the amine antioxidant, and operative in both deuterated and nondeuterated pentaerythritol tetraesters, is also concentration dependent (7.5, 7.7). Thus, a maximum in the oxidative stability has been observed as the concentration of alkali metal is increased (7.5,7.7). These results are significant since the lubricant to be employed in the bearing tests is a grease formulation with 11% by weight lithium stearate (Li, 2628 ppm) as the grease thickener.

In this study PEdTH and PETH basestocks were screened with the objective of selecting a suitable deuterated lubricant candidate and nondeuterated control for the blower motor bearing tests. Results of the preliminary screening test employed and the evaluation of selected basestocks are given in Sections 7.2 and 7.3. The effect of alkali metals on oxidative stability of these basestocks is also included in Section 7.3. The results of evaluating the oxidative stability of selected lubricant formulations is given in Section 7.4. A preliminary study of the effect of higher temperatures (>220°C) on the oxidative stability of a PEdTH ester with an inherent alkali metal content in the presence of an antioxidant is demonstrated in Section 7.5.

---

*Alkali metal compounds may be incorporated in the basestock during the standard workup procedure of isolating the tetraester, since this involves alkali metal salts.

7.2 Oxidative Stability Screening Tests

A preliminary screening of the PEdTH and PETH basestocks containing only an antioxidant (0.5% octyl PANA -- N-p-octylphenyl-alpha-naphthylamine) was performed by evaluation of their oxidative stabilities. Commercial lubricant formulations usually contain higher antioxidant concentrations (1-2%). With less antioxidant, a comparative evaluation is obtained in less time.

Selected basestocks were further evaluated with a complete additive package (1% octyl PANA and 0.2% benzotriazole) in the presence of a steel coupon. To determine the alkali metal effect of the lithium stearate grease thickener, mixtures containing 11% by weight lithium stearate in the formulated lubricant were also tested.

7.2.1 Oxidation Apparatus

Oxidation of the basestocks was performed in pyrex glass cells (30 cm long, 1 cm inside diameter), containing an inlet tube through which dry filtered air was bubbled; the tip of the inlet tube extended 0.3 cm above the base of the cell to facilitate aeration of the small sample volume used (2 ml). The cells were heated in an oven, controlled to 0.5°C (see figure 7.1). Prior to use, the cells were cleaned in a hot nitric/sulfuric acid bath, rinsed repeatedly with distilled water, and dried overnight in an oven.

Unless otherwise specified, the reference oxidations were performed on the basestock (2 ml), containing N-p-octyl phenyl-alpha-naphthylamine (octyl PANA 0.5%), as the anti-oxidant with dry air (flow rate 20 ml/min), and at a fixed temperature (220°C).

7.2.2 Detection and Recording of Oxidative Degradation

Oxidation stability of a lubricant is determined by measurement of its induction period, which is the time elapsed until oxidative degradation occurs. At the onset of oxidative degradation, a depletion of the anti-oxidant concentration occurs, and this is accompanied by a sharp increase in viscosity, acidity, and peroxide concentration of the basestock. Measurement of these parameters as a function of time, has been the conventional method for determining the induction period of the basestock. This procedure requires periodic sampling for analyses, which are tedious, labor intensive and wasteful of the lubricant sample.

To obviate these problems another technique involving an electronic gas sensor was developed for monitoring the oxidation stability of the basestock.

A block diagram of the experimental apparatus is shown in Figure 7.1. Excellent correlation of the sensor method of detection versus the conventional method is illustrated in Figure 7.2.

Initially, a recorder was used to plot the sensor response (voltage output signal) as a function of time. However to accomplish multiple runs simultaneously a computer is used for control; the data is visualized on a television monitor, and stored on disc. A maximum of 16 oxidation tests can be monitored simultaneously. A further refinement of the system is in the computer programming: conversion of the voltage output signal from the sensor to a parameter involving concentration of the

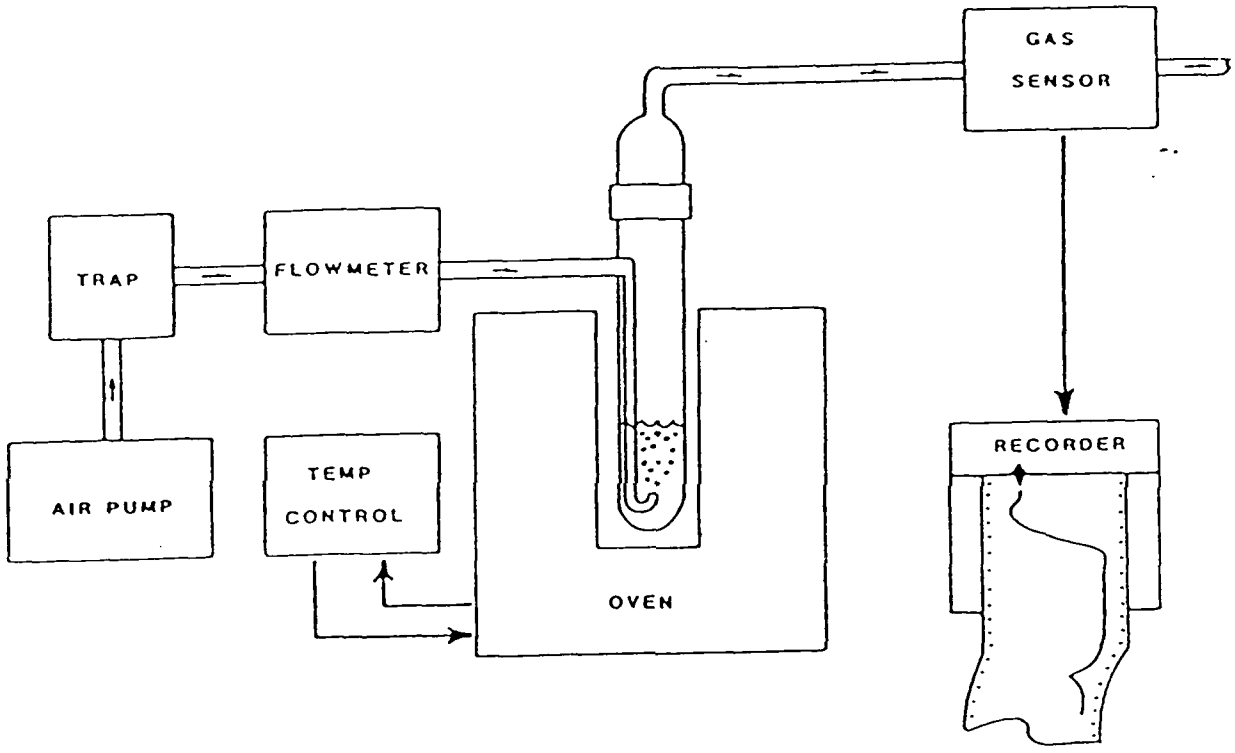

Figure 7.1 Oxidation test apparatus.

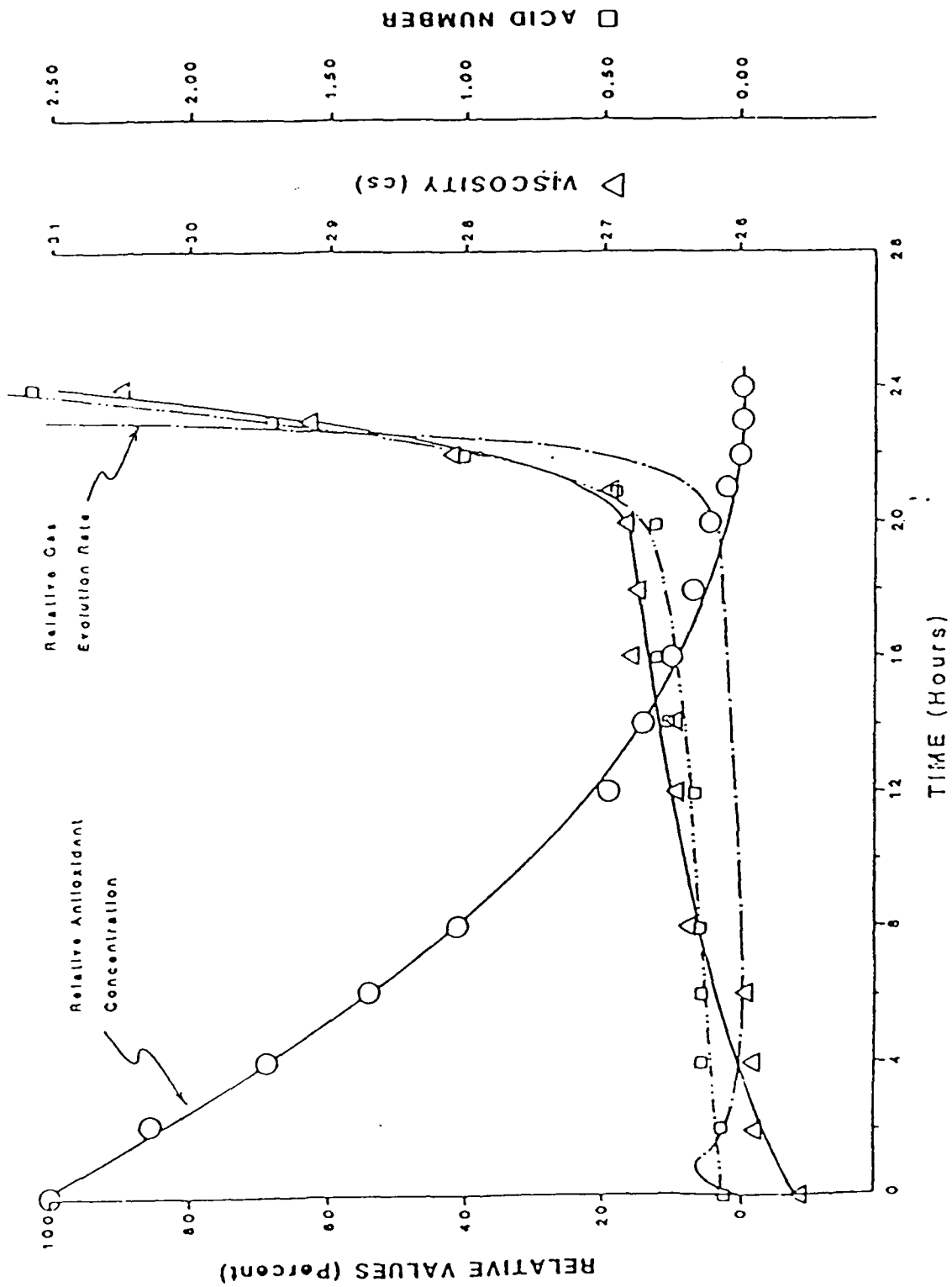

Figure 7.2 Correlation of oxidative breakdown indicator

GEO-CENTERS, INC.

effluent low molecular weight gases and vapors eliminates the variation in sensitivity among the sensors.

7.3 Basestock/Additive Evaluation Tests

7.3.1 Effect of Basestock Purity

The purity of the basestocks was characterized as described in a previous report (7.7). Triester content (a result of incomplete esterification) was measured by using Fourier transform infrared spectroscopy, and the alkali metal content by using inductively coupled plasma spectrometry. Multielement analyses of the basestocks were performed for 20 elements; namely, sodium, boron, silicon, magnesium, iron, silver, aluminum, beryllium, chromium, copper, nickel, lead, tin, titanium, barium, cadmium, manganese, molybdenum, vanadium, and zinc. Data for the induction period, triester content and four of the elements (Na, B, Si, Mg) are summarized in Table 7.1.

7.3.2 Role of Triesters

Triester content of the basestocks screened varied from <5% to 20% (Table 7.1). However, no correlation of the induction period (measure of oxidative stability) with varying triester content is apparent for similar PETH or similarly deuterated PEdTH basestocks. These results are consistent with previous observations (7.5, 7.7).

7.3.3 Role of Alkali Metal

Multielement analyses of the basestocks revealed the presence of varying amounts of sodium, boron, silicon, and magnesium. Levels less than 1 ppm could not be accurately measured (Table 7.1). At high levels of sodium, the

Table 7.1 Basestock Composition and Preliminary Screening Test Results (0.5% octyl PANA at 220°C)

Basestocks	Atom % Deuteration	Multi-Element Analysis (ppm)[a] Na	B	Si	Mg	Triester Content (%)	Induction Period (Hr)
PEdTH 2083-G	d_{44} 98.6	<1	-	5.4	-	<5	62
F529	98.0	1980	1500	11.5	2.3	20	344
F529A	98.0	<1	10	20.6	-	20	107
F651	97.4	600	465	53.5	2.3	5	272
F145[b]	97.1	2.9	N/A	N/A	N/A	10	9
F303[b]	95.5	160	+++	+	-	20	237
dPEdTH F144[b]	Alcohol Acid 98.0 94.6 d_{52} 95.1	13	N/A	N/A	N/A	10	111
PETH F258	None	.8	N/A	N/A	N/A	<<5	2.9
F146	"	1.6	-	50	-	10	5.7
F652	"	<1	-	28.3	-	<5	6.0
238H	"	<1	-	50	-	<5	7.1
F420R	"	92	50	10	-	5-10	58
Herc A[b]	"	<1	-	2.5	-	5-10	3.2
F304[b]	"	-	++	+	-	5	3.6

[a]Numerical values are given for analyses performed using inductively coupled plasma spectrometry; (-) refers to "not detected". [+++, ++, +, refers to relative amounts detected using flame emission spectrometry.]; N/A refers to "not available".

[b]Basestocks screened in previous investigations (5,7).

concentrations of boron and sodium seem somewhat related, suggesting a possible sodium boro-compound to be present in these basestocks.

Table 7.1 shows a correlation between the sodium content of the basestocks (>3 ppm) and their induction periods. Levels of sodium less than approximately 3 ppm seem ineffective. Thus, consistent with previous results (7.5, 7.7), the alkali metal content of the basestocks appears to explain the varying oxidative stabilities of similarly deuterated PEdTH esters as shown in Figure 7.3 and nondeuterated PETH esters (Table 7.1). The various formulations examined can be grouped as follows:

Table 7.2

Formulation	Purpose	Description
A	Preliminary screening	Basestock + 0.5% octyl PANA
B	Lubricant formulation	Basestock + 1% octyl PANA + 0.2% benzotriazole (BTA). Steel coupon added.
C	Grease Formulation: Evaluation of alkali metal effect of Li.	Formulation B + 11% lithium stearate (2628 ppm Li). Steel coupon added.
D	Verification of the alkali metal effect. Examined only in certain cases.	Formulation B + 1000 ppm Na ex sodium acetylacetonate. Steel coupon added.

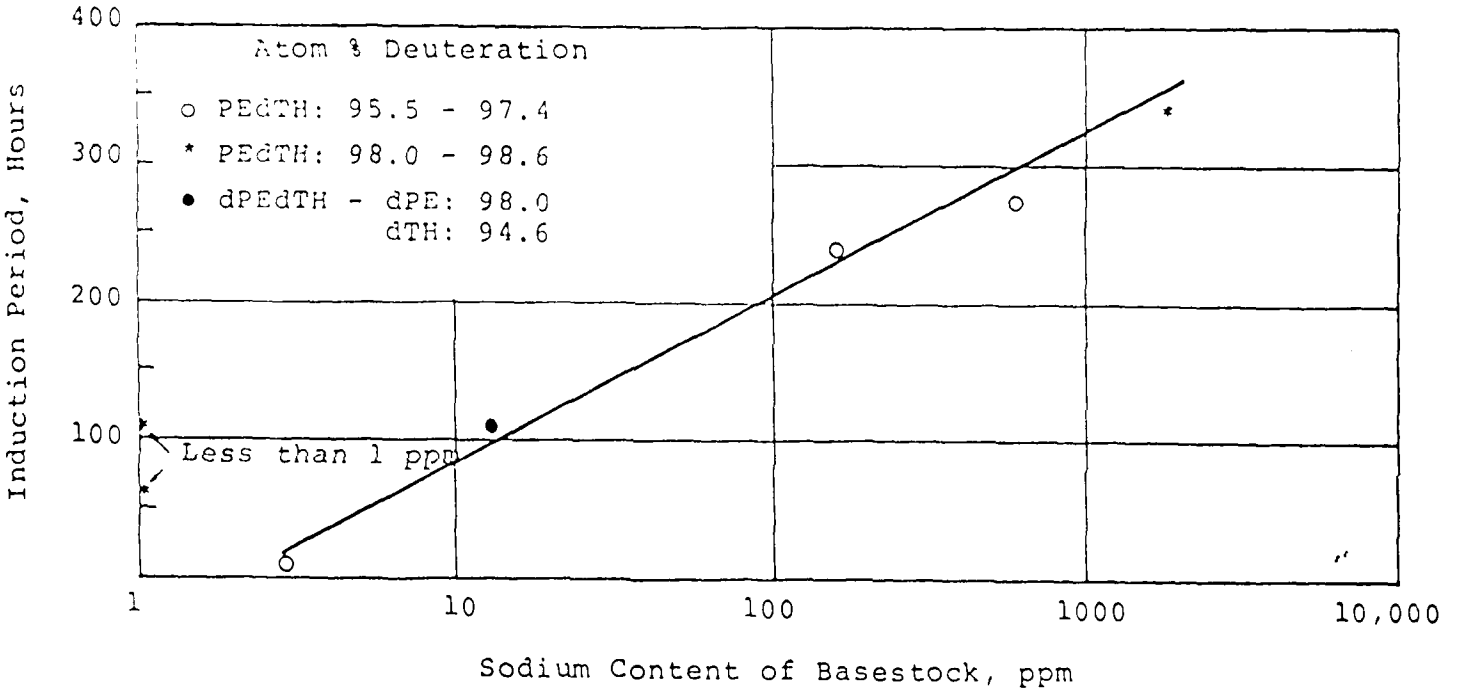

Figure 7.3 Effect of inherent sodium concentration on the induction period of deuterated PETH esters containing 0.5% octyl PANA at 220°C.

In the formulations that did not contain added alkali metal (A and B, Table 7.3), the increase in the induction periods of the basestocks with an inherent alkali metal content relative to similar basestocks with low alkali metal content (< 1 ppm) was again consistent with an alkali metal effect. Thus, for PEdTH F529, the alkali metal effect was a factor of 3-24, and for PETH F420R, a factor of 8-29, depending on the formulation. The variation in the alkali metal effect for formulation A or B is related to the variation in induction period of the ester used as reference (e.g. 2083-G or F529A for the PEdTH esters).

In the formulations which contained added alkali metal (C and D), only those basestocks with low inherent sodium content (<1 ppm Na) exhibited a significant increase in induction period. This increase, also attributable to the alkali metal effect, was a factor of 10-37 in 98 atom % deuterated PETH esters, and a factor of 21-73 in PETH esters. However, PEdTH F529 and PETH 420R, which were esters with high inherent alkali metal content, both exhibited a decrease in induction period upon the addition of lithium stearate (2628 ppm Li). A small increase (1.5 fold) in PEdTH F529 was observed in the presence of smaller amounts of added alkali metal (1000 ppm Na). These results indicated that the basestocks employed in the grease formulations for the blower motor bearing tests should contain an inherently low alkali metal concentration (< 1 ppm). Suitable candidate basestocks therefore included PEdTH 2083-G and PEdTH F529A. Likewise, suitable control basestocks included PETH 238H and PETH F258 and F146.

The results described are in general agreement with the alkali metal effect on oxidative stability alluded to in the Introduction. The optimum alkali metal effect generally observed

Table 7.3 Effect of Formulation and Alkali Metal Content on Induction Period at 220°C.

Basestocks	Inherent Sodium Content (ppm)	Induction Periods of Formulations[a] A (Hr)	B (Hr)	C[b] (Hr)	D (Hr)	Alkali Metal Effect Due to: Inherent Na A	B	Added Li C/B	Na D/B
PEdTH:[c] 2083-G	<1	62	26	333[d]	965	None	None	13	37
F529A	<1	107	54	516[d]	-	None	None	9.6	-
F529	1980	344	615[d]	<53[d], 15[d]	<900	3.2, 5.5	11, 24	~0.1	~1.5
PETH: F258 + F146	~1	3.6	2.2	61	160	None	None	28	73
238H	<1	7.1	6.1	207	129	None	None	34	21
F420R	92	58	64	15	-	8.2, 19	10, 29	0.23	-

[a] See text 2.1.2B -- A: Preliminary Screening; B: Lubricant Formulation; C: Formulation B + Lithium Stearate (2628 ppm Li); and D: Formulation B and 1000 ppm Na.

[b] Because of the soap effect of stearates on bubbling air through this formulation, the sample mixture tended to creep up the sides of the oxidation cell. This can result in poor precision of the data.

[c] 98 atom % deuterated.

in these results, approximately 30 fold, is also consistent with previous data (7.5, 7.7) for both PETH and PEdTH basestocks. The alkali metal effect of ~73 fold observed in a PETH ester (F258 and F146), formulation D, is an isolated case, and warrants further study.

7.3.4 Effect of Deuteration

Atom percent deuteration was measured using proton nuclear magnetic resonance (NMR) spectroscopy. The effect of atom percent deuteration on the induction period of a limited number of PEdTH basestocks containing low alkali metal content is shown in Table 7.4. The results indicated a significant increase in induction period with increased deuteration (> 97 atom %) of a PEdTH ester. A similar increase in oxidative stability with increased deuteration (> 94 atom %) has been reported by both Rebuck et al. (7.2) and Conte et al. (7.3) for a synthetic hydrocarbon.

The effect of deuteration, also shown in column 4 of Table 7.4, was determined by comparing the ratios of the induction periods of PEdTH vs. PETH basestocks that were purchased from the same manufacturer at the same time. However, because of the variation in the induction period of the nondeuterated ester (PETH) by a factor of two, the values given for the deuteration effect are not definitive. Further, scatter in the data was observed at the higher deuteration levels. For example, PEdTH F529A is slightly less deuterated than 2083-G, but has about a 40% longer induction period. Also, a large anomalous peak present in the proton NMR spectrum of F529A has not been identified. Additional work is therefore required to accurately establish the magnitude of the deuteration effect at high levels

Table 7.4 Effect of Deuteration of the Basestock on Induction Period (0.5% Octyl PANA at 220°C).

Deuteration (Atom %)	Induction Period (Hr)		Deuteration Effect
	PEdTH[a]	PETH[a]	PEdTH/PETH
98.6	2083-G: 62	238H: 7.1	8.7
98.0	F529A: 107	F652: 6.0	18
97.1	F145: 9	F258: 3.0	3.0[b]

[a] Basestocks containing similarly low alkali metal content (< 1 ppm).

[b] Previous investigation (7.5,7.7).

Table 7.5 Effect of Deuteration of Lithium Stearate (11% w/w: 2628 ppm Li) on Induction Period.

Basestock	Induction Period (Hr)	
	Lithium Stearate	Deuterated Lithium Stearate
Herc A[a] (Nondeuterated)	25	8.3
PEdTH F529A[b]	516	290

[a] In presence of 0.5% octyl PANA at 220°C.

[b] In presence of 1% octyl PANA + 0.2% BTA and steel coupon at 220°C.

of deuteration (> 97 atom %). Nevertheless, the results obtained suggest that a PEdTH basestock with 98 atom % (or higher) level of deuteration, and with low inherent alkali metal content, to be a suitable candidate for evaluation in the bearing tests (7.8).

Since the stearic acid moiety of lithium stearate is a long chain fatty acid it is therefore susceptible to increased oxidative attack on its secondary carbon-hydrogen bonds (7.9). The effect of a deuterated lithium stearate was therefore investigated. The basestocks employed were a commercial ester, Hercolube A, and a PEdth ester, F529A.

As shown in Table 7.5, the oxidative stability decreased in the presence of deuterated lithium stearate versus its nondeuterated analog under comparable conditions. These results warrant further study. However, for the grease formulations, nondeuterated lithium stearate was employed.

7.4 Evaluation of Oxidative Stability of Selected Lubricant Formulations

Because of the high alkali metal concentration of the lithium stearate thickener (2628 ppm Li) used in the grease formulation, the basestocks selected for the blower motor bearing tests should contain an inherently low alkali metal content. Also, as suggested, the PEdTH candidate basestocks should have a high atom percent deuteration (> 97 atom %) for increased oxidative stability.

Consequently, for the bearing tests, potential candidate basestocks included PEdTH 2083-G and PEdTH F529A. However, because of the anomalies of PEdTH F529A, PEdTH 2083-G, was

selected as the candidate basestock. The PETH basestocks that qualified as a suitable control included 238H and the combination mixture: F258 + F146. Based on availability, the latter mixture was employed as the control. The deuteration effect observed in the various formulations is shown in Table 7.6. The results indicated a deuteration effect of approximately five to fourteen fold, depending on the formulation employed. Thus, in the grease formulation, the deuterated grease should have at least a five fold longer life in the bearing tests, assuming the bearing life to be solely dependent on the oxidative stability of the lubricant formulation.

7.5 Effect of Temperature on the Oxidative Stability of a Deuterated Ester at 220 - 280°C

The significant enhancement in induction period as a result of the dual effects of alkali metal concentration and atom percent deuteration can be alternately translated via the Arrhenius equation into a potential for thermooxidative stability at temperatures higher than 220°C. Consequently, a preliminary study was conducted on the effect of temperature within the range 220-280°C, on the induction period of PEdTH F529 (98.0 atom % deuterated; sodium content: 1980 ppm). The data are plotted in Arrhenius form in Figure 7.4.

The linear relation obtained indicates excellent Arrhenius correlation of the data. The activation energy, calculated from the slope of the line, was found to be 48.71 kcal/mole. This information would be useful in future comparative kinetic studies with a PETH ester.

Table 7.6 Deuteration Effect of a Selected PEdTH Basestock in Various Formulations at 220°C.

Formulation	Additions to Basestocks	Induction Period (Hr.)		Deuteration Effect PEdTH/PETH
		PEdTH (2083-G)	PETH F258 + F146	
A	0.5% octyl PANA	62	3.6	14
B	1% octyl PANA, 0.2% BTA, steel coupon	26	2.2	13
C	1% octyl PANA + .2% BTA + steel coupon + 11% Li Stearate (2628 ppm Li)	333	61	5.5
D	1% octyl PANA + .2% BTA, steel coupon + 1000 ppm Na	965	160	6

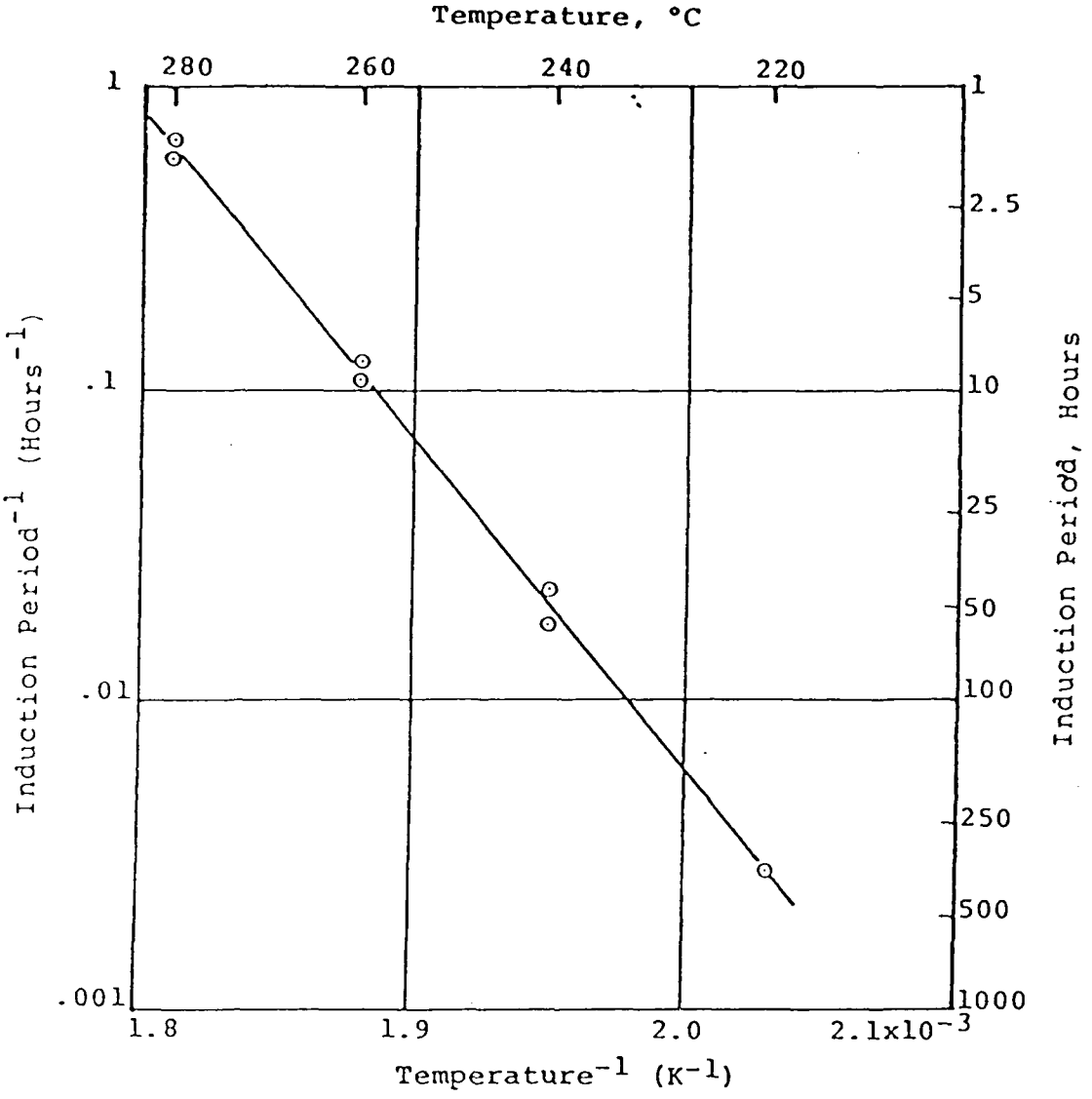

Figure 7.4 Effect of temperature on the induction period of a PEdTH ester (98 atom %) containing 1980 ppm inherent sodium and 0.5% octyl PANA.

These preliminary results are quite promising. For example, the oxidative stability of the PEdTh ester employed was 1.6 hours at 280°C, in the presence of 0.5% octyl PANA. These results indicate that combination of the dual effects of deuteration and alkali metal concentration offers a potential for lubricant operating temperatures significantly higher than present levels (220°C).

7.6 Conclusions

Consistent with previous results (7.5, 7.7) oxidative stability of a deuterated ester has been found to be a function of the deuterium isotope effect and an alkali metal effect. The significant increase in oxidative stability with increase in deuteration greater than 97 atom percent is in agreement with previous observations reported by Rebuck et al. (7.2) for a synthetic hydrocarbon. Because of the variation in oxidative stabilities of similarly deuterated PEdTH, and nondeuterated PETH basestocks, further work is required to establish definitive values for the deuteration effect of the basestock at higher levels of deuteration (> 97 atom %). The deuteration of lithium stearate (thickener) in the grease formulation decreased the oxidative stability of the basestock relative to its nondeuterated analog. Consequently, nondeuterated lithium stearate was used in the grease formulation.

The effect of alkali metal concentration on oxidative stability also corroborates previous observations (7.5, 7.7), i.e., increase in oxidative stability is followed by a decrease with increasing log of the alkali metal concentration. Consequently, for an optimum alkali metal effect on oxidative stability, the alkali metal content of the additives employed in

the formulation determines the allowed level of alkali metal content in the basestock. Accordingly, because of the high alkali metal content in the grease formulation (2628 ppm Li), the basestocks that were selected for the blower motor bearing tests had a low alkali metal content.

The basestock selected for the blower motor bearing test was a highly deuterated pentaerythritol perdeutero tetrahexanoate (PEdTH: d_{44}, 98.64 atom %) with low alkali metal content (< 1 ppm). The control was its nondeuterated analog, i.e. pentaerythritol tetrahexanoate (PETH), also with less than 1 ppm alkali metal content. Assuming that bearing life is solely dependent on the oxidative stability of the lubricant, the deuterated grease should have at least a 5-fold longer life at 220°C.

Combination of the dual effects of deuteration (~98 atom %) with alkali metal concentration resulted in an ester with superior oxidative stability at 220°C, and with good potential for operating at higher temperatures (possible maximum being 280°C). These promising results warrant further study for optimization of both the deuteration effect and the alkali metal effect regarding oxidative stability, especially at elevated temperatures.

7.7 References

7.1 S. Tako, "Blower, Vacuum - 7903344", Material Engineering Test Report, Document No. PX 72000-6918, Sperry-Univac, Minnesota, April 1980.

7.2 N.D. Rebuck, A.A.Conte, and L. Stallings, "The Effect of Deuterium Exchange on a Synthetic Hydrocarbon Lubricant", ASLE Trans., 20, 2, 108-114 (1977).

7.3 A.A. Conte, N.D. Rebuck, and V. Novielli, "Deuterium Substituted Synthetic Hydrocarbon Grease", ASLE Trans. 20, 3, 264-266 (1977).

7.4 H. Ravner, and H. Wohltjen, "The Determination of the Oxidative Stability of Several Deuterated Lubricants by an Electronic Gas Sensor", ASLE Preprint No. 82-AM-5A-4.

7.5 a) S.G. Pande, R.N. Bolster, and H. Ravner, "Factors Affecting Oxidation Stability of a Deuterted Ester", ASLE Trans. Preprint No. 83-LC-1A-2.

b) S.G. Pande, and H. Ravner, "Progress Report: Oxidation Stability of Deuterated Esters", Naval Research Laboratory, NRL Memorandum Report 5071, Washington, DC, April 26, 1983.

7.6 "The Oxidative Stability of Deuterated Lubricants", GEO-CENTERS, INC., GC-TR-82-182, Massachusetts, Jan. 1982.

7.7 "The Oxidation Stability of Deuterated Esters", GEO-CENTERS, INC. , GC-TR-83-182, Massachusetts, Jan. 1983.

7.8 J.E. Campana, and R.J. Doyle, "Deuterated Lubricants-Auxilliary Machines: Progress and Summary", Naval Research Laboratory, NRL Ltr Rpt. 6110-106a:RJD:bmd.2, Washington, DC, April 1983.

7.9 N.M. Emanuel, E.T. Denison, and Z.K. Maizus, trans. from Russian by B.J. Hazzard, "Liquid-Phase Oxidation of Hydrocarbons", Plenum Press, New York, 1967, p. 134.

END
DATED
FILM
8-88
DTIC